A HIGH RESOLUTION STUDY

OF THE

LOWEST 1/2+ ANALOGUE STATE IN ^{91}Nb

by

Mark Eric Bleck

Department of Physics
Duke University

Date:_____

Approved:

_____
E. G. Bilpuch, Supervisor

_____

_____

_____

_____

A dissertation submitted in partial fulfillment of the requirments for the degree of Doctor of Philosophy in the Department of Physics in the Graduate School of Arts and Sciences of Duke University

1978

ABSTRACT

(Physics)

A HIGH RESOLUTION STUDY

OF THE

LOWEST $1/2^+$ ANALOGUE STATE IN ^{91}Nb

by

Mark Eric Bleck

Department of Physics
Duke University

Date:_____

Approved:

_____
E. G. Bilpuch, Supervisor

_____

_____

_____

_____

An abstract of a dissertation submitted in partial fulfillment of the requirments for the degree of Doctor of Philosophy in the Department of Physics in the Graduate School of Duke University

1978

A HIGH RESOLUTION STUDY OF THE LOWEST 1/2+ ANALOGUE STATE IN ^{91}Nb

by

Mark Eric Bleck

Excitation functions for the reaction ^{90}Zr(p,p) were measured from 5.684 to 5.992 MeV at laboratory angles of 90°, 107°, 135° and 160°. Proton energy resolution varied between 425 and 450 eV. The data were fit to an R-matrix cross section containing 302 s-wave resonances. These levels comprise the fine structure of the lowest 1/2+ analogue state in ^{91}Nb.

Excellent beam energy resolution was maintained through use of a three loop energy regulating system adapted for high resolution work at TUNL specifically for this experiment. This system includes an optical feedback path which permits high voltage modulation of the terminal stripper in order to null residual energy fluctuations.

The fine structure distribution was incompletely resolved due to the extremely high compound nuclear level density. Nevertheless, a good fit to the theoretical distribution (Lane 1969) was obtained. The fine structure

parameters extracted from the fit were found to be in mild disagreement with those obtained in an earlier, thick target experiment (Richard et al. 1971). Severe disagreement between the Robson estimate and the experimental value was obtained for the analogue spreading width.

The statistical distributions of resonance widths and spacings were examined as a check on the R-matrix fitting procedure.

The analogue proton spectroscopic factor was deduced and compared with spectroscopic factors for the parent and anti-analogue states obtained from the literature.

ACKNOWLEDGEMENTS

I would like to thank my research advisor, Dr. E. G. Bilpuch, for his unfailing encouragement and support during all phases of this project. Sincere appreciation is also extended to Dr. G. E. Mitchell for many helpful discussions in the course of the data analysis and preparation of this dissertation.

I owe special thanks to Mr. W. K. Wells, Dr. D. A. Outlaw, Mr. C. R. Westerfeldt and Mr. J. E. Cairns, for their invaluable help in developing the instrumentation for the three loop stabilizer, and to Dr. F. O. Purser for helpful discussions concerning the tandem accelerator. The assistance of Mr. W. A. Watson in the development of the analyzing magnet stabilization system is appreciated. Additional thanks go to Mr. K. B. Sales and Miss B. H. Chou for help in taking portions of the data.

The fine work and cooperation of the machine shop, under the direction of Mr. A. W. Lovette, and the electronics shop, under the direction of Mr. S. E. Edwards, is greatly appreciated. Special thanks are due Mrs. Joseph Bailey for the professional preparation of the figures for this dissertation, Mr. J. D. Turner for photographing some of the figures, and Mr. E. Rummel and Mr. A Lovette for their help in maintaining the accelerator systems.

Warm thanks go to my parents for their support and encouragement throughout my life. Most of all, I want to thank my wife, Donna. Her love, patience, and encouragement during the past two years have made it all worth-while.

This work was supported in part by the United States Department of Energy. Some of the data analysis was performed at the Triangle Universities Computation Center, which is supported in part by the National Science Foundation.

TABLE OF CONTENTS

LIST OF FIGURES

LIST OF TABLES

'Now here, you see, it takes all the running you can do, to keep in the same place. If you want to get somewhere else, you must run at least twice as fast as that!'

-- the Red Queen

from Through the Looking Glass,
by Lewis Carroll

A HIGH RESOLUTION STUDY OF THE LOWEST $1/2^+$ ANALOGUE STATE IN ^{91}Nb

Chapter 1

INTRODUCTION

During the past twelve years, many high resolution proton elastic scattering experiments have been performed at the Triangle Universities Nuclear Laboratory. These experiments comprise a systematic study of both statistical and non-statistical phenomena associated with narrow compound nuclear resonances in the elastic scattering cross section of even-even, medium weight nuclei. In some cases the inelastic scattering and proton capture reactions have also been studied. Most of these results have been summarized by Bilpuch et al. (1976) in a recent review article.

For the most part, these experiments have been done in the TUNL 3-MV Van de Graaff laboratory. In a typical experiment, protons are incident upon a thin, solid target whose mass number lies between 26 and 64. The proton energy is continuously variable between 1.5 and 3.3 MeV with an

overall energy resolution of 300 to 400 eV.

This remarkable energy resolution is achieved through use of the analyzer-homogenizer system first developed by Parks et al. (1958). This apparatus makes use of the fact that two species of positive ions (H^+ and HH^+) emerge from the accelerator with identical time dependant energy fluctuations. An analyzing magnet diverts the molecular beam into the cylindrical electrostatic analyzer while directing the protons to the target chamber. An error signal proportional to the beam energy fluctuations is developed from the molecular beam current intercepted by a pair of slits behind the analyzer. After suitable amplification, this signal is applied to the target rod, varying the electrical potential of the target in order to cancel the time dependant energy fluctuations in the proton beam. The system is capable of reducing these fluctuations to less than 100 eV. The remaining resolution width is attributable to target straggling, target Doppler broadening, and the ion source energy spread.

Much of the high resolution work at TUNL has involved the study of isobaric analogue resonances. Indeed, the fine structure of analogue states was first fully resolved by Keyworth et al. (1966a, 1966b) in the $^{40}Ar(p,p)$ reaction. Since that time, over 40 fragmented analogues have been measured by the high resolution group at TUNL. These have been analyzed using Lane's theory (1969) which treats

analogue fine structure in the context of line broadening. Unfortunately, in this mass region ($26 < A < 64$) low background level densities generally limit the number of analogue fragments in a particular distribution and therefore limit the accuracy with which the fine structure parameters can be determined. In order to obtain a statistical assembly of levels in the fine structure pattern, a sequence of experiments in the mass 90 region was planned. This is in fact the mass region where fragmented analogue states were first observed, although not fully resolved, by Richard et al. (1964). The first step in the program was to remeasure two $1/2^+$ analogue states, one in ^{93}Tc and one in ^{91}Nb. These were studied by Richard with approximately 2 keV resolution.

Since these analogues are observed at proton energies between five and six MeV, the analyzer-homogenizer concept was adapted by Dzubay et al. (1972) for use with the TUNL tandem. This system provided 500 eV resolution which was sufficient for Outlaw (1974) to resolve the ^{93}Tc analogue fine structure. Preliminary attempts to measure the ^{91}Nb analogue revealed a much higher background level density than in ^{93}Tc. To reduce the effects of level interference, better resolution was required. However, the neutral beam homogenizer suffered from a number of intrinsic difficulties. Positional instabilities in the charged beam induced terminal fluctuations, and thus energy fluctuations,

through the corona feedback. These were only incompletely removed by the homogenizer system. In addition, the problems associated with simultaneous transport of two coupled beams (considerably more difficult in the tandem laboratory than in the 3-MV laboratory) were aggravated by small alignment problems. These factors motivated the decision to develop a terminal regulation system in which an optical feedback channel is opened to the Van de Graaff terminal. Although this system was initially intended for use in conjunction with the homogenizer, experience has shown that a target correction voltage is not required to obtain good energy resolution.

This dissertation provides a description of the operating principles and components of this system, as well as a summary of the measurement and subsequent analysis of the fine structure of the lowest $1/2^+$ analogue in ^{91}Nb.

Chapter 2 summarizes the theoretical concepts which are applied in the analysis of the data. The first three sections describe the scattering of protons through compound nuclear states. The application of the R-matrix theory of nuclear reactions to elastic scattering is outlined. Section 4 briefly summarizes the expected statistical distributions of resonance widths and spacings. Analogue states are described in section 5 in terms of the isospin model given by Robson (1965). Fine structure is discussed and the salient features of Lane's theory are presented.

Section 6 is concerned with spectroscopic factors for the analogue and parent states.

Experimental equipment and procedures are dealt with in Chapter 3. The triple loop accelerator control system is described in the first section in terms of a frequency domain model. Loop equations are presented and solved for both two and three loop systems. Energy regulation is discussed and compared in relation to the model predictions. In section 2, an improved analyzing magnet control system is discussed. Target characteristics and preparation techniques are given in section 3 while sections 4 and 5 discuss the equipment and procedures used in counting the scattered protons.

The $^{90}Zr(p,p)$ data are presented in Chapter 4. Sections 1 and 2 are concerned with the cross section data and R-matrix fits while sections 3 and 4 discuss the fine structure distribution of the analogue. Statistical distributions of the resonance parameters are examined in section 5. The proton spectroscopic factor for the analogue is deduced in section 6 and compared with parent state spectroscopic factors obtained from the literature.

Two appendices are included. The first lists the resonance parameters extracted from the R-matrix analysis. The second appendix contains physical descriptions and circuit diagrams of the triple loop control system components.

Chapter 2

THEORY

2.1 The Compound Nucleus

For more than forty years, resonance reaction studies have provided useful information about nuclear interactions and forces. Moon and Tillman (1936) discovered large variations over small energy intervals in the slow neutron activation cross section. These 'resonances' could not be explained in terms of the extreme independent particle model of Bethe (1935). In this picture, the incident neutron moves under the influence of an attractive real potential which represents an averaged superposition of the two-body interactions between the target nucleons and the projectile. This model predicts significant variations in the cross section to occur only over wide energy intervals. The experimental evidence for narrow resonances motivated the compound nuclear hypothesis of Bohr (1936). If a neutron penetrates a nucleus, it may interact with a single target

nucleon, sharing its kinetic energy in such a way that neither one can immediately escape from the averaged nuclear potential. Additional interactions and energy exchanges must then take place, involving increasingly complicated nuclear configurations, before a single nucleon acquires sufficient energy to escape. The state that is reached when all the available modes of excitation are statistically populated is called the compound nucleus. This kind of state has no 'memory' of its formation. Hence the only correlations that may be expected in observing the decay of the compound nucleus involve the conservation laws associated with the overall momentum, angular momentum, and parity of the system.

2.2 Reaction Channels and the U-Matrix

The formation of a compound nucleus is not limited to neutron induced reactions. Incident protons can initiate compound nuclear states provided they have sufficient energy to penetrate the Coulomb barrier. Because the compound nucleus can decay in many ways, an incident proton beam may give rise to a number of nuclear reactions such as (p,γ), (p,n), (p,p'), or even (p,fission) in addition to elastic scattering. The relative yields from these reactions depend on the structure of the target nucleus and the energy of the incident proton.

The various reaction configurations represent final states of a system of A+1 nucleons where the target has mass number A. These final states are often referred to as decay 'channels'. If discussion is limited to two-body reactions, a reaction channel 'c' may be more precisely defined as the decay of the compound nucleus into two parts; α_1 and α_2. Here α is a label for a nuclear configuration with a certain mass, charge and total spin J, in a particular state of internal excitation. The decay fragments exist in a certain quantum state defined by $(\ell m s \nu)$, where ℓ is the relative orbital angular momentum with z-projection m and s is the channel spin defined by

$$\underset{\sim}{S} = \underset{\sim}{J}_1 + \underset{\sim}{J}_2 \qquad (2.2.1)$$

with z-projection ν. The problem is thus reduced to solving the Schroedinger equation for the relative motion of a particular pair of decay products.

A transformation to center of mass coordinates reduces the two body problem to an equivalent one body problem defined by the following parameters.

1) the reduced mass $M_c = m_1 m_2/(m_1 + m_2)$
2) the relative separation r_c between α_1 and α_2
3) the energy of relative motion E_c
4) the wave number $k_c = (2M_c E_c/\hbar^2)$
5) the relative velocity $v_c = \hbar k_c/M_c$

The one-body Schrcedinger equation is written

$$\left[\frac{-\hbar^2}{2M_c}\nabla^2_{\underline{r}_c} + V(\underline{r}_c) - E_c\right]\Psi_c = 0 \qquad (2.2.2)$$

The channel wavefunction Ψ_c describes a particle of mass M_c moving in a potential $V(\underline{r}_c)$. In general $V(\underline{r}_c)$ is a superposition of the Coulomb potential and a short ranged nuclear potential whose exact form is unknown. Since the analytic form of the potential cannot be specified, it can be assumed that space may be divided into two parts; the external region where $r_c > a_c$, and the internal region for which $r_c < a_c$. Here a_c is called the channel radius, which is defined as the distance beyond which the channel fragments experience no mutual nuclear interaction.

In the external region the equations of motion include only the effects of the Coulomb force and can therefore be solved exactly. In spherical coordinates, the Schroedinger equation separates for a product wavefunction of the form

$$\Psi_c^{EXT} = A(\theta_c, \phi_c)\, B(r_c) \qquad (2.2.3)$$

where θ_c and ϕ_c are the polar and azimuthal scattering angles. The angular part of the equation has solutions given by

$$A(\theta_c, \phi_c) = i^{\lambda} Y_{\ell}^{m}(\theta_c, \phi_c)\, \chi_{csv} \qquad (2.2.4)$$

where the Y_λ^m are the spherical harmonic functions and are the channel spin wave functions. These latter functions are constructed by vector coupling the individual particle spin functions. The radial equation is solved by a function of the form

$$B(r_c) = \frac{f_\ell(r_c)}{r_c \sqrt{v_c}} \qquad (2.2.5)$$

$f_\ell(r_c)$ is the solution to the differential equation

$$\frac{d^2 f_\ell}{dr_c^2} + \frac{2M_c}{\hbar^2}(E_c - V_c) f_\ell = 0 \qquad (2.2.6)$$

where

$$V_c = \frac{Z_{a_1} Z_{a_2} e^2}{r_c} + \frac{\hbar^2}{2M_c} \frac{\ell(\ell+1)}{r_c^2}$$

The two terms on the right hand side are the Coulomb and centrifugal potentials, respectively. The external wave function may consequently be expressed

$$\psi_c^{EXT} = \frac{\phi_c(r_c) f_\ell(r_c)}{\sqrt{v_c}} \qquad (2.2.7)$$

Here, the functions

$$\phi_c(r_c) = \frac{i^l Y_l^m(\theta_c, \phi_c)}{r_c} \chi_{csv}$$

are often called surface functions. They form a complete orthonormal set on a spherical surface of radius a_c.

For $E_c > 0$, the equation (2.2.5) can be rewritten in dimensionless form as follows

$$\frac{d^2 f_l}{d\rho_c^2} + \left[1 - \frac{2\eta_c}{\rho_c} + \frac{l(l+1)}{\rho_c^2} \right] f_l = 0 \qquad (2.2.8)$$

Here the Coulomb parameter η_c is given by

$$\eta_c = \frac{Z_{\alpha_1} Z_{\alpha_2} e^2}{\hbar v_c}$$

and

$$\rho_c = k_c r_c$$

The solutions for (2.2.8) are called Coulomb wave functions. There exist two linearly independent f_l, one (F) which is regular and one (G) which is irregular at the origin. These functions have the following asymptotic behavior.

$$F_c = F_{\alpha l} \cong \sin\left[\rho_\alpha - \eta_\alpha \ln(2\rho_\alpha) - \frac{l\pi}{2} + \sigma_{\alpha l}\right] \qquad (2.2.9)$$

$$G_c = G_{\alpha l} \cong \cos\left[\rho_\alpha - \eta_\alpha \ln(2\rho_\alpha) - \frac{l\pi}{2} + \sigma_{\alpha l}\right] \qquad (2.2.10)$$

Here, $\sigma_{\alpha l}$ is the Coulomb phase shift given by

$$\sigma_{\alpha l} = \arg\Gamma(1 + l + i\eta_\alpha) \qquad (2.2.11)$$

Properties and tables of Coulomb wave functions are given in Abramowitz and Stegun (1970). In the absence of the Coulomb field (the case of interest for neutron scattering), F and G are related tc the Bessel and Neumann functions respectively.

For $E_c < 0$, (that is, for closed channels) equation (2.2.5) may formally be rewritten

$$\frac{d^2 f_{u-1/2}}{dz^2} + \left[-\frac{1}{4} + \frac{\chi}{z} + \frac{(1/4 - u^2)}{z^2}\right] f_{u-1/2} = 0 \qquad (2.2.12)$$

by making the substitutions

$$l = u - 1/2$$

$$\chi = -\eta$$

$$z = 2\rho$$

Equation (2.2.12) is called Whittaker's equation and the solutions are the Whittaker functions $W(z;\chi,u)$. Asymptotically these functions vanish at infinity as expected.

$$W \cong e^{(-z/2 + \chi \ln z)} \qquad (2.2.13)$$

The wave functions of natural interest in scattering theory represent incoming (I) and outgoing (O) waves. Linear combinations of Coulomb wave functions having the proper asymptotic behavior may be constructed for open channels as follows

$$I_{c^+} = (G_c - iF_c)\, e^{i\omega_c} \qquad (2.2.14)$$

$$O_{c^+} = (G_c + iF_c)\, e^{-i\omega_c} \qquad (2.2.15)$$

Here $\omega_c = \sigma_{al} - \sigma_{a0}$. For closed channels

$$O_{c^-} = W(2\rho_c; -\eta_c, l+1/2) \qquad (2.2.16)$$

Channel wave functions of unit flux representing incoming and outgoing waves may thus be written

$$\mathcal{I}_c = \frac{\phi_c(r_c)\, I_c^+}{\sqrt{v_c}} \qquad (2.2.17)$$

$$\mathcal{O}_c = \frac{\phi_c(r_c)\, O_c^\pm}{\sqrt{v_c}} \qquad (2.2.18)$$

where the $\pm$ superscript indicates positive (+) or negative (-) energy.

The total wave function in the external region may be constructed by summing an incoming wave in channel c, say, with a superposition of outgoing waves in all channels c'.

$$\Psi_c^{EXT} = \mathcal{I}_c - \sum_{c'} U_{c'c}\, O_{c'} \qquad (2.2.19)$$

Here the coefficients $U_{c'c}$ form the U-matrix. $U_{c'c}$ is the amplitude of an outgoing wave in channel c' associated with an incoming wave of unit flux in channel c.

The differential cross section may be expressed in terms of the U-matrix as follows,

$$d\sigma/d\Omega = |\mathcal{X} + \mathcal{Y}|^2 \qquad (2.2.20)$$

where

$$X = -f_c(\theta_\alpha)\, e^{2i\sigma_0}\, \delta_{c'c}$$

$$f_c(\theta_\alpha) = \left[-\frac{\hbar v_c \eta_c}{4E_c} \operatorname{cosec}^2\left(\theta_c/2\right) \right] \times \qquad (2.2.21)$$

$$e^{\left[-2i\eta_c \ln\{\sin(\theta_c/2)\} + i\pi + 2i\sigma_0\right]}$$

and

$$Y = \left(\frac{i\sqrt{\pi}}{k_c}\right) \times$$

$$\sum_{l'm'l} \left[\sqrt{2l+1}\, \left(e^{2i\omega_c}\, \delta_{c'c} - U_{c'c}\right) Y_{l'}^{m'}(\theta_{\alpha'}, \phi_{\alpha'}) \right] \qquad (2.2.22)$$

X and Y are the Coulomb and nuclear scattering amplitudes. The detailed derivation of equations (2.2.21) and (2.2.22), which are taken from Preston (1962), is too lengthy for inclusion in the present work. For elastic scattering (c=c'), the differential cross section consists of Rutherford scattering, nuclear scattering, and an interference term. For proton energies well below the Coulomb barrier, Rutherford scattering dominates the cross section. The observed line shape in the vicinity of a resonance is due to the interference between X and Y.

Since reaction channels may be experimentally distinguished from each other, the only degrees of freedom

left unspecified are the scattering angles. Knowledge of a specific reaction mechanism is required to predict angular distributions and the relative fraction of collisions which lead to a particular exit channel. This information is parametrized by the U-matrix formalism in terms of the coefficients $U_{cc'}$. Determining an analytic expression for the U-matrix is therefore equivalent to solving the reaction problem.

The U-matrix might be specified by postulating a particular nuclear model and then solving the Schroedinger equation for the resulting potential in the internal region, taking care to match the internal solutions to the external wave functions at the channel boundary. Solutions of this type will depend heavily on the parameters of the model, which at best is an approximation to the actual structure of the nucleus. In order to analyze scattering data without recourse to a particular nuclear model, a more general approach is required. A model independent formulation of the U-matrix was presented by Wigner (1946a, 1946b), and Wigner and Eisenbud (1947). It is called the Derivative Matrix or R-matrix theory of nuclear reactions.

2.3 The R-Matrix

In a comprehensive review, Lane and Thomas (1958) have described R-matrix formalism in detail. The important

features of the theory as it relates to elastic scattering are included in the present work and generalized without proof to the many channel case.

R-matrix theory presumes the existence of a complete orthonormal set of eigenstates $\Psi_{\lambda c}$ for the Hamiltonian in the internal region. If elastic scattering from spin-0 targets is the only reaction considered, the only reaction channels are those of sharp angular momentum ℓ. Dropping the subscript c of the previous section, the channel wave functions may be expressed

$$\Psi_{\lambda \ell m} = \frac{\phi_{\lambda \ell}(r)\, Y_\ell^m}{r} \qquad (2.3.1)$$

where $\phi_{\lambda \ell}$ is the solution to the radial equation

$$\phi''_{\lambda \ell} - \frac{2M}{\hbar^2}\left(V_c + V_n\right)\phi_{\lambda \ell} = -\frac{2M}{\hbar^2} E_{\lambda \ell}\phi_{\lambda \ell} \qquad (2.3.2)$$

The standard abbreviations

$$\phi' = d\phi/dr$$

and

$$\phi'' = d^2\phi/dr^2$$

are used throughout this section.

In equation (2.3.2) V_n is the nuclear potential, V_c is the central potential of section 2, and the $E_{\lambda \ell}$ are the

energy eigenvalues. The boundary conditions

$$\phi_{\lambda l}(0) = 0 \qquad (2.3.3)$$

$$r\,\phi'_{\lambda l}/\phi_{\lambda l}\Big)_{r=a} = B_l \qquad (2.3.4)$$

are sufficient to prove the orthogonality relation

$$\int_0^a \phi_{\lambda l}\,\phi_{\lambda' l}\,dr = \delta_{\lambda\lambda'} \qquad (2.3.5)$$

States ϕ_l of arbitrary energy E may be represented as linear combinations of the $\phi_{\lambda l}$,

$$\phi_l = \sum_\lambda b_{\lambda l}\,\phi_{\lambda l} \qquad (2.3.6)$$

where ϕ_l solves the equation

$$\phi_l'' - \frac{2M}{\hbar^2}(V_c + V_n)\,\phi_l = -\frac{2M}{\hbar^2}E\,\phi_l \qquad (2.3.7)$$

The coefficients $b_{\lambda l}$ may be determined in the following manner. ϕ_l and $\phi_{\lambda l}$ multiply equations (2.3.2) and (2.3.7) respectively. One is then subtracted from the other and the result integrated from r=0 to r=a , giving

$$\int_0^a (\phi_l\,\phi''_{\lambda l} - \phi_{\lambda l}\,\phi_l'')\,dr = \frac{2M}{\hbar^2}(E_{\lambda l} - E)\int_0^a \phi_{\lambda l}\,\phi_l\,dr \qquad (2.3.8)$$

The right hand side of this equation may be evaluated using the orthogonality of the $\phi_{\lambda\ell}$.

$$\int_0^a \phi_\ell \, \phi_{\lambda\ell} \, dr = \sum_{\lambda'} \int_0^a b_{\lambda\ell} \, \phi_{\lambda'\ell} \, \phi_{\lambda\ell} \, dr \qquad (2.3.9)$$

$$= b_{\lambda\ell}$$

The left side may be evaluated using the derivative properties of the Wronskian W, defined as

$$W = \phi_\ell \, \phi'_{\lambda\ell} - \phi'_\ell \, \phi_{\lambda\ell} \qquad (2.3.10)$$

Taking the derivative yields

$$W' = \phi_\ell \, \phi''_{\lambda\ell} + \phi'_\ell \, \phi'_{\lambda\ell} - \phi'_\ell \, \phi'_{\lambda\ell} - \phi''_\ell \, \phi_{\lambda\ell} \qquad (2.3.11)$$

$$= \phi_\ell \, \phi''_{\lambda\ell} - \phi''_\ell \, \phi_{\lambda\ell}$$

and consequently,

$$\int_0^a (\phi_\ell \, \phi''_{\lambda\ell} - \phi_{\lambda\ell} \, \phi''_\ell) \, dr = \Big[W \Big]_0^a \qquad (2.3.12)$$

Using the boundary conditions (2.3.3) and (2.3.4), equation (2.3.8) may then be solved for $b_{\lambda\ell}$.

$$b_{\lambda\ell} = \frac{\hbar^2}{2M} \left[\frac{\phi_{\lambda\ell}(a) \, \phi'_\ell(a)}{E - E_{\lambda\ell}} \right] \left[\frac{B_\ell}{a} \, \frac{\phi_\ell(a)}{\phi'_\ell(a)} - 1 \right] \qquad (2.3.13)$$

Consequently, substituting (2.3.13) into (2.3.6) gives an expression for $\phi_l(a)$ as follows.

$$\phi_l(a) = R_l [a \phi_l'(a) - B_l \phi_l(a)] \qquad (2.3.14)$$

Here the R-function R_l is given by

$$R_l = \sum_\lambda \frac{\gamma_{\lambda l}^2}{E - E_{\lambda l}} \qquad (2.3.15)$$

and the reduced width $\gamma_{\lambda l}^2$ is defined as

$$\gamma_{\lambda l}^2 \equiv \frac{\hbar^2}{2Ma} \phi_{\lambda l}^2(a) \qquad (2.3.16)$$

Equation (2.3.14) shows how the R-function relates the wave function ϕ_l to its derivative at the boundary r=a .

The R-function possesses poles at each energy $E=E_{\lambda l}$. The scattering matrix U_l, expressed in terms of R_l , shows resonance behavior near the energies $E_{\lambda l}$. Matching the boundary conditions for the solution in the external region, given by (2.2.19), and the solution in the internal region gives

$$g_l(a) - U_l f_l(a) = \phi_l(a)$$

$$g_l'(a) - U_l f_l'(a) = \phi_l'(a)$$

Substituting these relations into equation (2.3.14) yields U_l in terms of R_l.

$$U_\ell = \frac{\mathcal{I}_\ell(a)}{O_\ell(a)} \frac{\left[(1 + R_\ell B_\ell) - a R_\ell \left(\mathcal{I}'_\ell(a) / \mathcal{I}_\ell(a) \right) \right]}{\left[(1 + R_\ell B_\ell) - a R_\ell \left(O'_\ell(a) / O_\ell(a) \right) \right]} \qquad (2.3.19)$$

From the defining equations (2.2.14-18) it can be shown that

$$\frac{\mathcal{I}_\ell(a)}{O_\ell(a)} = e^{2i(\omega_\ell - \delta_\ell)} \qquad (2.3.20)$$

where

$$\delta_\ell = \tan^{-1}\left(\frac{F_\ell(a)}{G_\ell(a)} \right)$$

Furthermore, if the L-function is defined in terms of the logarithmic derivative of the outgoing wave function as follows

$$L_\ell = r \frac{O'_\ell(a)}{O_\ell(a)} = S_\ell + i P_\ell \qquad (2.3.21)$$

where S_ℓ is called the shift function and P_ℓ is called the penetrability, then (2.3.20) may be rewritten

$$U_\ell = e^{2i(\omega_\ell - \delta_\ell)} \left[1 + 2i P_\ell \frac{R_\ell}{1 - R_\ell (L_\ell - B_\ell)} \right] \qquad (2.3.22)$$

For an isolated level λ, the R-function can be approximated by

$$R_\ell \cong \frac{\gamma_{\lambda\ell}^2}{E - E_{\lambda\ell}} \qquad (2.3.23)$$

Substitution into (2.3.22) gives

$$U_\ell = e^{2i(\omega_\ell - \delta_\ell)}\left[1 + \frac{i\Gamma_{\lambda\ell}}{E'_{\lambda\ell} - E - i\,\Gamma_{\lambda\ell}/2}\right] \qquad (2.3.24)$$

where the following identifications have been made.

$$\Gamma_{\lambda\ell} = 2P_\ell\,\gamma_{\lambda\ell}^2 \qquad (2.3.25)$$

$$E'_{\lambda\ell} = E_{\lambda\ell} - \Delta_\ell \qquad (2.3.26)$$

$$\Delta_\ell = \gamma_{\lambda\ell}^2 (S_\ell - B_\ell) \qquad (2.3.27)$$

The differential cross section given by (2.2.19) is proportional to $|U|^2$, giving rise to terms of the form

$$|U|^2 = \frac{\Gamma_{\lambda\ell}^2}{(E'_{\lambda\ell} - E)^2 + \Gamma_{\lambda\ell}^2/4} + \cdots \qquad (2.3.28)$$

which is the familiar Breit-Wigner single level formula with laboratory width $\Gamma_{\lambda\ell}$ and center of mass energy $E'_{\lambda\ell}$. It is

important to note that $\Gamma_{\lambda\ell}$ is the product of $\gamma^2_{\lambda\ell}$, which contains the internal structure information, and P_ℓ which describes the external conditions.

The effects of the shift function and the boundary conditions can easily be seen. The amplitude of the radial wave function is maximized in the internal region when

$$B_\ell = r \frac{\phi'_\ell(a)}{\phi_\ell(a)} = 0 \qquad (2.3.29)$$

These are the Wigner-Eisenbud boundary conditions. Under these conditions the resonance energy $E'_{\lambda\ell}$ is shifted by the amount $S_{\lambda\ell}\gamma^2_{\lambda\ell}$ from the actual energy, $E_{\lambda\ell}$, of the internal state. An additicnal shift arising from mismatching at the boundary occurs when $B \neq 0$. These shifts can be made to cancel if

$$B_\ell = S_\ell \qquad (2.3.30)$$

as suggested by Kapur and Peierls (1938). Thus the resonance energies are identical to the energies of the internal states. However, these boundary conditions are energy dependant complex numbers. It is the Kapur-Peierls boundary condition which is useful in the treatment of analogue state fine structure (section 2.5).

Equation (2.3.22) may be rewritten as a matrix equation by defining the following diagonal matrices.

$$\begin{aligned}
\hat{U}_{\mu\nu} &= U_\mu \, \delta_{\mu\nu} \\
\hat{R}_{\mu\nu} &= R_\mu \, \delta_{\mu\nu} \\
\hat{L}_{\mu\nu} &= L_\mu \, \delta_{\mu\nu} \\
\hat{P}_{\mu\nu} &= P_\mu \, \delta_{\mu\nu} \\
\hat{\Omega}_{\mu\nu} &= e^{i(\omega_\mu - \delta_\mu)} \, \delta_{\mu\nu} \\
\hat{W}_{\mu\nu} &= 2i \, \delta_{\mu\nu} \\
\hat{1}_{\mu\nu} &= \delta_{\mu\nu}
\end{aligned} \qquad (2.3.31)$$

The matrix representation of U is then written

$$\hat{U} = \hat{\Omega} \left[\hat{1} + \hat{P}^{1/2} (1 - \hat{R}\hat{L})^{-1} \hat{R} \, \hat{P}^{1/2} \hat{W} \right] \hat{\Omega} \qquad (2.3.32)$$

The generalization to the multi-channel case is straightforward. A complete set of solutions Y_λ to the Schroedinger equation is assumed to exist in the internal region and to be associated with resonances at the eigenvalues E_λ. A set of wave functions $\phi_{\lambda c}(r_c)$ are defined at the channel radius by the overlap integral

$$\phi_{\lambda c}(a_c) = \int_{r=a_c} \phi_c^* \, Y_\lambda \, dS \qquad (2.3.33)$$

where the ϕ_c are defined by (2.2.7) and the $\phi_{\lambda c}$ correspond to the $\phi_{\lambda \ell}$. The boundary conditions are specified by

$$r_c \left.\frac{\phi'_{\lambda c}}{\phi_{\lambda c}}\right|_{r_c=a_c} = B_c \qquad (2.3.34)$$

This leads to an R-matrix which may be non-diagonal and whose elements are defined by

$$\hat{R}_{c'c} = \sum_{\lambda} \frac{\gamma_{\lambda c}\gamma_{\lambda c'}}{E - E_\lambda} \qquad (2.3.35)$$

where

$$\gamma_{\lambda c} = \left(\frac{\hbar^2}{2M_c a_c}\right)^{1/2} \phi_{\lambda c}(a_c) \qquad (2.3.36)$$

If the diagonal matrices $\hat{W}$ and $\hat{P}$ are modified for closed channels as follows

$$\begin{aligned} \hat{W}_{mm} &= 0 \\ \hat{P}_{mm} &= \frac{P_c}{I_c O_c} \end{aligned} \qquad (2.3.37)$$

then (2.3.32) is the correct matrix equation for the multi-channel case.

In practice many approximations are required in the application of (2.3.32). For isolated resonances, where the shifts Δ_λ and widths Γ_λ are small compared to the spacing of the levels, Lane and Thomas show that

$$(\hat{1} - \hat{R}\hat{L})^{-1}\hat{R} \cong \sum_{\lambda} \frac{\gamma_{\lambda c}\gamma_{\lambda c'}}{(E_\lambda - \Delta - E - i\Gamma_\lambda/2)} \qquad (2.3.38)$$

where all open channels contribute to the total width Γ_λ.

$$\Gamma_\lambda = \sum_c \Gamma_{\lambda c} = \sum_c 2 P_c \gamma_{\lambda c}^2 \qquad (2.3.39)$$

The shift Δ_λ is given by

$$\Delta_\lambda = \sum_c (S_c - B_c)\, \gamma_{\lambda c}^2 \qquad (2.3.40)$$

The differential cross section for a particular reaction will have terms of the form

$$\left.\frac{d\sigma}{d\Omega}\right|_{c'c} \cong \sum_\lambda \frac{\Gamma_{\lambda c}\, \Gamma_{\lambda c'}}{(E_\lambda' - E)^2 + \Gamma_\lambda^2/4} \qquad (2.3.41)$$

The resonance cross section is a product of the amplitude $\Gamma_{\lambda c}$ for the formation through the channel c of a state λ and the amplitude $\Gamma_{\lambda c'}$ for the decay of that state through the channel c'. The assumption of a compound nuclear state implies the independence of $\Gamma_{\lambda c}$ and $\Gamma_{\lambda c'}$.

2.4 Statistical Distributions

The compound nucleus described in the previous sections is a complicated mixture of different nucleon configurations. The chance of exciting a particular one varies rapidly with excitation energy. Therefore, the value and sign of $\phi_{\lambda c}(a_c)$ will depend on the randomly distributed

values of a large number of independent variables. Consequently $\gamma_{\lambda c}$, which is proportional to $\phi_{\lambda c}(a_c)$, is expected to have a normal distribution centered at zero. That is, the probability for locating a level in channel c with reduced width amplitude $\gamma_{\lambda c}$ in an interval $d\gamma$ about the value γ is given by

$$P(\gamma)\,d\gamma = \left(\frac{1}{2\pi\langle\gamma^2\rangle}\right) e^{-\frac{\gamma^2}{2\langle\gamma^2\rangle}}\,d\gamma \qquad (2.4.1)$$

where $\langle\gamma^2\rangle$ is the average value of γ^2 in the region of interest. The distribution for the square of a normally distributed variable is given by the well known χ^2 distribution with one degree of freedom. Thus the probability of observing a level of width $\Gamma_{\lambda c}$ in an interval $d\Gamma$ about the value Γ is given by

$$P(x)\,dx = \frac{1}{\sqrt{2\pi x}}\, e^{-\frac{x}{2}}\,dx \qquad (2.4.2)$$

where

$$x = \Gamma/\langle\Gamma\rangle$$

This distribution was suggested by Porter and Thomas (1956).

The distribution of nearest neighbor resonance spacings was investigated by Wigner (1956). A simple although accurate expression was derived from assumptions about the statistical nature of the Hamiltonian matrix elements.

The simplest possible case involves a two dimensional Hamiltonian matrix. Solving the secular equation

$$\hat{H} - \lambda \hat{1} = 0 \qquad (2.4.3)$$

gives the spacing between eigenvalues.

$$|\lambda_1 - \lambda_2| = [(H_{11} - H_{22})^2 + 4 H_{12}^2] \qquad (2.4.4)$$

If only the relative energy spacing is considered, the energy scale may be shifted so that the smaller of the eigenvalues is zero. Let the probability of observing the second level at an energy greater than E=D be given by P(D). If the probability for seeing a level between D and D+dD is given by f(D)dD then the probability p(D) of observing the second level between D and D+dD is

$$p(D)\,dD = P(D) f(D)\,dD \qquad (2.4.5)$$

A differential equation for P(D) may be obtained by integrating (2.4.5).

$$P(D) = \int_D^\infty p(D')\,dD' = \int_D^\infty P(D') f(D')\,dD' \qquad (2.4.6)$$

and therefore

$$\frac{dP}{dD} = - P(D) f(D) \qquad (2.4.7)$$

This equation is trivially integrated to yield

$$P(D) = e^{-\int_0^\infty f(D')\,dD'} \qquad (2.4.8)$$

A functional form for f(D) must be guessed from the statistical distribution of the matrix elements. At this point, a useful geometric construction consists of a cartesian coordinate grid of points (u,t) where $u=2|H_{12}|$ and $t=|H_{11}-H_{22}|$. D will then be the distance from the origin to the point (u,t). The probability f(D)dD is equal to the integral over an annulus of radius D and width dD of the product of the distribution functions for the variables u and t. The simplest possible assumption is that these variables are randomly distributed with equal average densities. The density of points (u,t) is thus uniform over the plane and the integral is just proportional to the area of the annulus so that

$$f(D)\,dD \propto D\,dD \qquad (2.4.9)$$

which leads to the familiar Wigner distribution given by

$$P(z)\,dz = \frac{\pi z}{2} e^{-\frac{\pi z^2}{4}} dz \qquad (2.4.10)$$

where

$$z = D/\langle D \rangle$$

As might be expected, equation (2.4.10) is most accurate for

z small compared to unity, since in that limit the 2x2 Hamiltonian represents a subspace approximately independent of the remaining elements. The most significant feature of (2.4.10) is the low relative probability for very small level spacings. This is often referred to as the 'level repulsion' property of the distribution.

A more general approach to the problem of the statistical distribution of resonance parameters has been summarized by Wilson (1973). This method involves the specification of the joint differential probability for the matrix elements of an N dimensional Hamiltonian. For the diagonalized Hamiltonian, this number may be expressed in terms of the coefficients of the diagonalizing transformation matrix and the eigenvalues of the Hamiltonian. From this expression it is possible to extract width and spacing distributions. For N=2 this method generates the Wigner distribution (2.4.10). For arbitrary N a closed form for the spacing distribution has not been given. However, Monte Carlo calculations for large order Hamiltonians have confirmed the accuracy of the Wigner distribution.

2.5 Analogue States and Fine Structure

The phenomenon of Isobaric Analogue Resonances (IAR) is related to the charge independence of the nuclear force.

Consider a nucleus, referred to as the parent, of mass number A+1 with N+1 neutrons and Z protons (A=N+Z). The bound state spectrum for this nucleus will include a number of states with large single particle components that consist primarily of an unexcited core plus one neutron. The properties of this kind of nuclear configuration are those associated with the single neutron. If the nuclear force is truly charge independent, then exchanging the neutron for a proton will not alter the nuclear properties of the state. Energetically the only difference between the states arises from the extra Coulomb energy of the proton, and the difference in mass between the proton and neutron.

Experimentally, IAR were discovered in just this way. Anderson and Wong (1961) observed strongly populated states in the residual nucleus following (p,n) excitation of several medium to heavy nuclei. These states were identified as analogues of the target ground states. Analogue states were first observed in compound nuclear reactions by Fox, Moore, and Robson (1964) who observed sharp resonances in the proton elastic scattering from ^{88}Sr and ^{89}Y. These were analogues of low-lying states in ^{89}Sr and ^{90}Y, respectively. The manifestation of analogue states in proton elastic scattering may be easily understood in terms of isotopic spin algebra as shown by Robson (1965).

In this formalism, which is mathematically equivalent to spin-1/2 angular momentum algebra, the nucleon is assigned

an isotopic spin t=1/2. The z-projection t_z may be +1/2 or -1/2 for a neutron or proton, respectively. The total isospin T of a system of A nucleons (A=N+Z) is given by the vector sum

$$\underset{\sim}{T} = \sum_{i=1}^{A} \underset{\sim}{t}_i \qquad (2.5.1)$$

with

$$T_z = \sum_{i=1}^{A} t_{z_i} = \frac{1}{2}(N-Z) \qquad (2.5.2)$$

These two quantum numbers completely specify an isotopic spin state of sharp T.

Several operators may be defined in terms of their effects on such states.

$$\hat{T}^2 |T, T_z\rangle = T(T+1) |T, T_z\rangle \qquad (2.5.3)$$

$$\hat{T}_z |T, T_z\rangle = T_z |T, T_z\rangle \qquad (2.5.4)$$

$$\hat{T}_\pm |T, T_z\rangle = \sqrt{(T \mp T_z)(T \pm T_z + 1)}\ |T, T_z \pm 1/2\rangle \qquad (2.5.5)$$

Charge conservation requires that T_z be a constant of the motion, but total isospin is only conserved by the nuclear portion of the Hamiltonian. In the following discussion isospin conservation is assumed to first order.

Consider the proton elastic scattering from an even-even target ${}_N C_Z$ with Z protons and N neutrons. The compound nucleus formed in this reaction is associated with an

excited state of the daughter nucleus ${}_{N}D_{Z+1}$. Analogue states are observed as resonances with anomalously large widths at center-of-mass excitation energies E_p such that

$$E_p = \Delta E_c - B_n + E_x - \delta \qquad (2.5.6)$$

as shown in figure 2.1. ΔE_c is the Coulomb energy difference between the analogue and parent states and δ is the neutron-proton mass difference. B_n is the neutron separation energy of the parent nucleus and E_x is the excitation of the parent state.

The parent state isospin wave function represents a neutron coupled to the core nucleus ${}_{N}C_{Z}$. Since the core has isospin $T=T_z=T_0$, the parent state may be expressed

$$\begin{aligned} |nC\rangle &= |n\rangle|C\rangle \\ &= |1/2, 1/2\rangle |T_0, T_0\rangle \\ &= |T_0+1/2, T_0+1/2\rangle \end{aligned} \qquad (2.5.7)$$

This is a state of pure isospin $T_>=T_0+1/2$. The analogue state is formed by exchanging a proton for a neutron in the parent state. Formally, this is equivalent to applying the isospin lowering operator to the parent state.

$$|ANALOGUE\rangle = \hat{T}_- |nC\rangle = (2T_0+1)^{1/2} |T_>, T_0-1/2\rangle \qquad (2.5.8)$$

In contrast, the ordinary excited states of the daughter have isospin $T_<=T_z-1/2$. The analogue is therefore a special state which differs from the daughter in total

Figure 2.1 The energy level diagram of parent and daughter nuclei.

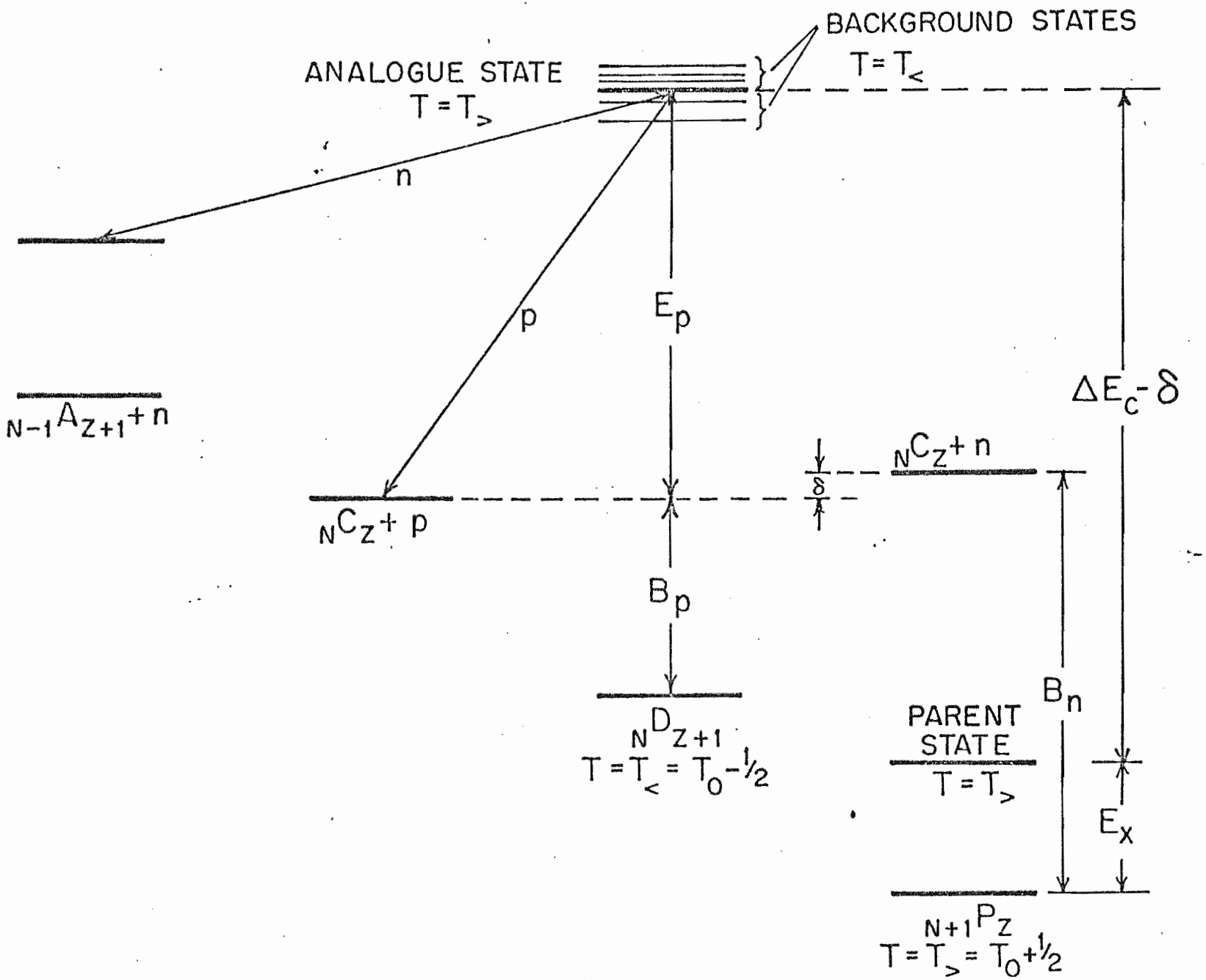
BACKGROUND STATES
T = T<
ANALOGUE STATE
T = T>
n
p
Ep
ΔEc - δ
N-1AZ+1 + n
NCZ + n
δ
NCZ + p
Bp
Bn
NDZ+1
T = T< = T0 - ½
PARENT STATE
T = T>
Ex
N+1PZ
T = T> = T0 + ½

isospin. It is observed in the excitation spectrum of the daughter because the compound nucleus is a linear combination of sharp isospin states. Coupling a proton to the core gives

$$|pC\rangle = |\tfrac{1}{2},-\tfrac{1}{2}\rangle |T_0,T_0\rangle$$
$$= \frac{1}{\sqrt{2T_0+1}} \left(|T_>,T_<\rangle + \sqrt{2T_0}\,|T_<,T_<\rangle \right) \qquad (2.5.9)$$

Clearly, the compcund nucleus is made up of a part which may couple to the daughter ($T_<$) and a part which may couple to the analogue ($T_>$).

The structure of the analogue state itself may be examined by decomposing its isospin wave function.

$$|\text{ANALOGUE}\rangle = |\tfrac{1}{2},-\tfrac{1}{2}\rangle |T_0,T_0\rangle + \sqrt{2T_0}\,|\tfrac{1}{2},\tfrac{1}{2}\rangle |T_0,T_0-1\rangle$$
$$= |pC\rangle + \sqrt{2T_0}\,|nA\rangle \qquad (2.5.10)$$

Here $|nA\rangle$ represents a neutron coupled to the analogue of the target ground state ${}_{N+1}A_{Z-1}$. As shown in figure 2.2, these states have two-particle, one-hole configurations. The coefficients of equation (2.5.10) arise from the fact that in addition to the single particle neutron, there are $2T_0$ excess neutrons in the core which may be exchanged for a proton without violating the Pauli exclusion principle. The analogue state may therefore decay through neutron or proton emission. The total width of the analogue state is expected to be comparable with the single particle width of the

Figure 2.2 The particle-hole picture of the analogue state.

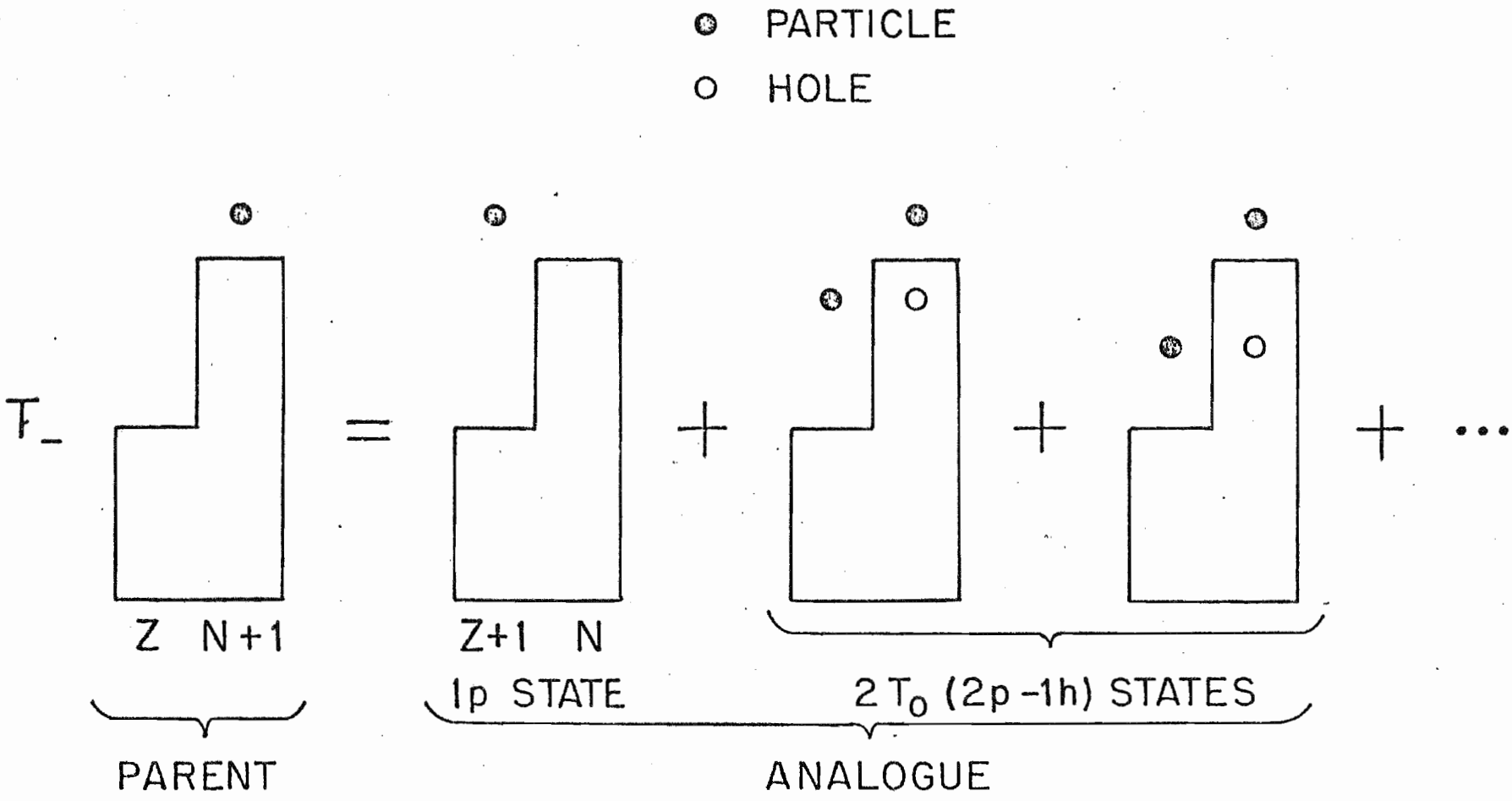
PARTICLE
HOLE
T_
=
+
+
+
...
Z N+1
Z+1 N
1p STATE
2 T0 (2p-1h) STATES
PARENT
ANALOGUE

parent state. If none of the decay channels are preferred, then the width of the IAR in the elastic channel is given by

$$\gamma_p^2 = \frac{\gamma_n^2}{2T_0+1} \qquad (2.5.11)$$

where γ_n^2 is the parent state reduced width.

The analogue (equation 2.5.10) is one eigenstate of the isospin dependant optical model potential of Lane (1962).

$$U = U_0 + U_1 (\underset{\sim}{t} \cdot T_0) \qquad (2.5.12)$$

There exists another eigenstate which is orthogonal to the analogue and is often called the anti-analogue. It has isospin $T_<$ and its wave function is given by

$$|\text{ANTI-ANALOGUE}\rangle = \sqrt{2T_0}\,|pC\rangle - |nA\rangle \qquad (2.5.13)$$

The isospin dependance of the Hamiltonian splits the two states energetically by the amount ΔE,

$$\Delta E = (T_0 + 1/2)\,U_1 \qquad (2.5.14)$$

which usually results in the anti-analogue being bound. Thus it is typically observed in the reaction C(^{3}He,d)D, and has a reduced width of approximately

$$\gamma^2_{He,d} = \frac{2T_0}{2T_0+1}\,\gamma_n^2 \qquad (2.5.16)$$

Implicit in this treatment is the assumption that the only role of the Coulomb force is to energeticly differentiate the analogue from the parent. This can only

be true if the total isospin operator commutes with the Hamiltonian. This is a fair approximation inside the channel radius (Henley, 1969) but cannot be true in the external region since the Coulomb force quite obviously distinguishes a proton from a neutron. States of pure isospin $T_>$ and $T_<$ do not represent an acceptable basis for the decomposition of $|\rho C\rangle$ in the external region. Here the natural states have mixed isospin and may couple either to the analogue or the the background daughter states. This isospin channel coupling has the effect of sharing the strength of the analogue with the neighboring background states of the same spin and parity. The width distribution of these levels constitutes the fine structure of the analogue state.

The degree of isospin mixing in the Robson theory is characterized by the difference in boundary conditions at the channel radius between the internal and external R-matrix wave functions. The result, as shown in figure 2.3, is an asymmetric enhancement of the $T_<$ background levels in the vicinity of the $T_>$ level.

Mello (1967) has derived the Robson asymmetry by assuming states of mixed isospin throughout configuration space. The spreading of the analogue strength is interpreted as a giant resonance induced by external mixing.

The most complete treatment of analogue state fine structure is given by Lane (1969) as a special case of line

Figure 2.3 A schematic representation of the enhancement of background states in the vicinity of an analogue due to isospin mixing.

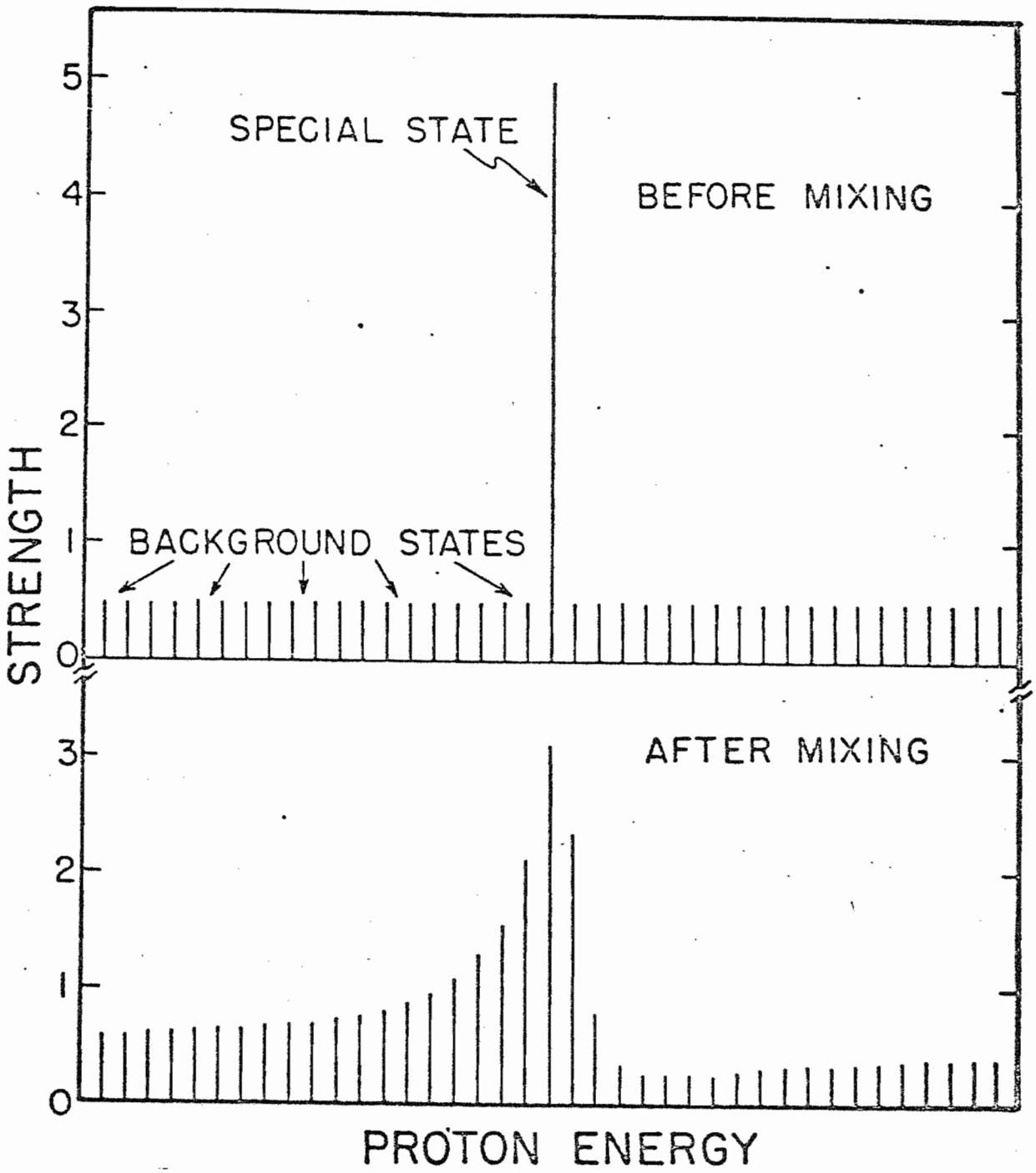
SPECIAL STATE
BEFORE MIXING
BACKGROUND STATES
AFTER MIXING
STRENGTH
PROTON ENERGY
5
4
3
2
1
0
3
2
1
0

broadening theory. Lane treats both external and internal mixing within the Kapur and Peierls R-matrix framework.

This formalism describes the effects on background states η due to the presence of an analogue state λ. The analogue is an eigenstate of the approximate Hamiltonian H_o. The actual Hamiltonian H has eigenstates ν which coincide with the η states far from the analogue. The mixing of the analogue with the background is the result of the residual interaction h defined by

$$h = \Delta H + \Delta \mathcal{L} \qquad (2.5.16)$$

In this equation H is the difference between H and H_o, and causes internal mixing while $\Delta \mathcal{L}$ is the difference in boundary conditions and results in external mixing.

The solution to the fine structure problem is given in terms of the strength function

$$S(E) = \langle \gamma^2 \rangle_\rho$$

where $\langle \gamma^2 \rangle$ is the average reduced width and ρ is the average level density. The widths are averaged over an interval small compared with the spreading width of the analogue state. The form of the solution depends on the degree of isospin mixing as defined by the parameter λ.

$$\lambda = \frac{\Gamma_\lambda^\downarrow / \pi}{\sqrt{\langle D \rangle^2 + 1/4 (\Gamma_\lambda^\downarrow)^2}} \qquad (2.5.18)$$

where

$\Gamma_\lambda^\dagger$ = analogue natural decay width

$\langle D \rangle$ = average spacing of the η states

$\Gamma_\lambda^\downarrow = 2\pi(\langle \eta | h | \lambda \rangle)^2 / \langle D \rangle$, the mixing width

Strong mixing is implied by $\lambda >> 1$ and weak mixing by $\lambda << 1$. In the case of strong mixing, when the analogue is completely dissolved among the fine structure fragments, Lane obtains

$$S(E) = S_0 \left[\frac{(E_A - \Delta - E)^2 + \omega^2/4}{(E_R - E)^2 + 1/4\, W_0^2} \right] \qquad (2.5.19)$$

where s_0 is the strength function of the background levels η. E_A is the observed energy of the analogue and W_0 is the spreading width.

$$E_A = E_\lambda + \langle \lambda | h | \lambda \rangle + P \int_{-\infty}^{\infty} \frac{[\langle \eta | h | \lambda \rangle]_\epsilon^2 \rho_\eta(E)}{E' - E} dE' \qquad (2.5.20)$$

$$W_0^2 = (\Gamma_\lambda^\downarrow)^2 + 2 \frac{\Gamma_\lambda^\downarrow \langle D \rangle}{\pi} \qquad (2.5.21)$$

The asymmetry of the distribution is characterized by Δ, where

$$\Delta = \frac{1}{\pi S_0} \left[\left(\gamma_\lambda - P \int_{-\infty}^{\infty} \frac{[\gamma_\eta \langle \eta | h | \lambda \rangle]_\epsilon^2 \rho_\eta(E)}{E' - E} dE' \right) \times \pi \left[\gamma_\eta \langle \eta | h | \lambda \rangle \right]_\epsilon \rho_\eta(E) \right] \qquad (2.5.22)$$

The parameter ω may be expressed in terms of the other fine structure parameters as follows

$$\omega^2 \simeq W_o^2 - 4\Delta^2 + \frac{2 W_o^2 \gamma_A^2}{\pi S_o} \qquad (2.5.23)$$

where γ_A^2 is the excess reduced width due to the presence of the analogue.

$$\gamma_A^2 = \int S(E)\, dE - \sum_\eta \gamma_\eta^2 \qquad (2.5.24)$$

The integral covers an energy interval large compared to the spreading width.

For strong mixing the parameter R defined as

$$R = \frac{S(E+\Delta)}{S(E-\Delta)} = \frac{1+3r}{1-r} = 1 + 16\,\frac{\Delta^2}{\omega^2}. \qquad (2.5.25)$$

where

$$r = \frac{[\gamma_\eta \langle \eta | h | \lambda \rangle]_E^2}{[\gamma_\eta]^2\, [\langle \eta | h | \lambda \rangle]_E^2} \qquad (2.5.26)$$

is a measure of the asymmetry. The value of r lies between 0 and 1, and depends upon the correlation between $\langle \eta | h | \lambda \rangle$ and γ_η. The greatest correlation ($\langle \eta | h | \lambda \rangle / \gamma_\eta$ = constant) gives r=1 and R=∞, which are the values corresponding to the largest possible asymmetry. This occurs when h is dominated

by external mixing in one channel (a sufficient but not necessary condition). In this case $\omega^2 = 0$, and equation (2.5.19) becomes identical with the Robson expression. Internal mixing is characterized by a non-zero value of ω^2. The ratio

$$\frac{\omega^2}{4\Delta^2} \cong \frac{1-r}{r} \qquad (2.5.27)$$

is considered a measure of the internal relative to the external mixing. In general a strong asymmetry is the characteristic of external mixing.

In the case of weak mixing, the distribution is quite narrow and is dominated by a single strong level. Apart from the dominant level, this distribution has a Breit-Wigner contour, as does the strong mixing solution. For intermediate mixing a general solution has not been given but Lane solves the special case of uniform level spacing. The resulting distribution is somewhat more peaked in the center than a Breit-Wigner shape. Unfortunately the level spacings are expected to assume a Wigner distribution, and thus the solution for the uniform model is of little practical value. However, it has been shown by Lane et al. (1974) that equation (2.5.19) may be applied in the intermediate mixing case if S(E) is interpreted as an ensemble strength function. This means that S(E) gives the most probable value of the strength function for an ensemble of fragmented analogues defined by a given set of parameters

E_A, W_o, γ_A^2, s_o and Δ.

The procedure for fitting equation (2.5.19) to the experimental data and extracting values for the fine structure parameters is discussed in section 4.4.

2.6 Spectroscopic Factors

The single particle parent states described in section 2.5 are not the only bound states in the parent nucleus. In general there are many levels, corresponding to more complicated nuclear configurations, lying between the single particle states. These levels are observed because there exists a residual two-body nuclear interaction between the core nucleons and the excess neutron. In the same way an analogue state is fragmented among the background levels by the Coulomb interaction, this residual nuclear interaction tends to spread the single particle strength among the background levels of the same spin and parity and gives rise to giant resonances in the strength function. The neutron spectroscopic factor is defined by

$$S_{dp} = \frac{\gamma_n^2}{\gamma_{s.p}^2} \qquad (2.6.1)$$

where γ_n^2 is the reduced width of the parent state and γ_{sp}^2 is the single particle reduced width. γ_n^2 is usually obtained by studying the C(d,p)P reaction. The spectroscopic factor is a measure of the residual interaction. A strong

interaction dissipates much of the single particle strength among the background levels resulting in a small spectroscopic factor. Conversely weak residual interactions are associated with spectroscopic factors near unity. The proton spectroscopic factor for an analogue state is defined by

$$S_p = (2T_0+1)\frac{\Gamma_p}{\Gamma_{sp}} \qquad (2.6.2)$$

where $\Gamma_p = 2P\gamma_a^2$ and P is the Coulomb penetrability. Recalling equation (2.5.11), it is clear that S_{dp} should equal S_p (to within $(2T+1)^{-1}$). It is interesting that this proves not to be the case. In figure 2.4, (S_{dp}, S_p) is plotted for more than 40 analogues measured at TUNL. The best fit straight line through the data has a slope of 0.64±0.03. The proton spectroscopic factors are systematically smaller than their neutron counterparts. No consistent theoretical explanation has been presented for this discrepancy.

Figure 2.4 A plot of the points $(S_{d\rho}, S_{\rho})$ for more than 40 analogues studied at TUNL, showing the systematic behavior: $S_{d\rho} > S_{\rho}$.

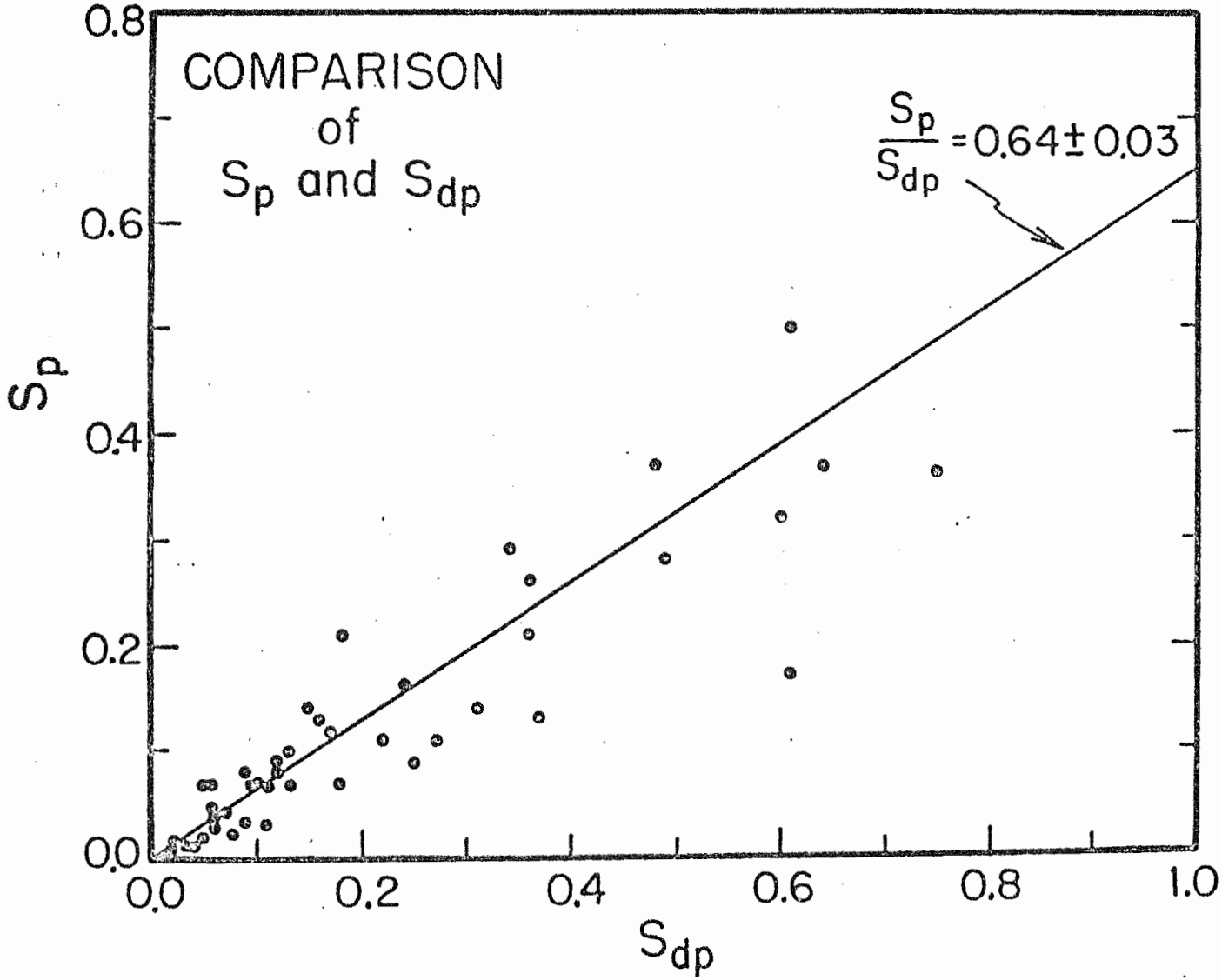
COMPARISON
of
S_p and S_{dp}
$\frac{S_p}{S_{dp}} = 0.64 \pm 0.03$
S_p
S_{dp}
0.0
0.2
0.4
0.6
0.8
1.0

Chapter 3

EXPERIMENTAL EQUIPMENT AND PROCEDURES

3.1 The Accelerator Control System

In order to facilitate high resolution proton elastic and inelastic scattering studies at energies greater than those available in the TUNL 3-MV Van de Graaff laboratory, an improved energy stabilization system was developed for the TUNL tandem accelerator. With this equipment overall experimental energy resolution of 400 to 450 eV was obtained for the measurement of the ^{90}Zr elastic scattering cross section.

In contrast with the 3-MV laboratory analyzer-homogenizer system originally described by Parks et al. (1958), and with the neutral beam homogenizer system of Dzubay et al. (1972), the triple loop terminal regulator employs neither an auxilliary beam nor a target correction voltage. Instead, high voltage modulation of the terminal charge exchange stripper is employed to null residual

machine energy fluctuations. The feedback signal is transmitted to the terminal via an intensity modulated light beam. This additional control loop thus has no inherent frequency response limitation such as the ion drift time associated with the conventional corona control arrangement. Several authors (Bloch et al. (1967), Roth and Weitkamp (1974), and Cairns et al. (1974)) have described systems similar in operating principles to the one at TUNL. However its adaptation for high resolution proton reaction studies is unique, and represents the 'state of the art' in performance and reliability in the 3-7 MeV energy range.

A schematic diagram of the control system superimposed on an abbreviated floor plan of the laboratory is shown in figure 3.1. Briefly, the system is configured as follows: An error signal proportional to the machine energy fluctuations is derived from the current intercepted by a pair of control slits downstream from the double 90° analyzing magnets. In order to insure that all of the energy information is retained in the signal, a matched pair of fast low-noise slit current preamplifiers was designed and constructed. These amplifiers have a logarithmic gain characteristic which renders the error signal insensitive to beam intensity fluctuations. Unfortunately this quality leaves the preamplifiers vulnerable to electron cross talk from the control slits. To eliminate this problem, the control slits were offset about four inches along the beam

Figure 3.1 A schematic diagram of the three loop control system.

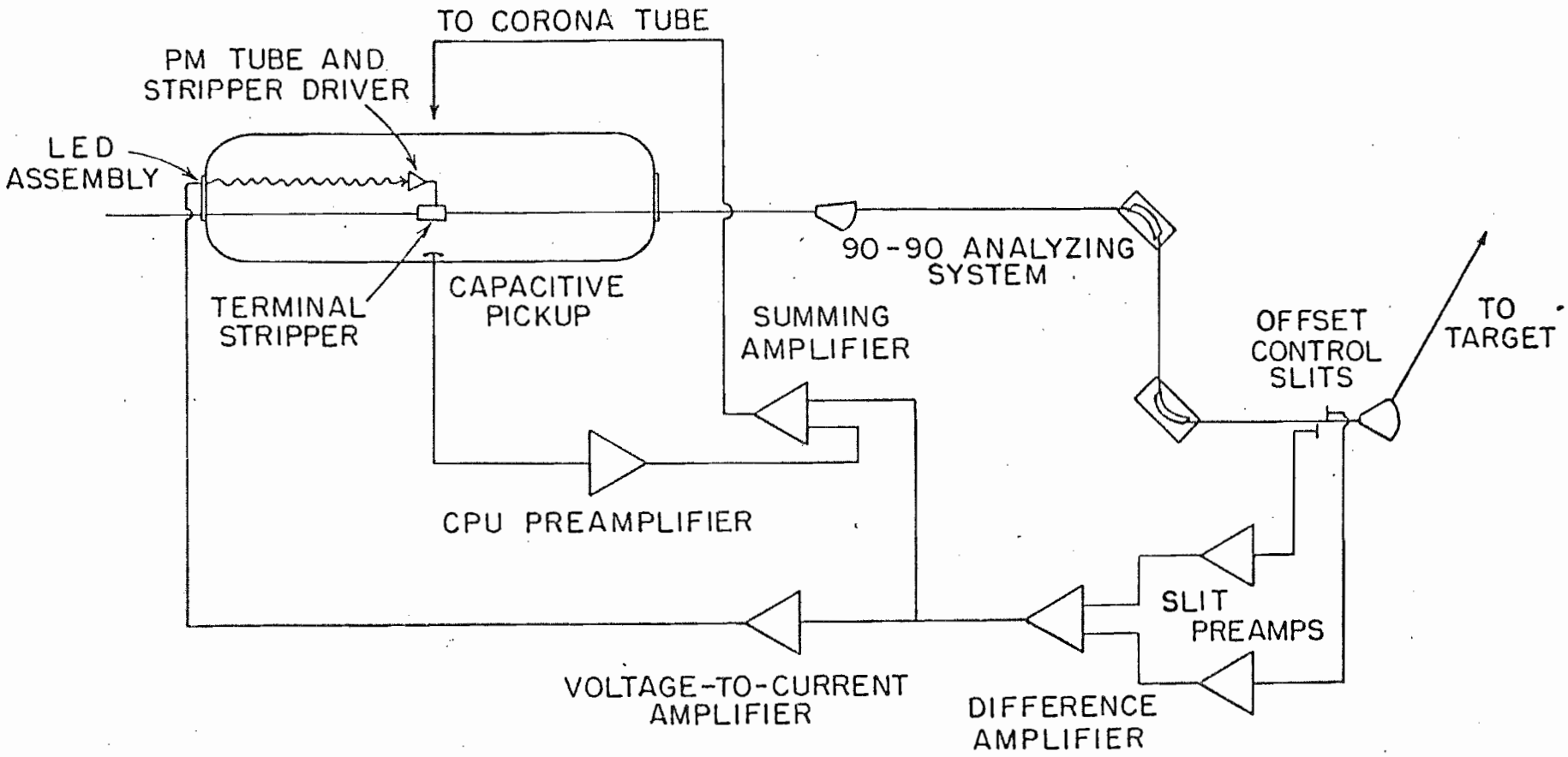

TRIPLE LOOP CONTROL SYSTEM

axis. The control signal is developed from the two slit signals by a difference amplifier. It is then summed with the signal from the capacitive pickup and applied to the corona tube grid. This much of the control system is similar to that described by Gere et al. (1967). In addition, the slit signal is encoded in a light beam by a voltage-to-current converter which drives a light emitting diode (LED). A small objective lens focuses the beam through a port at the low energy end of the accelerator pressure tank. Within the terminal, a collecting lens focuses the light upon a photomultiplier tube which converts the light intensity fluctuations back into a voltage signal. This in turn drives the high voltage terminal amplifier whose output is capacitively coupled to the stripper. The terminal amplifier is capable of six kilovolt peak to peak output swings. The system may be operated with either foil or gas stripping.

In some cases, it is desirable to adjust the fast feedback loop gain to zero. This results in a Gere type control system very similar to the one in use at TUNL previously. In this configuration a signal from the generating voltmeter (GV) may be substituted for the control slit signal in the corona tube loop. Operation in this manner is called 'GV' control as opposed to 'SLIT' control, and requires no control slit signal. A control mode called 'AUTO' is available which automatically switches from 'SLIT'

control to 'GV' control if the total control slit current falls below a certain minimum. Thus if the beam on the control slits is lost for any reason, the accelerator will switch to 'GV' control and large terminal voltage excursions which often result in tank sparks may be avoided. However, the 'GV' mode is unsuitable for use with the fast feedback channel, which requires a stable control slit signal. Thus it is unsuitable for high resolution work. Consequently the present work includes a detailed analysis only for the slit control mode of operation.

The standard procedure for quantifying the description of a feedback network is to build a frequency domain model of the system. The inputs to the model represent the unregulated fluctuations in one or more measurable quantities. In this case the variables of interest are the terminal voltage and the beam energy. The output of the model represents the input quantities after feedback processing. The model itself amounts to a description of the feedback paths in terms of transfer functions that describe the processing of sinusoidal signals by an element or sequence of elements of the system. In general a transfer function is a complex number that is a function of frequency. The modulus of the function corresponds to the gain and the argument gives the phase of the outgoing signal relative to the incoming signal. The response of the entire system to a sinusoidal excitation of arbitrary frequency may

be deduced by solving a series of loop equations in much the same way as one solves an RLC network. The performance and stability of the feedback system is then analyzed in terms of ratios of the regulated output quantities to the corresponding input quantities. These ratios are called regulation factors. In principle the problem of a general periodic excitation is then solved since such a signal may be decomposed into its Fourier components.

The analysis of the 3-loop regulator is best begun by considering the 2-loop Gere type terminal regulating system. The model for this system will illustrate the limitations of this design and can easily be expanded to represent the present system. Figure 3.2 shows a block diagram of the Gere arrangement. The unboxed variables represent measurable parameters at various points in the system.

ΔV_{t_o} = the unregulated terminal voltage fluctuations

ΔV_t = the regulated terminal voltage fluctuations

ΔE = the regulated beam energy fluctuations

Δr = the fluctuation in beam position at the control slits due to ΔE

The ΔV_{t_o} arise primarily from charge migration on the Van de Graaff charging belt. This results in a periodic terminal voltage fluctuation at the belt frequency (about 2 Hz). The amplitude of these fluctuations is typically 10 to 20 kV.

Figure 3.2 The frequency domain model for the conventional Gere type terminal regulating system.

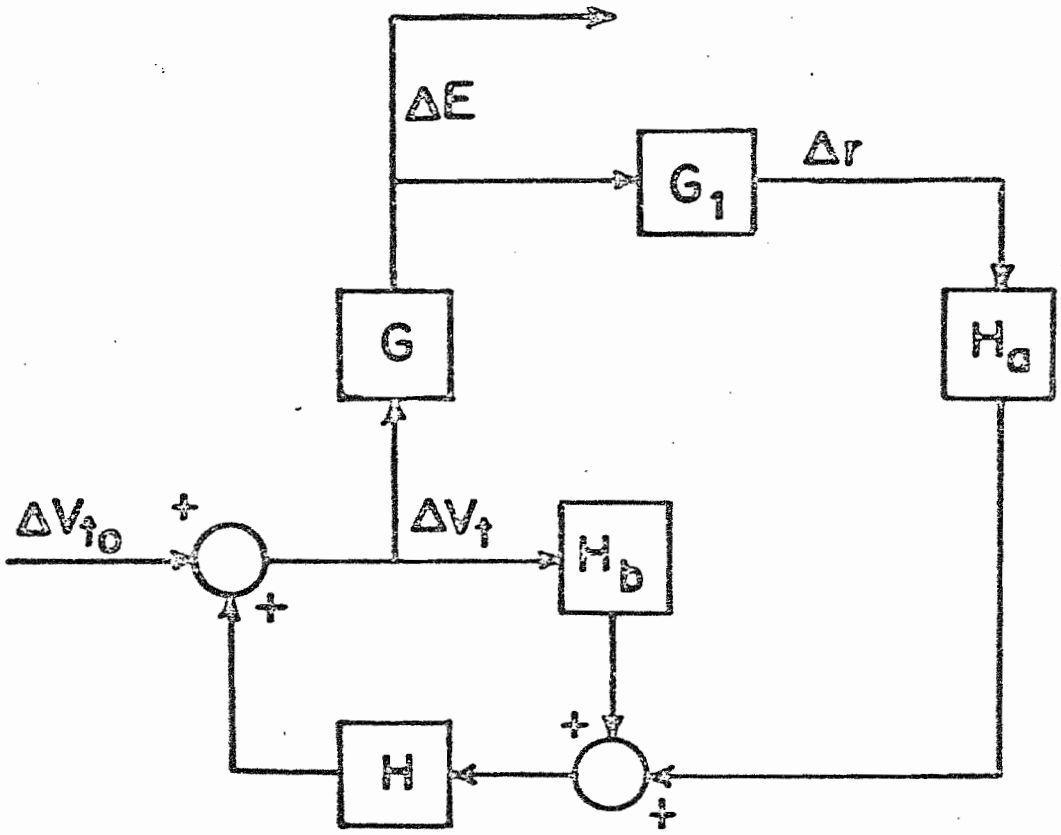
ΔE
G1
Δr
G
Ha
ΔVto
+
ΔVt
HD
+
+
H
+
+

The boxed variables represent the transfer functions of the various system components.

G = the conversion factor between terminal voltage and beam energy

G_1 = the spatial energy dispersion of the analyzing magnets

H_a = the transfer function of the path from control slits to summing amplifier

H_b = the transfer function of the path from capacitive pickup to summing amplifier

H = the transfer function of the path from corona tube grid to terminal

The circles represent signal sum points. G is given by

$$G = -q_1 + q_2 \qquad (3.1.1)$$

where q_1 is the negative beam charge state and q_2 is the positive beam charge state.

The network equations for the model are given by

$$\Delta E = G\Delta V_t \qquad (3.1.2)$$

$$\Delta V_t = \Delta V_{t_0} + H(\Delta V_t H_b + \Delta V_t G G_1 H_a) \qquad (3.1.3)$$

These equations may be rewritten in terms of the appropriate regulation factors as follows.

$$\frac{\Delta V_t}{\Delta V_{t_o}} = \frac{\Delta E}{G \Delta V_{t_o}} = \frac{1}{1 + A} \qquad (3.1.4)$$

The open loop frequency response A is given by

$$A = - H(H_b + GG_1 H_a) \qquad (3.1.5$$

The operational concepts behind the design of the two loop control system are clear from the form of A. The second term, $-HGG_1 H_a$, is the open loop response of the path from the control slits to the terminal via the corona tube. Gere and his collaborators assumed that an error signal derived from control slits was accurate only for frequencies less than about 0.5 Hz. This loop was intended to regulate only very slow drifts in terminal voltage. Consequently the frequency response of the slit current preamps was rolled off sharply at a very low frequency. A feedback signal for higher frequencies is required to regulate terminal fluctuations at the belt frequency. This is the purpose of the CPU to corona channel. By nature the CPU is an ac sensor. The two terms of A represent feedback in different frequency bands peculiar to the different methods of extracting the error signals.

The basic difficulty with this method of terminal regulation is associated with the signal path from corona tube grid to terminal. This path is characterized by the transfer function H. It has been shown by Cairns (1973)

that

$$H(s) = K\left[\frac{(1-e^{-s\tau})}{s\tau}\right]\left[\frac{1}{(1+sRC)}\right] \qquad (3.1.6)$$

in the approximation of a constant radial electric field gradient between the terminal and tank wall. The substitution $s=j\omega$, where $j=\sqrt{-1}$ and ω is the angular frequency, is made in (3.1.6). In this expression τ is the average drift period associated with ion transit from the corona points to the terminal. For an FN tandem filled with a mixture of CO_2 and N_2, is approximately 30 msec. C is the terminal capacitance (about 100 pf) and R is the equivalent resistance of the low and high energy column resistor stacks (about 30,000 MΩ). K is an adjustable gain parameter. Takacs (1972) has shown that some complication is introduced by considering the exact form of the radial field, particularly at high terminal voltage where the corona points are retracted to a position near the tank wall. However, the basic properties of H may be deduced from a Bode plot cf equation (3.1.6) in which H in decibels and the phase angle ϕ_H (equal to arg(H)) are plotted against log(f), where $f=\omega/2\pi$. This is shown in figure 3.3 with K=1. Stability requires that the open loop gain not exceed unity when the phase shift $\phi_H=-180°$. A practical design guideline fixes the unity gain point at a frequency where

Figure 3.3 A Bode plot of the unity gain frequency response for the signal path from the corona tube grid to the terminal.

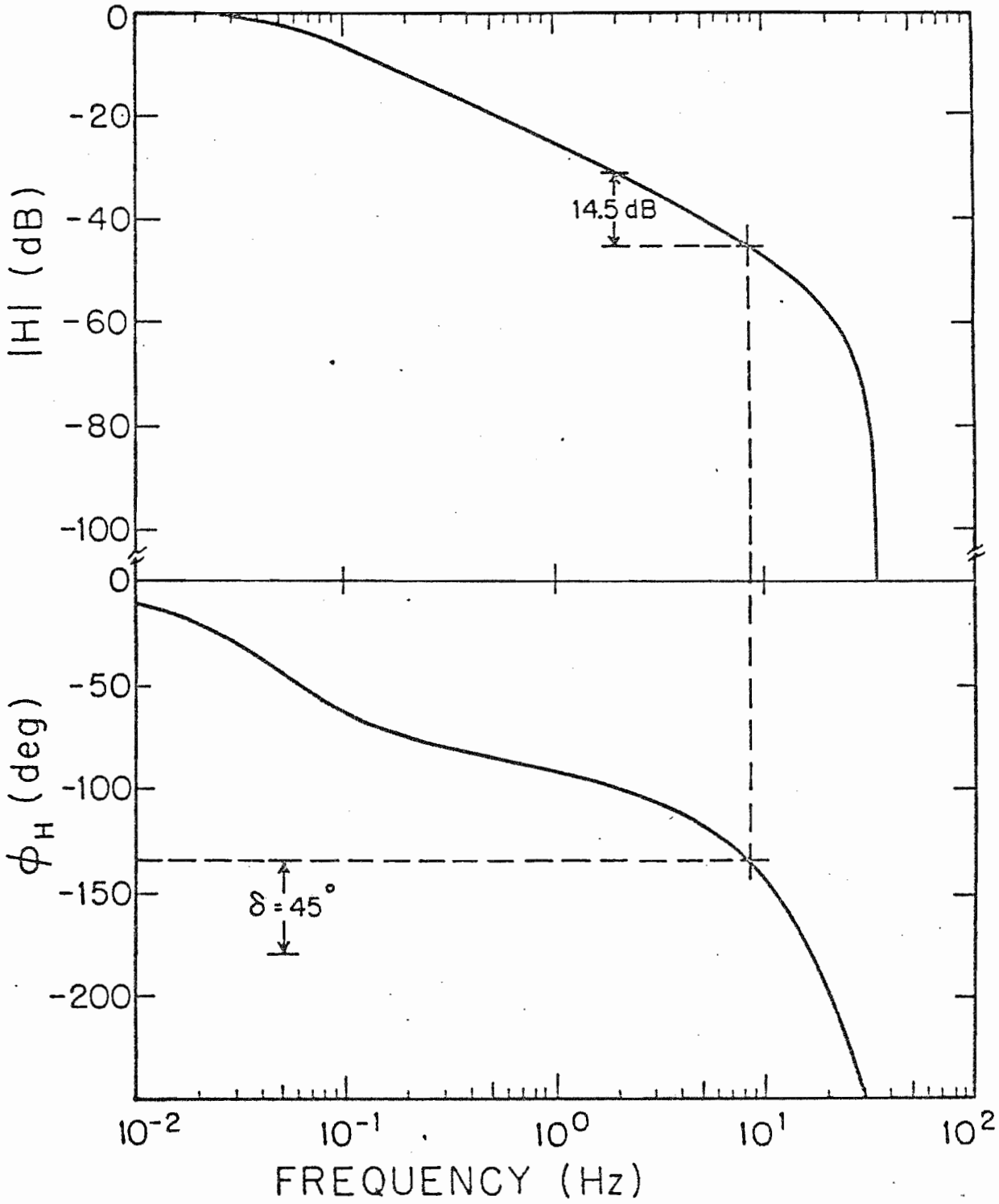
0
-20
-40
-60
-80
-100
|H| (dB)
14.5 dB
0
-50
-100
-150
-200
ϕ_H (deg)
δ = 45°
10^{-2}
10^{-1}
10^{0}
10^{1}
10^{2}
FREQUENCY (Hz)

$$\phi_H = -180° + \delta \qquad (3.1.7)$$

The phase margin δ is usually on the order of 45°. If the energy sensor combination is approximated by a constant, say

$$H_b + G G_1 H_a = 1 \qquad (3.1.8)$$

then figure 3.3 also represents the complete open loop frequency response A. The unity gain frequency is approximately 8.5 Hz which means the gain at the belt frequency can be as high as 14.5 dB. Under these conditions an open loop terminal ripple of 10 kV will be reduced to about 1.6 kV. A gain of 46 dB is available for stabilization against slow terminal drifts with frequencies less than 0.2 Hz. The performance of the two loop system can be improved slightly by introducing an additional phase lead in H_a. However it is difficult to achieve stable operation with a belt frequency gain greater than about 20 dB. This still leaves a kilovolt or more of terminal ripple with strong components at 2 Hz and 30 Hz. For a proton beam this translates into energy fluctuations of at least 2 keV.

An energy spread of this size is clearly unacceptable for high resolution experiments which require an overall resolution in the neighborhood of 400 eV. Historically this difficulty has been solved at TUNL with the homogenizer concept. The problem may also be attacked by adding the third loop to the two loop system described above.

The frequency domain model for the three loop regulator is shown in figure 3.4. Here ΔV_s is the stripper modulation signal and H is the transfer function of the signal path from the LED driver to the terminal amplifier. The loop equations (3.1.2) and (3.1.3) now become

$$\Delta E = G(\Delta V_t + G_1 H_a H_c \Delta E) \qquad (3.1.9)$$

$$\Delta V_t = \Delta V_{t_o} + H(H_b \Delta V_t + G_1 H_a \Delta E) \qquad (3.1.10)$$

The regulation factor for the terminal voltage is found by solving (3.1.9) for ΔE and substituting into (3.1.10) giving

$$\frac{\Delta V_t}{\Delta V_{t_o}} = \frac{1}{1 + A_T} \qquad (3.1.11)$$

where the open loop terminal frequency response A is given by

$$A_T = -H\left[H_b + \frac{G G_1 H_a}{(1 - G G_1 H_a H_c)}\right] \qquad (3.1.12)$$

Similarly, the energy regulation factor is found to be

$$\frac{\Delta E}{G \Delta V_{t_o}} = \frac{1}{1 + A_E} \qquad (3.1.13)$$

where A_E is the open loop energy frequency response.

$$A_E = -[H H_b + G G_1 H_a (H + H_c - H_b H_c)] \qquad (3.1.14)$$

Figure 3.4 The frequency domain model for the three loop energy regulating system.

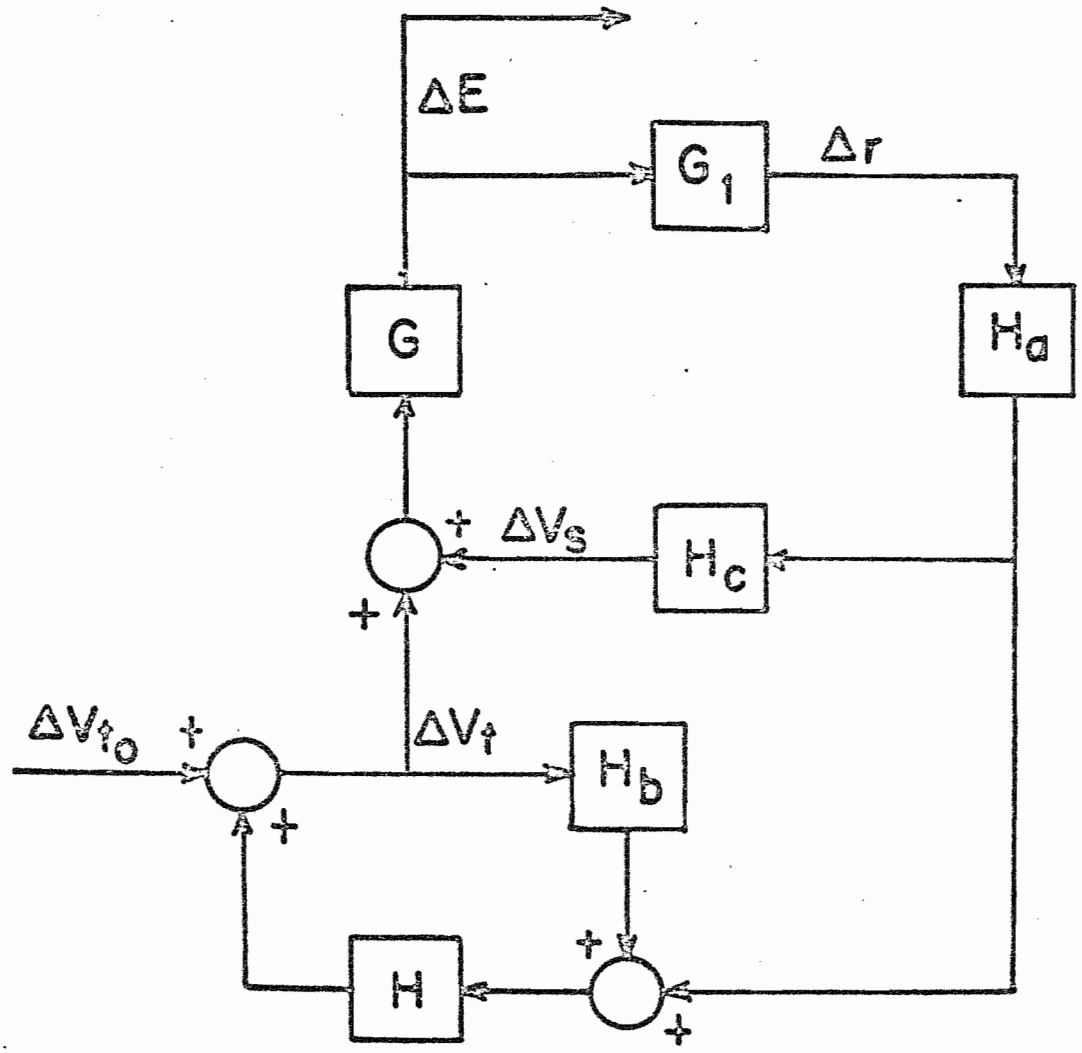
ΔE
G1
Δr
G
Ha
+
ΔVs
Hc
+
ΔVto
+
ΔVt
Hb
+
H
+
+

The regulation factors are clearly no longer identical. The low frequency part of the terminal response is divided by the factor $1-GG_1H_aH_c$. Increasing the fast channel gain (H_c) thus tends to destabilize the terminal against low frequency drifts. This effect can be partially reduced by rolling off the fast channel response at frequencies less than 1 Hz, which is accomplished in the present design by capacitively coupling to the terminal stripper.

The open loop energy response has two additional terms, $-GG_1H_aH_c$ and $GG_1H_aH_bH_c$. The former is the fast channel loop gain. The latter is an interference term between the CPU channel of the corona regulator and the fast feedback channel. Unless H is small compared to unity, this term will induce the 30 Hz oscillation characteristic of the two loop regulator. This requirement need not ruin the terminal regulation if the bandwidth of the control slit error signal can be increased. Experience with the 3 MV laboratory homogenizer has shown that the so-called geometric phase advance is not a significant factor at frequencies up to several kHz. The control slit loading problem discussed by Gere is overcome with the multi-stage design of the slit current preamplifiers. However, if the slit control channel of the corona loop is responsible for feedback at the belt frequency, the fast channel feedback might be expected to destabilize the terminal against belt flop. Fortunately a very wide band of energy fluctuations is removed by the fast

channel feedback. This allows stable operation of the terminal with a much smaller phase margin, say 15° instead of 45°. Consequently the gain of the corona loop may be greatly increased.

Figure 3.5 shows the Bode plot of A_T with the ratio of H/H_c optimized for a phase margin of 15°. The corona channel gain has been increased about 40 dB but the gain at the belt frequency is still only 16 dB. The closed loop terminal fluctuations will still be on the order of one or two kilovolts. The Bode plot for the corresponding energy response A_E is shown in figure 3.6. The gain at the belt frequency is 54 dB which is sufficient to reduce 40 keV open loop fluctuations to 80 eV. This compares favorably with other effects which contribute to the total beam energy resolution.

The qualitative performance of the system is shown in figure 3.7. The top picture is a reproduction of an oscilloscope photograph which shows the terminal voltage, measured by the CPU, and the control slit error signal. The accelerator is in corona control, the fast channel having been turned off. The lower figure shows the same two signals after the system has been retuned with the stripper modulation channel in operation. The fast fluctuations in the slit error signal, which are proportional to the beam energy fluctuations, are reduced to the noise level of the preamplifiers. The high frequency components of the

Figure 3.5 A Bode plot for the triple loop system open loop terminal response (A_T).

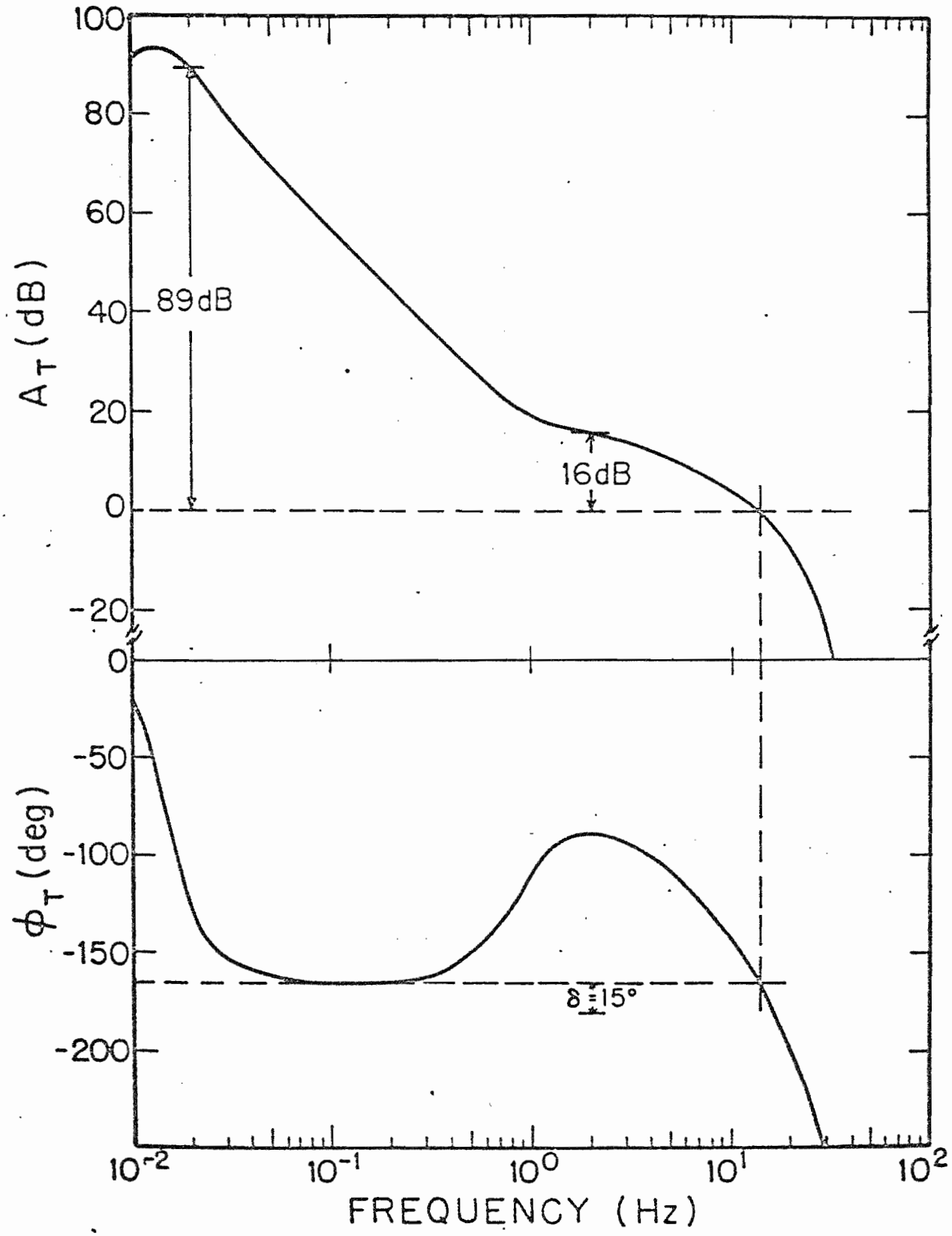
100
80
60
40
20
0
-20
A_T (dB)
89dB
16dB
0
-50
-100
-150
-200
ϕ_T (deg)
δ=15°
10^{-2}
10^{-1}
10^{0}
10^{1}
10^{2}
FREQUENCY (Hz)

Figure 3.6 A Bode plot for the triple loop system open loop energy response (A_E).

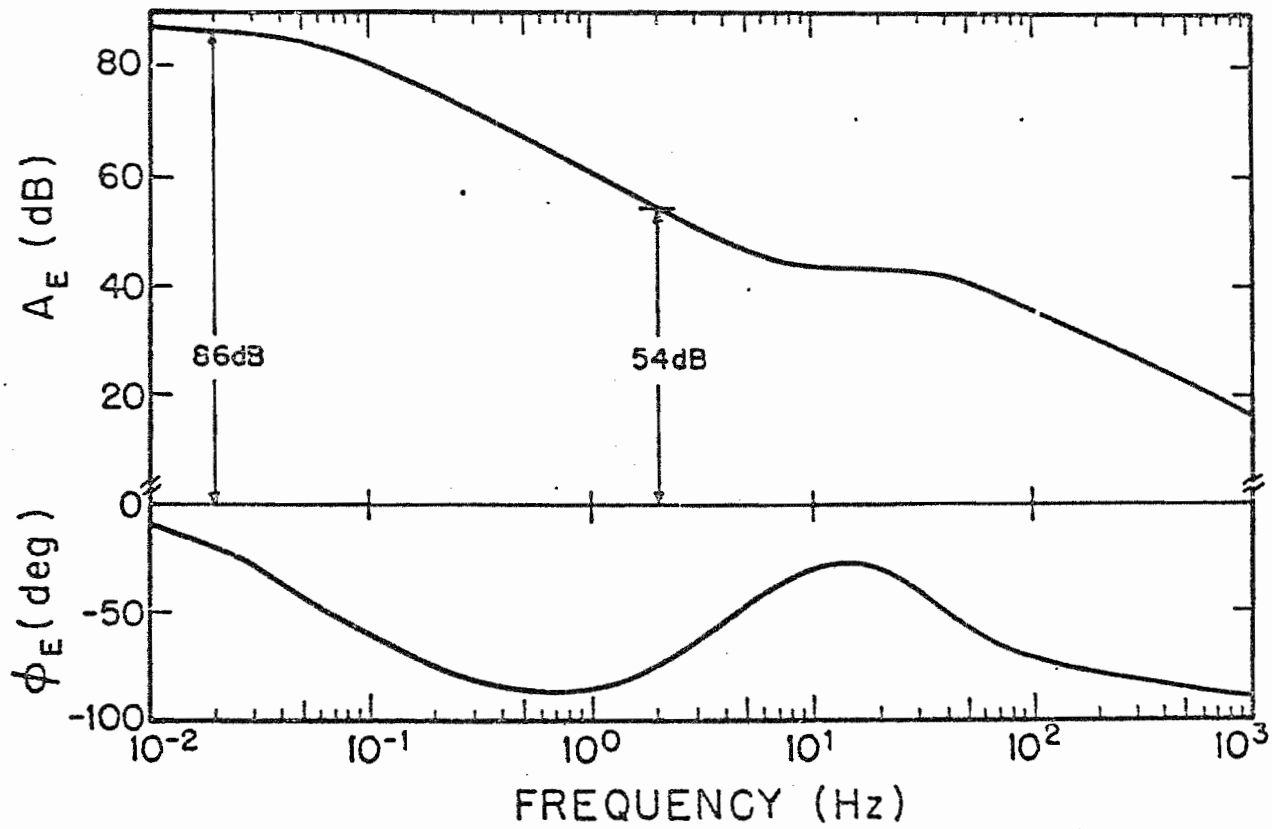
80
60
40
20
0
A_E (dB)
86dB
54dB
ϕ_E (deg)
-50
-100
10^{-2}
10^{-1}
10^{0}
10^{1}
10^{2}
10^{3}
FREQUENCY (Hz)

Figure 3.7 Oscilloscope traces showing terminal and energy fluctuations with and without fast feedback.

Terminal Ripple
1 kV/div

Control Slit
Error Signal
0.5 V/div

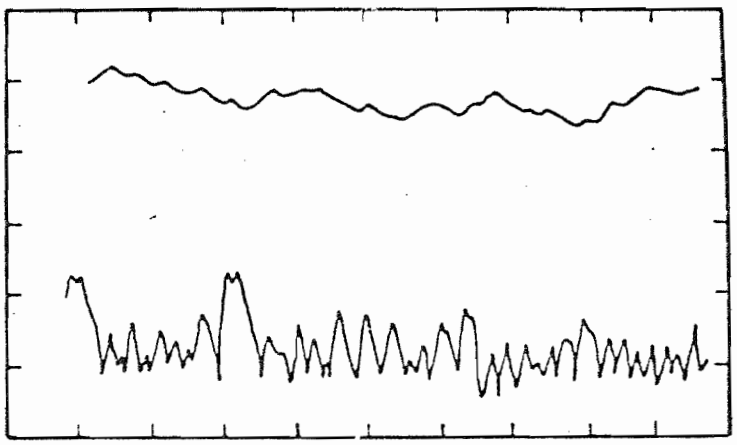

Time Base: 20 msec/div

FAST CHANNEL OFF

Terminal Ripple
1 kV/div

Control Slit
Error Signal
0.5 V/div

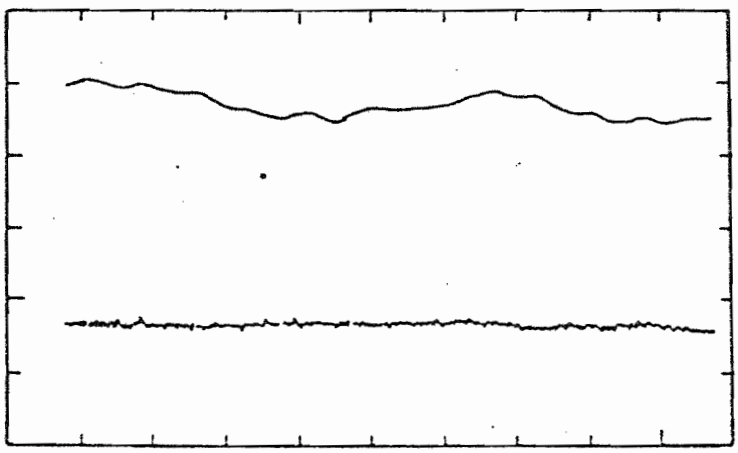

Time Base: 20 msec/div

FAST CHANNEL ON

terminal ripple are substantially reduced although the magnitude of the fluctuations is about the same as with no fast feedback. A precise calibration of the control slit error signal is difficult to obtain due to the logarithmic nature of the slit current preamps. However, experience has shown that a quantitative measurement of the beam energy spread is best made by measuring the cross section of a nuclear reaction in the vicinity of a narrow resonance. Figure 3.8 shows an f-wave resonance in the ^{54}Fe(p,p) reaction taken using the triple loop regulator. The full width at half maximum of the resolution function used to smear the theoretical cross section is 375 eV.

The various contributions to the total instrumental resolution may be estimated as follows. The spread in energy due to straggling in the stripper gas and target are expected to be greater than or equal to the average energy loss suffered by the beam in transit through them. For an ^{54}Fe target whose thickness is 3 μg/cm^2 this amounts to 150 eV. The energy loss in the stripper is more difficult to estimate since the oxygen pressure within the stripper canal cannot be directly measured. Assuming a canal pressure of one micron gives an energy loss of 275 eV. Standard duoplasmatrons such as the one in the TUNL direct extraction negative ion source produce beams with an energy spread of about 50 eV. Finally, the target Doppler broadening, which arises from the thermal motion of the atoms in the target,

Figure 3.8 A narrow resonance in the $^{54}Fe(p,p)$ reaction measured as a resolution check for the three loop energy stabilization system.

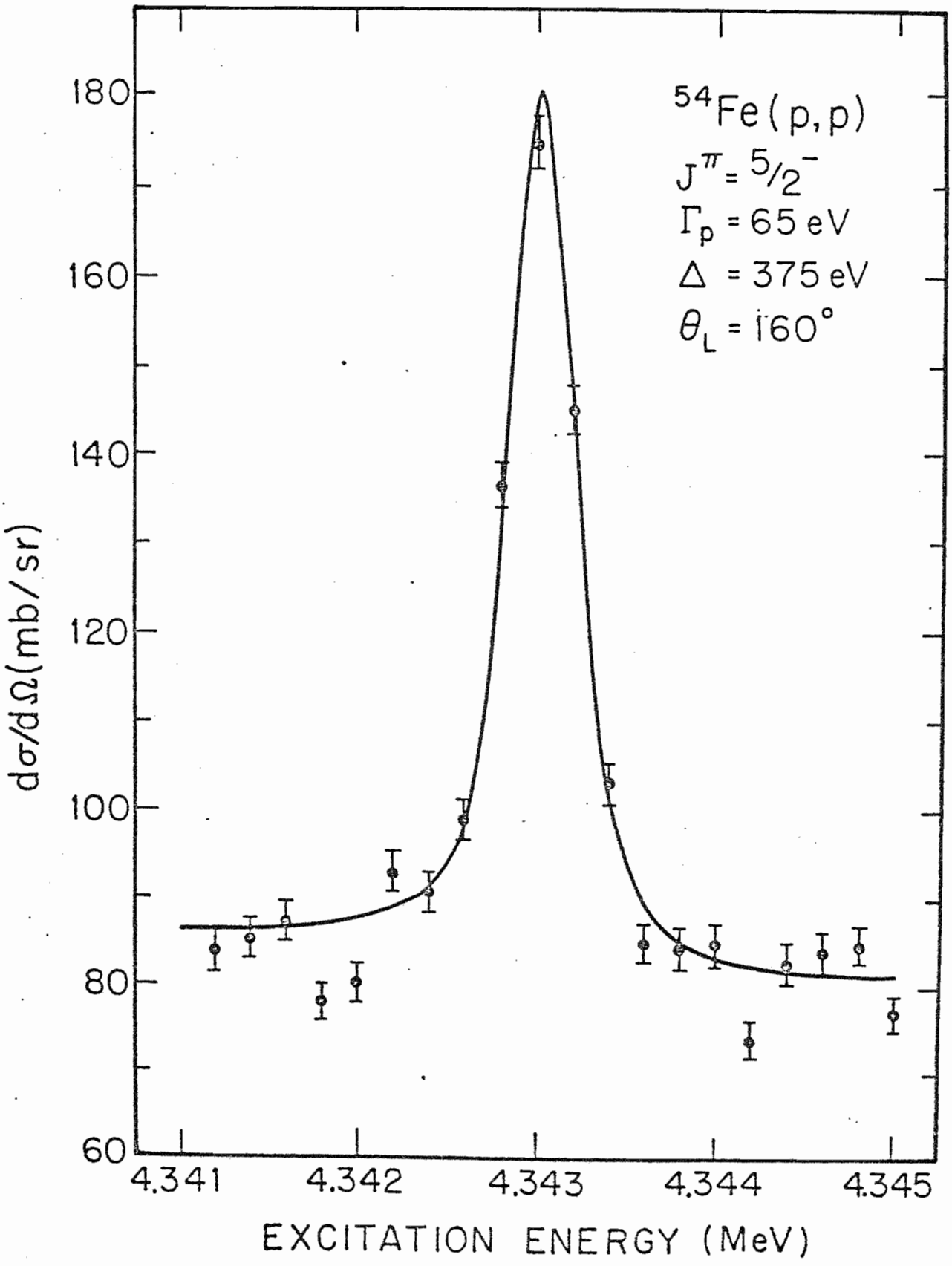
$^{54}Fe(p,p)$
$J^{\pi} = 5/2^-$
$\Gamma_p = 65$ eV
$\Delta = 375$ eV
$\theta_L = 160°$
180
160
140
120
100
80
60
$d\sigma/d\Omega$(mb/sr)
4.341
4.342
4.343
4.344
4.345
EXCITATION ENERGY (MeV)

may be estimated using the formula

$$\Delta E_o = 3.33 \left[M m E_R k T_{eq} / (M+m) \right]^{1/2} \qquad (3.1.15)$$

due to Bethe and Placzek (1937). Choosing T_{eq} =500°, ΔE_o is estimated to be 190 eV. The independent contributions to the energy spread add in quadrature and leave less than 100 eV that is attributable to residual time dependent beam energy fluctuations.

The design and construction details of the various system components are not required for a basic understanding of the system operating principles. In the interest of completeness, these details are included in Appendix II. Circuit diagrams and important features are discussed for the terminal amplifier installation, the LED driver, and the slit current preamplifiers.

3.2 Analyzing Magnet Stepping and Stabilization

In addition to a highly monoenergetic beam, proton elastic scattering experiments require the proton energy to be incremented very precisely. Normally, energy steps from 1/4 to 1/8 the resolution width are used. The exact step size is determined by many factors including the spin-parity of the observed resonances, the density of levels, and the observed resonance widths. The necessity for such precision is illustrated by figure 3.8. Here the energy stepsize is

160 eV, somewhat less than half the smear function width of 375 eV. The accuracy of the extracted resonance parameters depends on the details of the resonance lineshape as revealed by the data. Fortunately in this case, a data point has been taken very near the peak cross section. If the energy scale is displaced 80 eV one way or the other, the maximum in the cross section is missed entirely and the data may be fitted with a resonance width and resolution function quite different from those shown.

The precision with which the beam energy may be incremented depends on the precision with which the magnetic field in the analyzing magnet can be stepped and upon the low frequency feedback of the energy regulating system. The position r of the beam at the image slits of the analyzing system ideally will be a function only of beam energy and magnetic field.

$$r = f(E, B) \tag{3.2.1}$$

Therefore, any change in r can be written

$$\begin{aligned} \Delta r &= \frac{\partial f}{\partial E}\Delta E + \frac{\partial f}{\partial B}\Delta B \\ &= G_1 \Delta E + G_2 \Delta B \end{aligned} \tag{3.2.2}$$

This may be incorporated into the control system model as shown in figure 3.9. The loop equations are modified as follows.

Figure 3.9 The frequency domain model of the three loop system including the effect of a change in the analyzing magnet field strength ΔB.

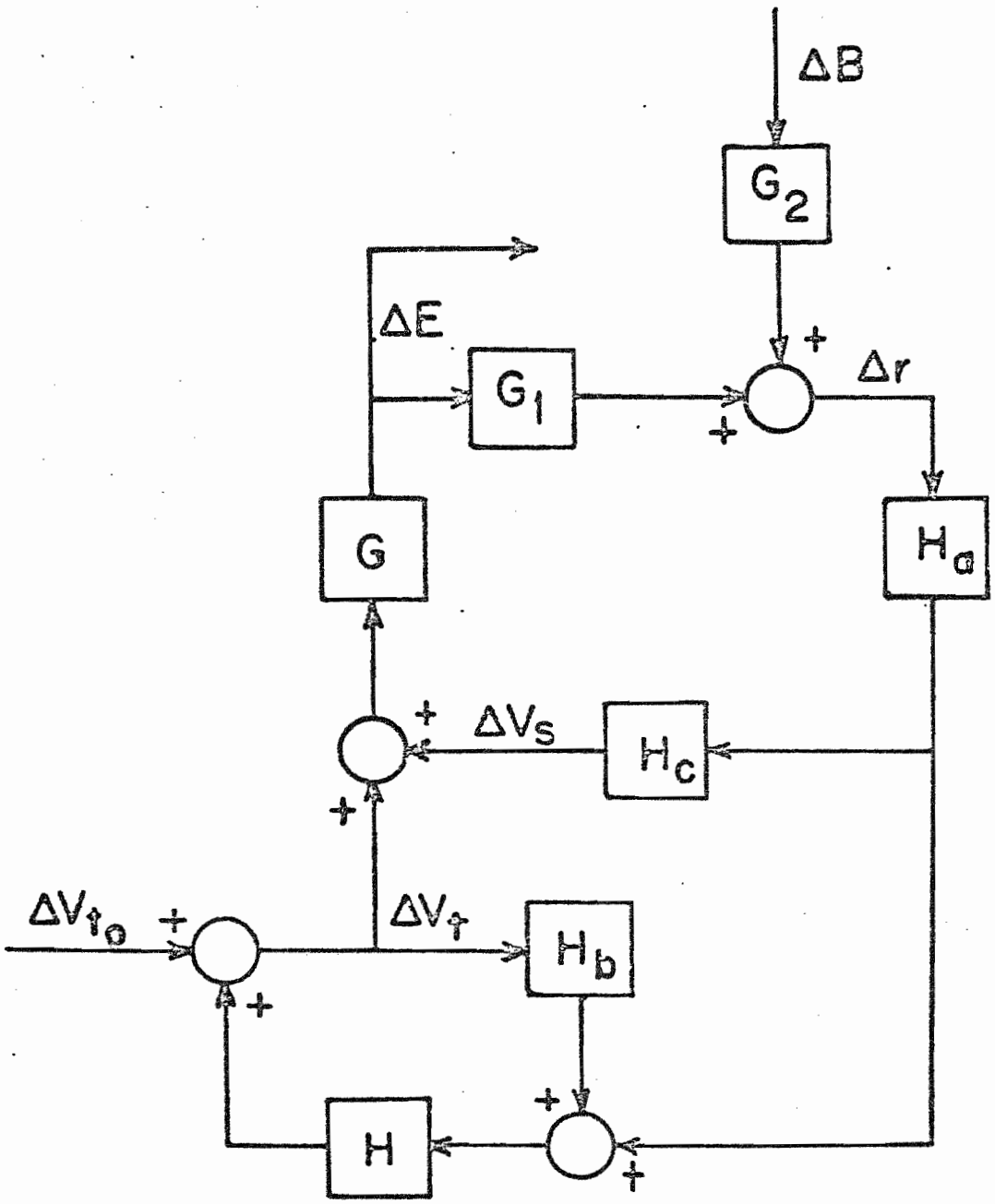
ΔB
G2
ΔE
G1
+
+
Δr
G
Ha
+
ΔVs
Hc
+
ΔVto
+
ΔVt
Hb
+
+
H

$$\Delta E = G\left[\Delta V_t + H_a H_c \left(G_1 \Delta E + G_2 \Delta B\right)\right] \qquad (3.2.3)$$

$$\Delta V_t = \Delta V_{t_0} + H\left[H_b \Delta V_t + H_a \left(G_1 \Delta E + G_2 \Delta B\right)\right] \qquad (3.2.4)$$

These equations may be solved as before for E to obtain

$$\Delta E = G \Delta V_{t_0} \left[\frac{1}{1 + A_E}\right] + G G_2 H_a \Delta B \left[\frac{H + (1 - H H_b) H_c}{1 + A_E}\right] \qquad (3.2.5)$$

There is an additional term proportional to ΔB. For very low frequencies, H_b and H_c go to zero and therefore for dc shifts in the field strength B, the additional term becomes

$$-\Delta B \frac{G_2}{G_1}\left[\frac{A_c}{1 + A_c}\right] \qquad (3.2.6)$$

where

$$A_c = -G G_1 H H_a \qquad (3.2.7)$$

A_c is the open locp response of the slit control channel of the corona loop. Since A_c exceeds 80 dB at very low frequencies, it is a good approximation to rewrite (3.2.5) as

$$-\Delta B \frac{G_2}{G_1} \qquad (3.2.8)$$

The minus sign appears because the Δr associated with an

increase in magnetic field is in the opposite direction from that associated with an increase in energy. G_1 and G_2 are constants which depend on the optical geometry of the analyzing magnet system. The energy steps are thus strictly proportional to the field increments.

The data of figure 3.8 were taken with the magnet current control system shown in figure 3.10. The heart of the system is the voltage programmable analyzing magnet power supply. Six volts applied at the programming input drives 270 amperes through the magnet load. The programming voltage is provided by a Zener diode and is scaled by two sets of control potentiometers. The first set drives the master proportionality controller which also provides the reference voltage for the analyzing system quadrupoles and sextupoles, as well as the 70-70 switching magnet which must track the analyzing system to keep beam on target. Current regulation is obtained by deriving a feedback signal from a temperature compensated sense resistor in series with the load. This signal is summed with the reference voltage and applied to the programming input. The energy of the proton beam is selected by manually adjusting the magnet current and thus the field strength.

For this data, each energy step of 160 eV corresponded to a seven degree rotation of the fine current adjust potentiometer which drives the master proportionality controller. Smaller energy steps could not be taken by

Figure 3.10 The analyzing magnet power supply before modification.

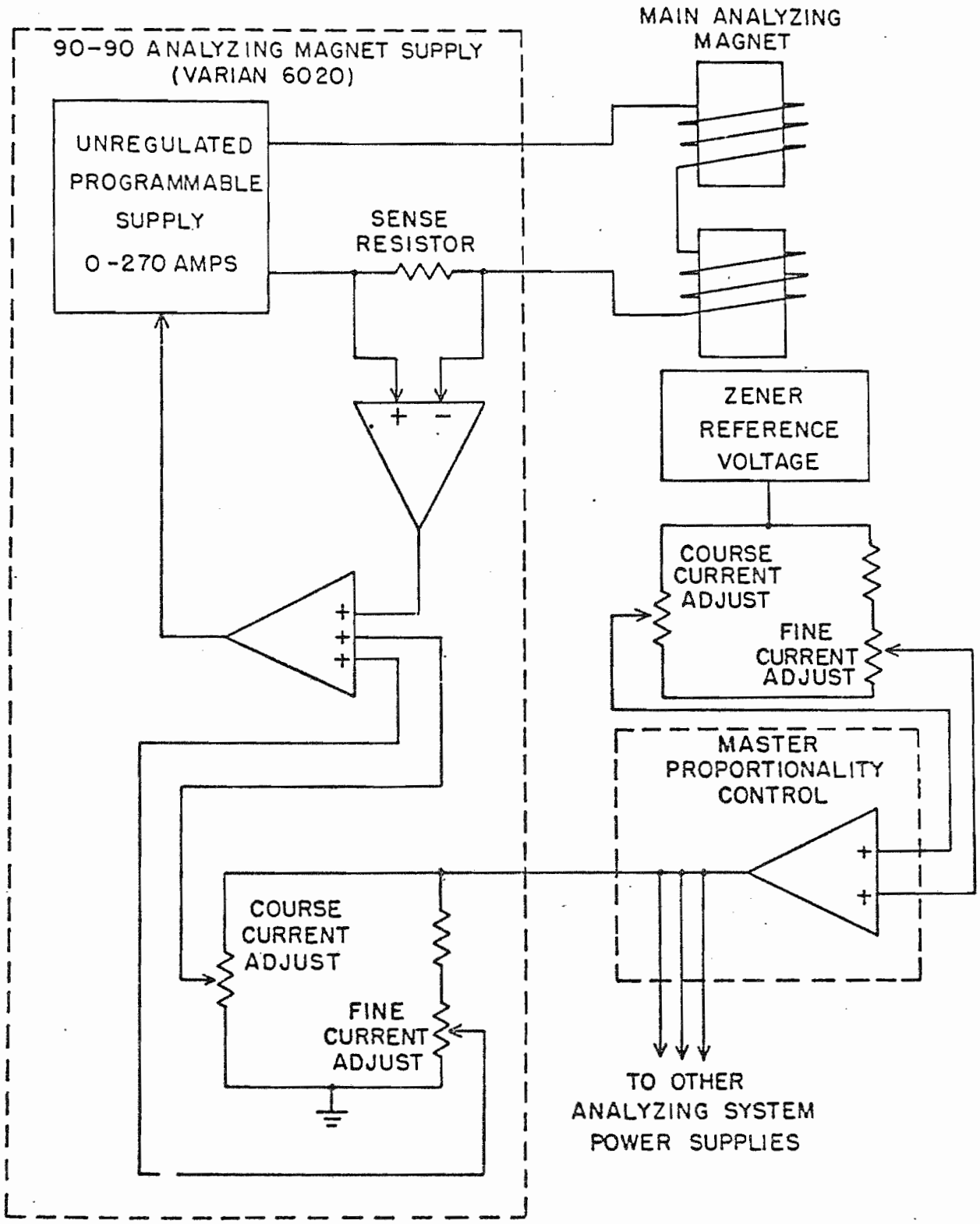

ANALYZING MAGNET POWER SUPPLY

manually adjusting the current control. This problem was solved by driving the fine current control with a stepping motor via a 400:1 reduction gear train. The motor is digitally commanded by the data taking computer. This system allows extremely precise adjustment of the reference voltage. It also eliminates many errors associated with manual operation by the experimenters.

During the initial stages of the $^{90}Zr(p,p)$ experiment, large discrepancies in the spacing of resonances appeared in overlapping sections of data. The cause was traced to slow drifts in the magnet current. These drifts amounted to a milliamp or more out of 60 amperes with periods ranging from several minutes to half an hour. Presumably they are caused by temperature instability in the impedance of the sense resistor and the Zener diode. However, these current variations were only slightly greater than the power supply manufacturer's specifications. Fortunately, compensation for these current fluctuations is possible through direct field regulation of the magnet supplies. This is accomplished by sampling the magnetic field with a nuclear magnetic resonance fluxmeter. This device provides an error signal proportional to the field fluctuations $\Delta B = B - B_0$, where B_0 is the field strength associated with nuclear magnetic resonance at a radio frequency ν_0. These quantities are related by

$$h\nu_0 = 2\mu B_0 \qquad (3.2.9)$$

where h is Planck's constant and μ is the nuclear magnetic moment of the probe sample material. The NMR signal is summed with the other components of the programming voltage in the master proportionality controller. Drifts in the field due to faulty current regulation are corrected by this feedback. Typically, the system is used to stabilize the beam energy at one point over a long time period. In this case the problem requires stabilization at each of a succession of different energies. Each time the field is incremented by ΔE, the NMR reference frequency must be changed by $\Delta\nu$ where

$$\Delta\nu = \frac{2\mu\Delta B}{h} \qquad (3.2.10)$$

The accuracy and precision of the field increment thus depends upon the quality of the oscillator which drives the NMR probe. Fortunately, extremely accurate digitally synthesized oscillators are available. A John Fluke model 6039A frequency synthesizer was obtained as an external oscillator for the TUNL NMR fluxmeter. When driven by a General Radio 5MHz frequency standard, the RF output is adjustable in frequency from 1 Hz to 40 MHz in single Hz steps. The frequency stability is approximately one part in 10^8. In addition, it is digitally programmable. Computer interface hardware and software have been developed which allows the data taking computer to increment the reference frequency and therefore the machine energy automatically.

The complete analyzing magnet control system is shown in figure 3.11. Since the installation of this system, energy drifts and data reproducability have ceased to be a problem.

3.3 Targets

The targets for this experiment consist of metallic ^{90}Zr evaporated onto 5 $\mu g/cm^2$ self-supporting carbon films. The isotopic enrichment exceeds 98%. Target thickness varied between 2 and 4 $\mu g/cm^2$.

The Zr metal was evaporated from a 0.010" thick tungsten boat through which is passed a large electric current. The metal melts at about 230 amperes (1850° F) and evaporates smoothly at 300 amperes. Care must be taken to thoroughly outgas the boat before it is loaded with isotope. Otherwise the metal oxidizes immediately after melting and recrystallizes. The evaporation of ZrO is impossible with the open boat method since the melting point of the oxide is approximately 2950° F. As is illustrated in figure 3.12, target contamination was not a problem. A typical detector spectrum shows nitrogen, oxygen, and silicon peaks. The carbon peak has been gated out as discussed in the next section. The small amount of nitrogen is due to surface adsorption during exposure to the atmosphere, while oil vapor from the evaporator diffusion pump is the source of the silicon. The oxygen is a result of natural target

Figure 3.11 The analyzing magnet power supply after modification.

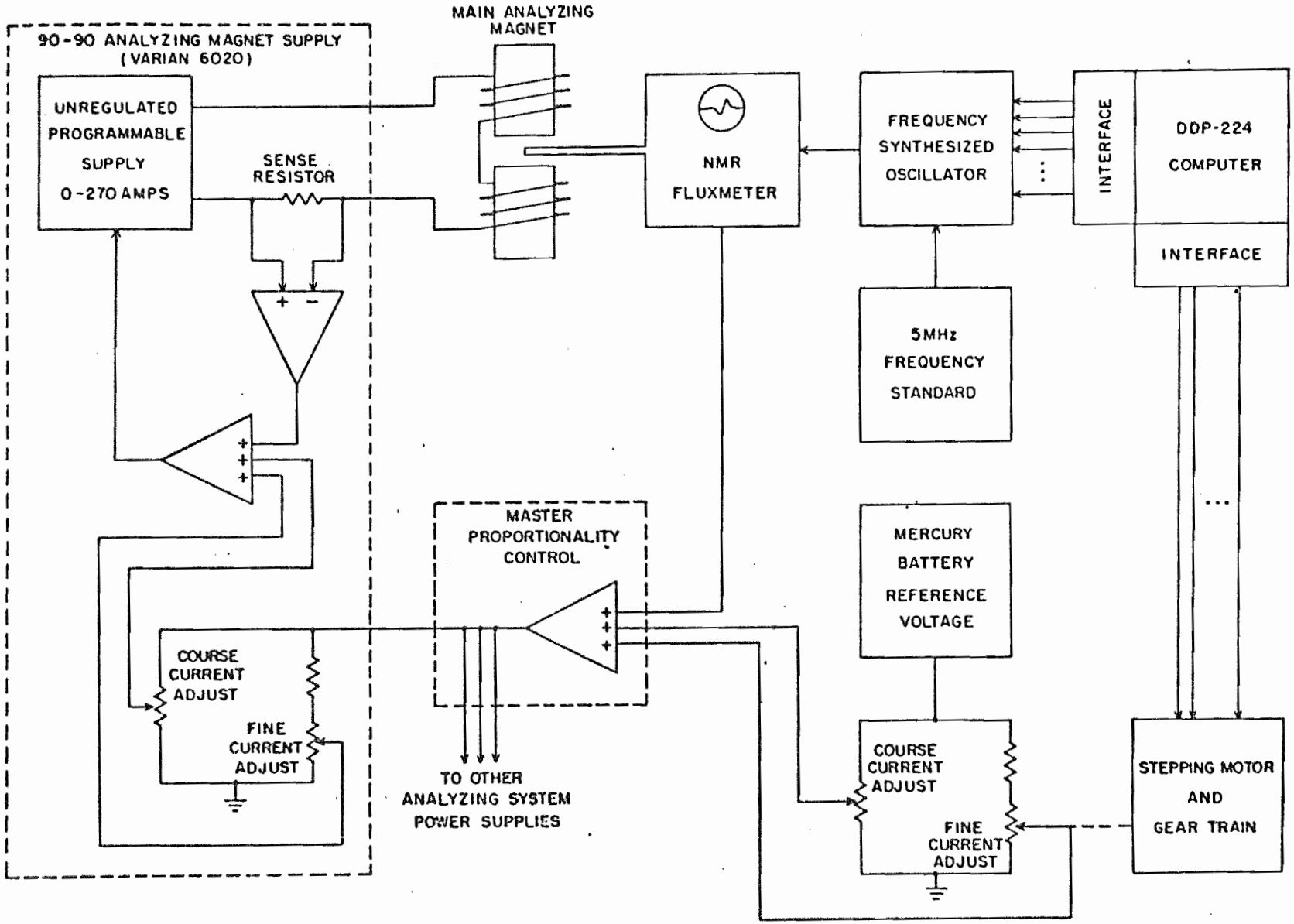

ANALYZING MAGNET POWER SUPPLY

Figure 3.12 A typical detector spectrum. The insert shows, on an expanded scale, the effect of gating out the Carbon pulses before the multi-channel analysis.

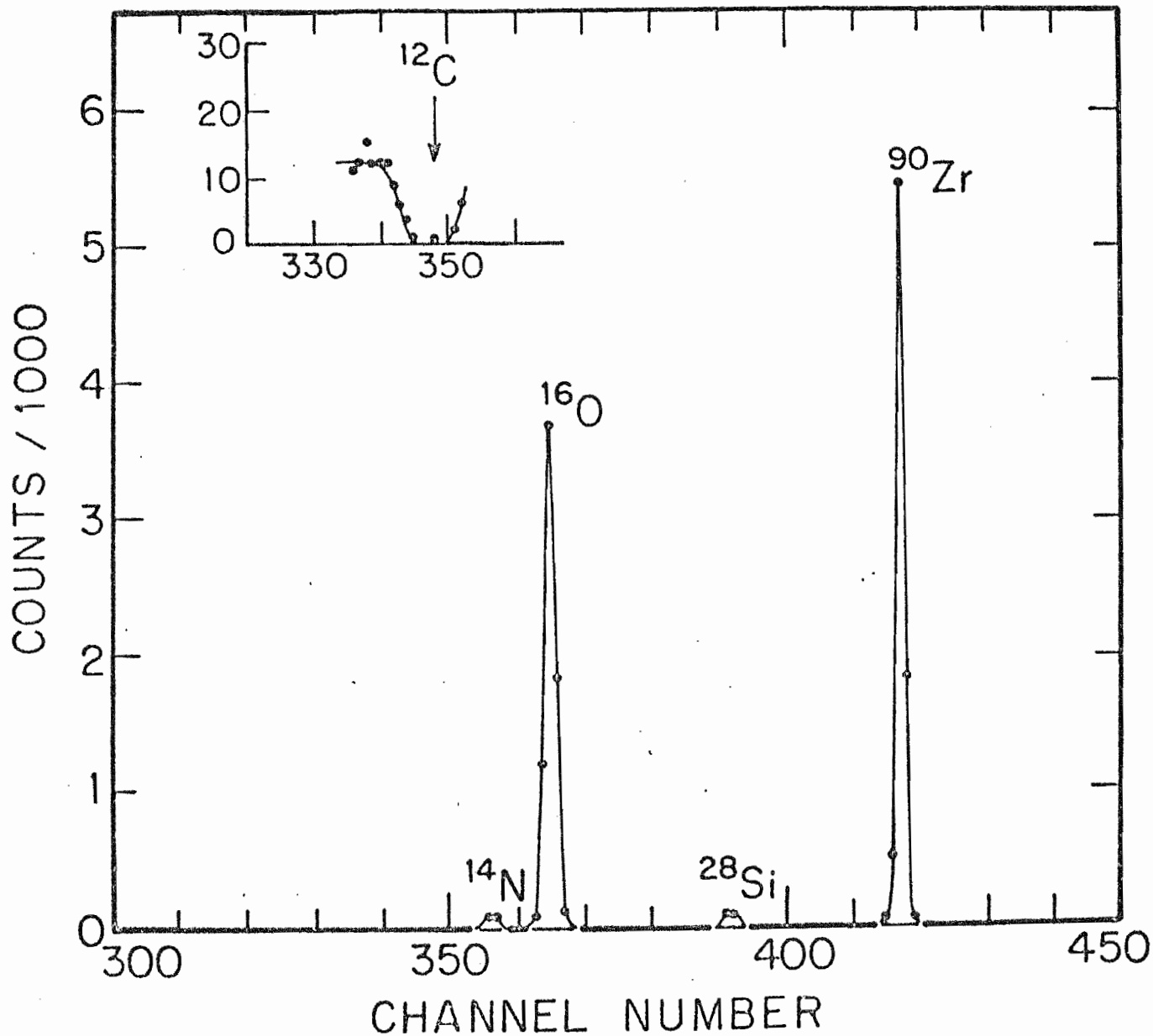
30
20
10
0
330
350
12C
90Zr
16O
14N
28Si
6
5
4
3
2
1
0
300
350
400
450
COUNTS / 1000
CHANNEL NUMBER

oxidation and may be minimized by storing the targets in an evacuated dessicator.

3.4 Scattering Chamber and Pulse Instrumentation

The scattering chamber used for this experiment is located on the 60° left port of the TUNL 70-70 switching magnet. A top view of the chamber (with the lid removed) is shown in figure 3.13. It is constructed of aluminum and has an inside diameter of 23.5". A turbo-mechanical pump maintains a vacuum of 2×10^{-6} torr within the chamber. Beam definition was accomplished with a 0.125" diameter collimator in the box ahead of the chamber and a pair of crossed 0.080" slit apertures located at the end of a telescoping snout inside the chamber. These were placed approximately four inches from the target. The scattered protons were counted with silicon surface barrier detectors whose properties are summarized in table 3.1. For each detector, a pair of tantalum collimators fitted to the ends of an aluminum snout defined the detector solid angle. The integrated beam current is collected in a faraday cup located behind the chamber. Coaxial cables connect each detector to its preamplifier via a vacuum feedthrough located in the floor of the scattering chamber.

The preamplifiers (Ortec 109A) were located at the target chamber. They drive highly stable spectroscopy

Figure 3.13 A top view of the scattering chamber showing the detector geometry.

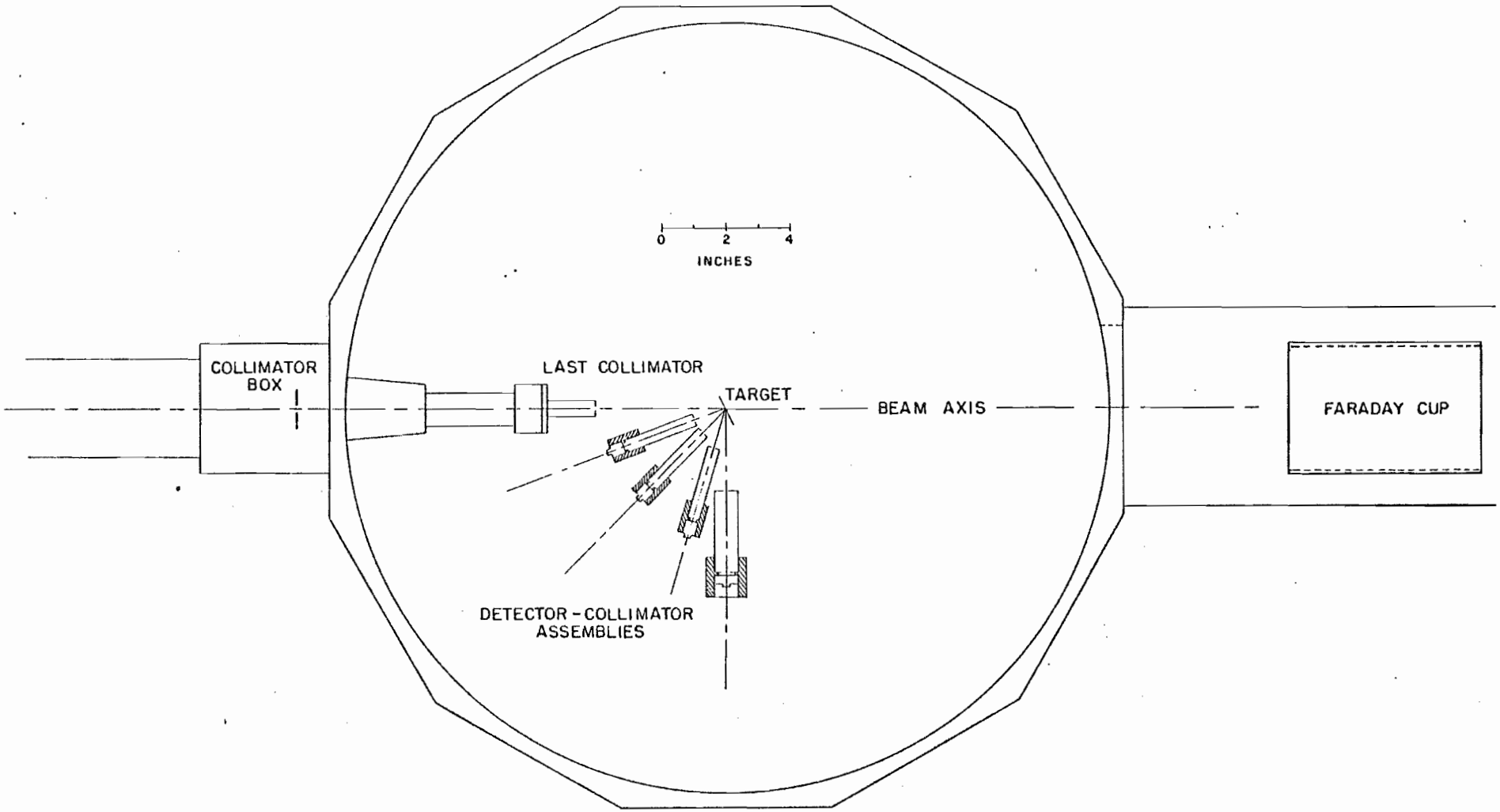
0
2
4
INCHES
COLLIMATOR BOX
LAST COLLIMATOR
TARGET
BEAM AXIS
FARADAY CUP
DETECTOR - COLLIMATOR ASSEMBLIES

TABLE 3.1

DETECTOR ANGLE	90°	107°	135°	160°
ACTIVE AREA (mm^2)	100	25	50	50
BAIS VOLTAGE (VOLTS)	160	275	135	135
RESOLUTION (keV)	40	25	28	30
SOLID ANGLE (msr)	2.34	3.92	4.58	4.58

amplifiers (Ortec 452) through long cables which link the target and control rooms. The bipolar output of each amplifier feeds a pair of timing single channel analyzers (Ortec 420A), labeled 'A' and 'B' in figure 3.14. SCA 'A' is run in the integral mode so that a signal of any size gives rise to a gate output pulse. SCA 'B' is run in the differential mode with a window set on the pulses which correspond to protons scattered from the carbon substrate. The gate pulses from the SCAs go to a coincidence module (Ortec 481) whose output has the signature $A \cdot \overline{B}$. This signal drives the gate input of a linear gate and stretcher (Ortec 442) whose linear input is driven by the unipolar output of the spectroscopy amplifier. In this manner, carbon pulses are preferentially excluded in order to reduce dead time in the multi-channel analysis. The insert in figure 3.12 illustrates the result. Here the vertical scale has been divided by a factor of 50. A pronounced hole in the background occurs where the carbon peak should be located. The four coincidence gate signals also serve as routing signals. The gated linear signals from all four angles are summed. The result is then fed to an analogue to digital converter (Northern Scientific NS-628) whose output is sorted by the router into four 512 channel spectra and stored in the computer.

Figure 3.14 A schematic diagram of the signal processing electronics.

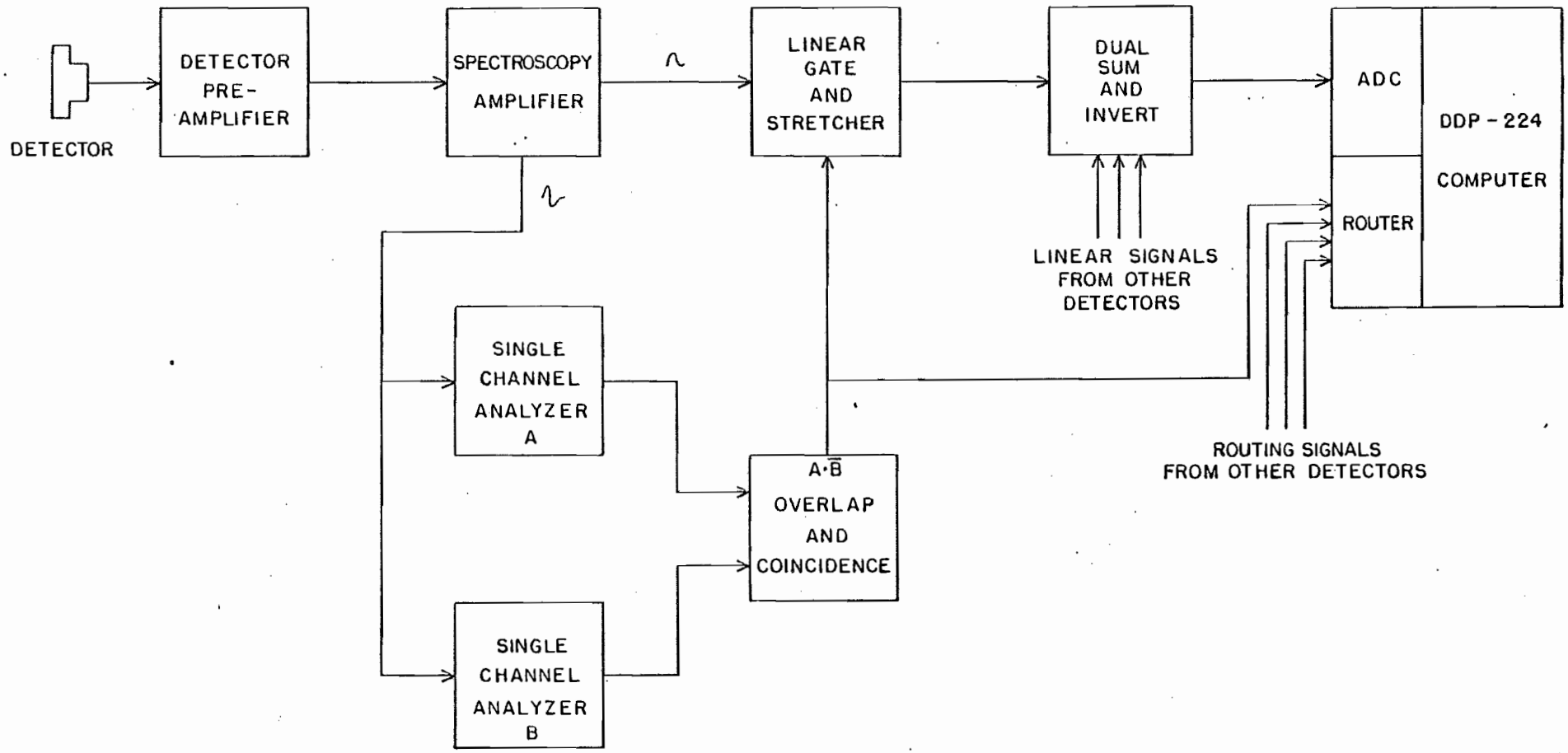
DETECTOR
DETECTOR PRE-AMPLIFIER
SPECTROSCOPY AMPLIFIER
LINEAR GATE AND STRETCHER
DUAL SUM AND INVERT
ADC
DDP - 224 COMPUTER
ROUTER
LINEAR SIGNALS FROM OTHER DETECTORS
SINGLE CHANNEL ANALYZER A
SINGLE CHANNEL ANALYZER B
A·B̄ OVERLAP AND COINCIDENCE
ROUTING SIGNALS FROM OTHER DETECTORS

3.5 Data Taking Procedures

The elastic scattering yield curves for this experiment were taken in overlapping sections which varied from 10 to 50 keV in length. Each point required an integrated charge of 120 μC. For the most part the data were taken in 80 eV steps which correspond to NMR frequency increments of 100 Hz. Double size steps were used for some of the data on the wings of the analogue state. The beam current on target varied between one and three μA. Thus the time per point varied between one and two minutes, which gives a data taking rate of three to five keV/hr.

At the end of each point, the preset scaler which counts the integrated beam current initiated a series of computer operations. The sequence was as follows,

1) Turn ADC and router off
2) Increment frequency synthesizer
3) Increment analyzing system voltage reference
4) Dump spectra on tape
5) Sum windows set on peak of interest
6) Store sums in yield curve display matrix
7) Clear spectra
8) Clear preset scaler
9) Turn ADC and router on

At this point data accumulation begins and the whole process

is repeated. Data taking was also interrupted if beam on target dropped below a certain minimum level. In this way, the mechanical aspects of data taking were completely automated.

This left the experimenter(s) free to monitor the online data displays. Both spectrum and yield curve displays were available for each angle. Preliminary offline data processing was begun on the DDP-224 α-computer as data tapes were completed. This consisted primarily of summing the Zr peak in the spectra for each energy. Each set of yields was punched on a computer card along with the corresponding energy, obtained from the NMR calibration. These cards comprise the input data to the R-matrix fitting program 'MULTI' discussed in Chapter 4.

Chapter 4

DATA AND RESULTS

4.1 Cross Section Fitting Procedure

The R-matrix computer program 'MULTI' written by Sellin (1969) was used to fit the elastic scattering data. This code calculates differential cross sections for up to 30 competing channels. In the present work, elastic scattering is assumed to be the only contributing nuclear reaction. No other charged particle channels are observed and all data were taken below the (p,n) threshhold. The (p,γ) channel, which is not treated by R-matrix theory, was ignored.

The analysis is begun by guessing a set of resonance parameters. For each resonance, a resonance energy, total angular momentum and parity J^{π}, and a laboratory width are input to the code along with the raw yield curve data. 'MULTI' calculates a differential cross section which includes the effects of Coulomb, hard sphere, and resonance scattering.

The calculated cross section is 'smeared' with a resolution function which reflects the time averaged spread in the incident proton energy. For this experiment, this function had a half Gaussian, half Lorentzian shape where the ratio of the half widths W_L/W_G =1.125. The Lorentzian shape is introduced to approximate the asymmetric energy distribution due to straggling in the stripper gas. The total width (FWHM) of the resolution function varied between 425 and 450 eV for most of the data.

The data is then normalized to the calculated cross section. Background subtraction, amounting to 3-4% of the total yield was used only for the 90° data. This correction was necessary because of the relatively poor detector resolution at that angle. The output of the program consists of the normalized data superimposed on a plot of the calculated cross section. The resonance parameters are varied until a satisfactory visual fit is obtained.

The data was fit in overlapping 10 to 20 keV sections, beginning near the center of the analogue, where the largest resonances occur. Resonance parameters for the particular section being fitted plus parameters for levels in adjacent data, up to the maximum number (75) allowed by the code, were included in the fit. As fitting progressed toward the wings of the analogue, consistent normalization of the data could not be obtained. This was the result of the exclusion of an increasingly greater part of the analogue strength

from the R-matrix cross section. The problem was solved by modifying 'MULTI' to accept up to 300 levels. Inclusion of all strong resonances changed the calculated cross section as much as 10 to 20% on the wings of the distribution and corrected the data normalization.

4.2 Cross Section Data and Fits

Data were taken between the laboratory proton energies of 5.684 and 5.992 MeV. The data and R-matrix fits are shown in their entirety in figure 4.1. The resonance parameters extracted from this analysis are listed in table I.1 (Appendix I). The energy calibration is provided by the NMR calibration of the analyzing magnets. This in turn was checked against the 12.713 MeV resonance in the $^{16}O(p,p)$ reaction and several narrow resonances previously measured by Flynn (1977) in the $^{54}Fe(p,p)$ reaction. These occur at proton energies between 3 and 4 MeV, and their resonance energies are tied to the $^{7}Li(p,n)$ threshhold. When the analyzing magnets have been cycled to eliminate hysteresis and the beam geometry is properly limited, the NMR calibration is accurate to ±5 keV. Particular care was taken to obtain a good calibration for the first set of data, which lies in the interval 5.865 to 5.892 MeV. All subsequent data sets were shifted in energy to agree with the initial calibration.

Figure 4.1 The normalized data and R-matrix cross section fits. The solid line is the fit. Data was fitted between 5.684 and 5.992 MeV.

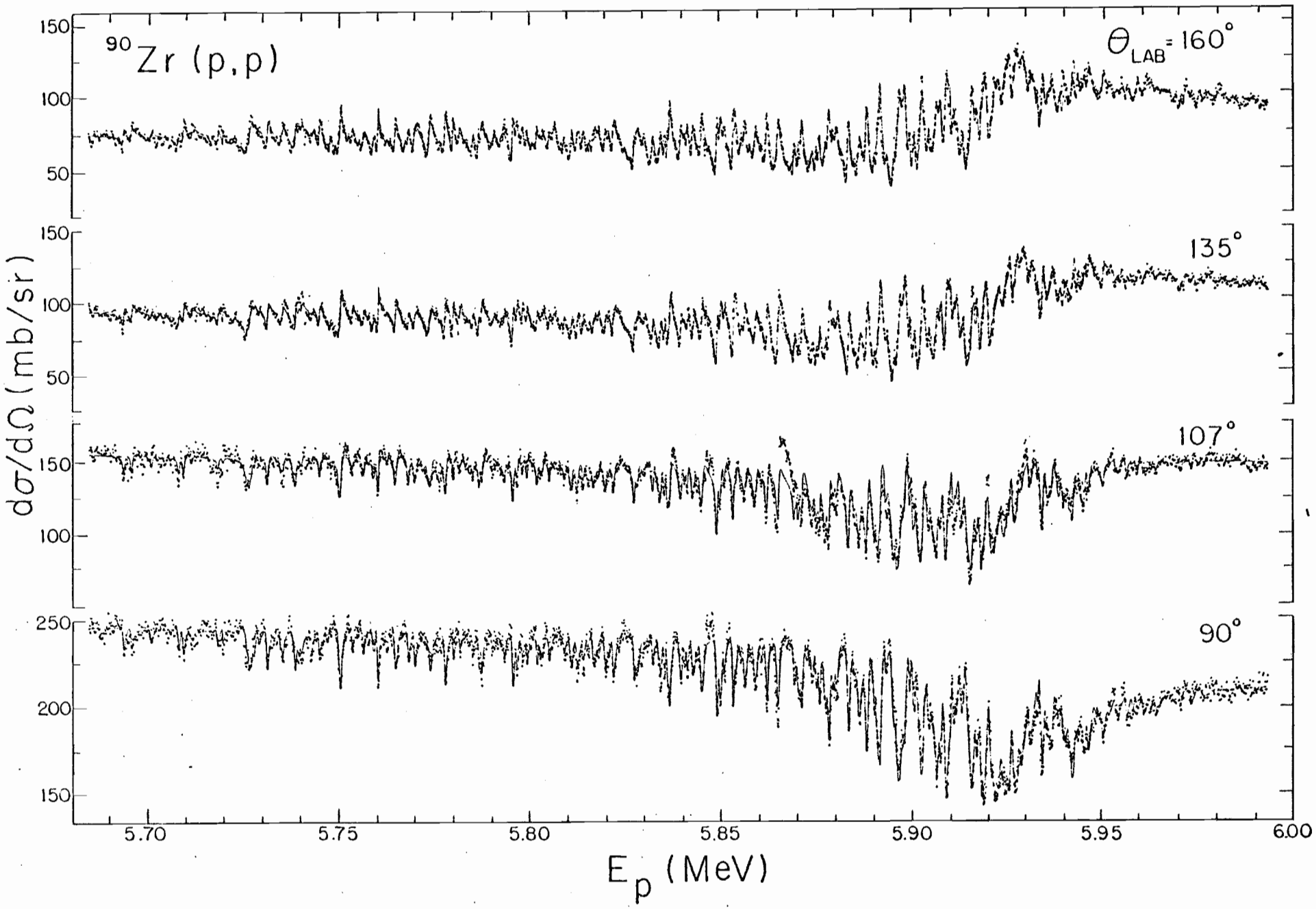
^{90}Zr (p,p)
θ_{LAB} = 160°
135°
107°
90°
dσ/dΩ (mb/sr)
150
100
50
250
200
5.70
5.75
5.80
5.85
5.90
5.95
6.00
E_p (MeV)

These data are dominated by the fine structure of the $1/2^+$ analogue state corresponding to the 1.21 MeV $1/2^+$ state in ^{91}Zr. The fit is comprised of 302 s-wave resonances. 18 p-wave ($J = 1/2^-$) are also included in the fit. However, in almost all cases these are either strongly interfering with other levels or have small laboratory widths. For this reason, most of these spin assignments are tentative and are listed in table I.1 as $(1/2^-)$.

As shown in figure 4.2, the density of observed levels increases markedly from the wings of the analogue to the center, where the average resonance spacing is on the order of 400 eV. This may be compared with an average spacing of 150 eV predicted by the Gilbert and Cameron semi-empirical formula (1965).

In this region, the average laboratory width is around 125 eV. The degree of level interference is so great in certain sections of the data that the individual resonance lineshapes disappear completely. Data of this type are shown in figure 4.3. The fit to this data contains 25 s-wave resonances between the proton energies of 5.92 and 5.93 MeV. Clearly, the fine structure in regions such as this is not totally resolved. However, the agreement between data and fit at all angles insures that the strength is distributed approximately as indicated by the resonance parameters. The fit parameters for this type of data are enclosed in parentheses in table I.1.

Figure 4.2 The apparent $1/2^+$ level density as a function of excitation energy. The averaging interval is 10 keV.

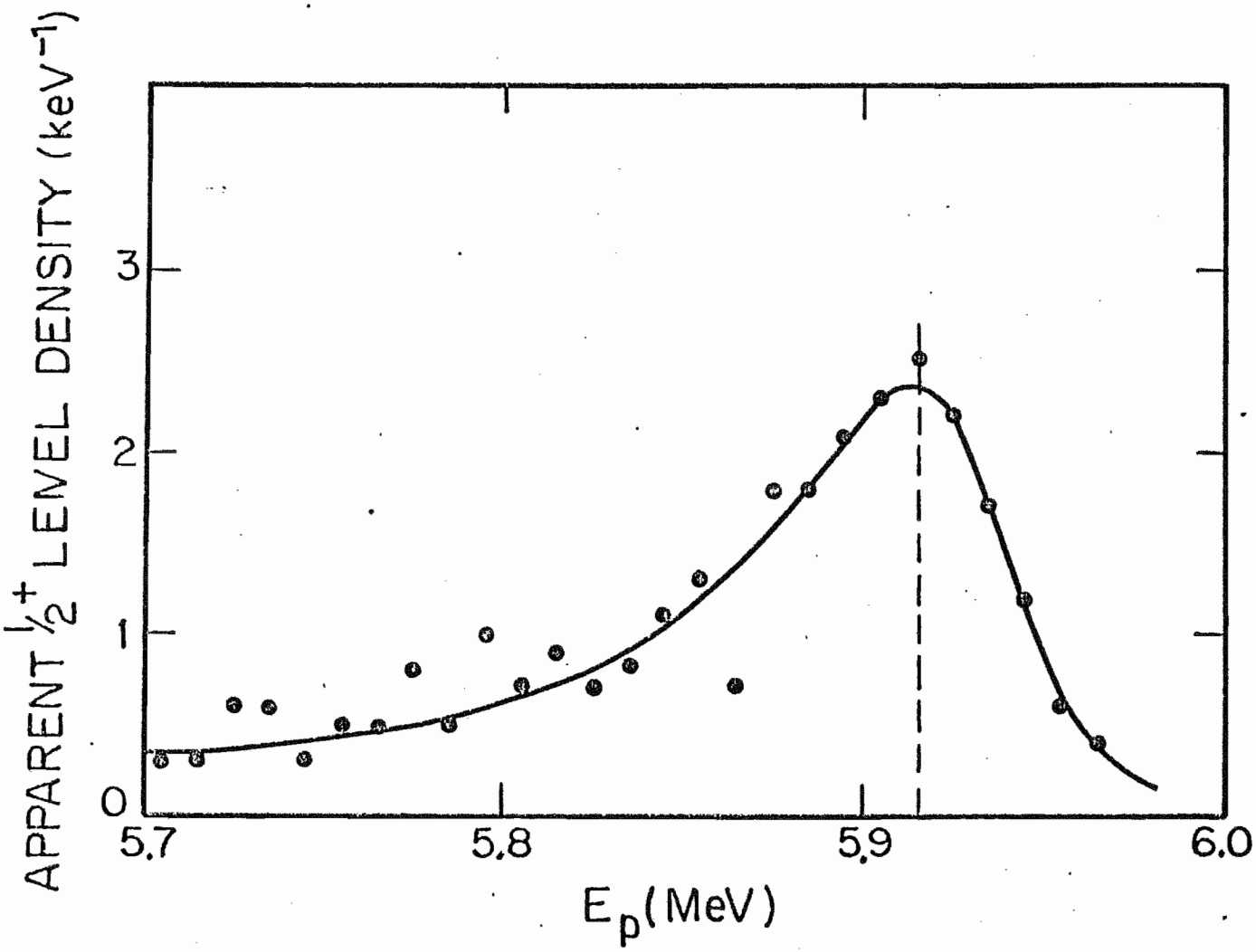
APPARENT $\frac{1}{2}^+$ LEVEL DENSITY (keV^{-1})
0
1
2
3
5.7
5.8
5.9
6.0
E_p(MeV)

Figure 4.3 The normalized data and fits in the interval 5.91 to 5.94 MeV. The fit contains 25 $1/2^+$ resonances between 5.92 and 5.93 MeV.

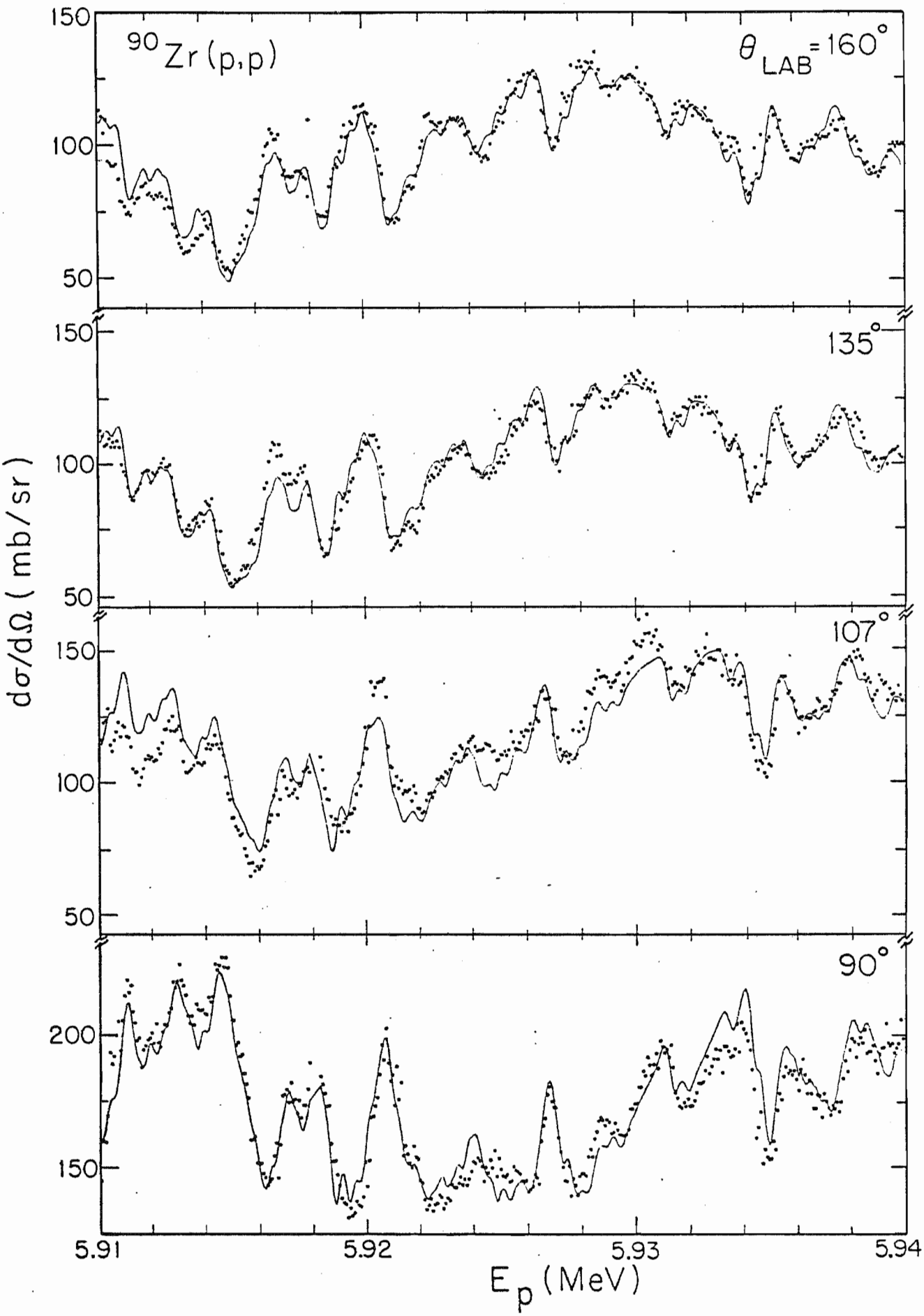
^{90}Zr (p,p)
θ_{LAB}=160°
135°
107°
90°
150
100
50
200
dσ/dΩ (mb/sr)
5.91
5.92
5.93
5.94
E_p (MeV)

Several small anomalies are present in the data. Near 5.85 MeV, the 90° non-resonant fit considerably undershoots the data. This is the result of excessive background subtraction for one section of the data. The same thing occurs in the 107° data at about 5.865 MeV. At this angle, there was no background subtraction and the difficulty is attributed to beam motion on the target. In both cases the fit is sufficiently good at the other angles that these problems were overlooked. The only data which could not be satisfactorily fit lies between 5.938 and 5.942 MeV. However the total fitted s-wave strength in this region amounts to less than 0.5 keV, or about 2% of the total analogue strength obtained from the fine structure fits (section 4.4). This is small compared to the error associated with the analogue reduced width γ_A^2, and thus does not affect the remainder of the analysis.

4.3 Fine Structure Fitting Procedure

In order to avoid errors introduced by averaging the reduced widths to obtain an energy dependent strength function, the integral of equation (2.5.19) is fit to the running sum of the experimentally determined reduced widths. This procedure was introduced by Lane, Lynn, and Moses (1974) and amounts to varying the parameters W_o, γ_A^2, Δ, s_o, and E_A to obtain the best least squares fit. The parameters

are assumed constant over the energy interval of the fit.

An initial set of fine structure parameters is guessed by inspection of the data and then parameter space is searched to obtain a good fit. Best fit values for Δ and s_o are then obtained by fitting only the wings of the distribution while searching on these variables and holding the others fixed. The entire ensemble of levels is then refit holding Δ and s_o fixed but allowing the other parameters to vary.

4.4 Fine Structure Data and Fits

Figure 4.4 shows the differential and integral plots of the reduced width fine structure. The general features of the analogue are evident in the differential plot. The width distribution is clearly asymmetric. Observable analogue fragments exist as far as 230 keV below the analogue energy but disappear less than 100 keV above. Although the average level spacing <D> is much smaller than the spreading width W_o, the analogue is not completely dissolved in the background. There are 10-15 strong levels near the center of the distribution that contain a considerable fraction of the analogue strength. It would seem that the mixing is of intermediate strength and occurs mostly in the external region.

Figure 4.4 The fine structure distribution in the differential (lower) and integral (upper) representations. The solid line is the integral of the Lane strength function.

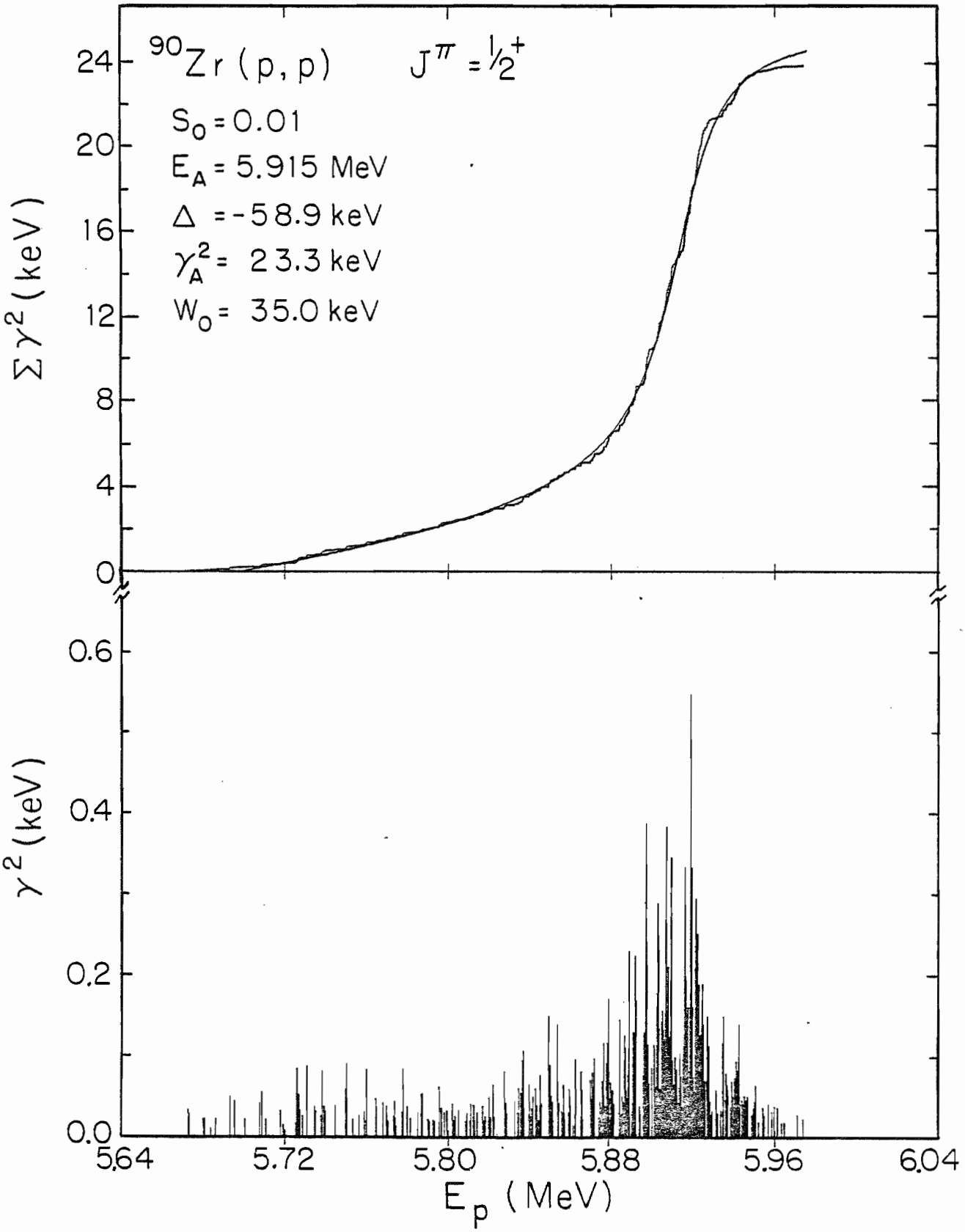
^{90}Zr (p, p)
$J^\pi = 1/2^+$
$S_0 = 0.01$
$E_A = 5.915$ MeV
$\Delta = -58.9$ keV
$\gamma_A^2 = 23.3$ keV
$W_0 = 35.0$ keV
$\Sigma\gamma^2$ (keV)
γ^2 (keV)
E_p (MeV)
0
4
8
12
16
20
24
0.0
0.2
0.4
0.6
5.64
5.72
5.80
5.88
5.96
6.04

Superimposed on the plot of cumulative reduced width is the integral of equation (2.5.19) which is obtained from the following set of fine structure parameters.

$$s_o = 0.01 \pm 0.003$$

$$E_A = 5.915 \pm 0.005 \text{ MeV}$$

$$\Delta = -58.9 \pm 20 \text{ keV}$$

$$W_o = 35.0 \pm 7 \text{ keV}$$

$$\gamma_A^2 = 23.3 \pm 5 \text{ keV}$$

The errors reflect the sensitivity of the fit quality to variations in the fine structure parameters. The overall quality of fit is quite good except at the extreme high and low ends of the distribution. A better fit may be obtained in these areas by allowing a smaller background strength function. In fact the fit with χ^2 minimized gives $\Delta = -214$ keV and $s_o = 0.004$. However this is in sharp disagreement with the $1/2^+$ background strength function for ^{93}Tc measured by Outlaw (1974). A value of 0.04 was obtained from this experiment at a proton energy of 5.3 MeV. In ^{93}Tc the level density is substantially less than that observed in the present work and as a result, the cross section data on the wings of the analogue are considerably better. In ^{91}Nb, the average laboratory width is small compared to the smallest resonance width observable experimentally. Based on a level density comparable to that observed near the center of the

analogue state, $\rho = 2.5$ keV^{-1}, $s_o = 0.01$, and a minimum observable laboratory width of 15 eV, integration of the Porter-Thomas distribution indicates that the experiment sees only about 10% of the background levels, and thus about 45% of the background strength. Therefore the best fit to the background data considerably underestimates the background strength function.

From equation (2.5.19) ω is found to be 198 keV. Taking

$$\Gamma_\lambda^\uparrow = 2P\gamma_A^2 = 23.8 \text{ keV}$$
$$\Gamma_\lambda^\downarrow = W_o = 35 \text{ keV} \quad \text{(equation (2.5.17))}$$
$$\langle D \rangle = 0.4 \text{ keV}$$

a value of the mixing parameter λ may be obtained

$$\lambda = 0.94$$

We obtain $\omega^2/(4\Delta^2) = 0.71$ and thus the asymmetry parameters assume the values $r = 0.59$ and $R = 6.75$. The subjective impressions of intermediate mixing primarily in the external region are confirmed by the fit to the fine structure.

Several of the fine structure parameters may be compared to resonance parameters obtained for the analogue by Richard et al. (1971). They observed the proton elastic scattering from a thick ^{90}Zr target (200 μg/cm^2), which had the effect of averaging the fine structure fluctuations in the cross

section. They obtained a proton width $\Gamma_p = 33 \pm 1.7$ keV, a spreading width $W_o = 42 \pm 3.3$ keV, and an analogue energy $E_R = 5.925 \pm 0.003$ MeV. Thus agreement with the present work is obtained for the spreading width, but not for the analogue proton width or analogue energy. However, as discussed by Browne (1969), reliable estimates of analogue state parameters are difficult to obtain from thick target measurements unless the shape of the energy resolution function is known precisely. This probably accounts for the small discrepancies in these values.

Lane (1969) has shown that Robson's single channel model leads to expressions for the spreading width W_o and the asymmetry parameter Δ.

$$\Delta_R = - \gamma_R^2 \, \Delta L \qquad (4.4.1)$$

$$W_o = 2\pi S_o \gamma_R^2 \, (\Delta L)^2 \qquad (4.4.2)$$

Here, L is defined as

$$\Delta L = \frac{\langle \eta | \Delta \mathcal{L} | \lambda \rangle}{\gamma_\eta \, \gamma_\lambda} \qquad (4.4.3)$$

and is essentially the difference between the internal and external logarithmic derivatives (L). For the ^{91}Nb analogue, the values $\Delta = -48 \pm 17$ keV and $W_o = 6.3 \pm 1.3$ keV are obtained. A large disagreement between the experimental value and the Robson estimate for the spreading width can

sometimes be explained in terms of analogue decay through other reaction channels. In this case however, the spectroscopic information gained from the $^{90}Zr(d,p)$ and $^{90}Zr(^{3}He,d)$ studies (section 4.6) would indicate that the single channel approximation is experimentally justified. The discrepancy between predicted and experimental spreading widths therefore remains unexplained.

4.5 Statistical Distributions

In some sense, the analogue state acts as a magnifying glass for examining the spacing distribution of the background levels. Away from the analogue, too many levels are missed to place much faith in the observed distribution. Near the center, however, a very large fraction of the background levels should have observable laboratory widths. The resonance spacings should assume a Wigner distribution in this region.

The observed spacing distribution may be used as a check on the cross section fits. If they follow a Wigner distribution, one's confidence in the fits is enhanced. Conversely, the degree and nature of any deviations from the Wigner may indicate flaws in the fitting procedure. The distribution of observed resonance spacings in the energy interval 5.87 to 5.93 MeV (level density greater than 1.4 keV^{-1}) are plotted as a histogram in figure 4.5. The fit to

Figure 4.5 The nearest neighbor resonance spacing distribution. Only resonances between 5.87 and 5.93 MeV are included.

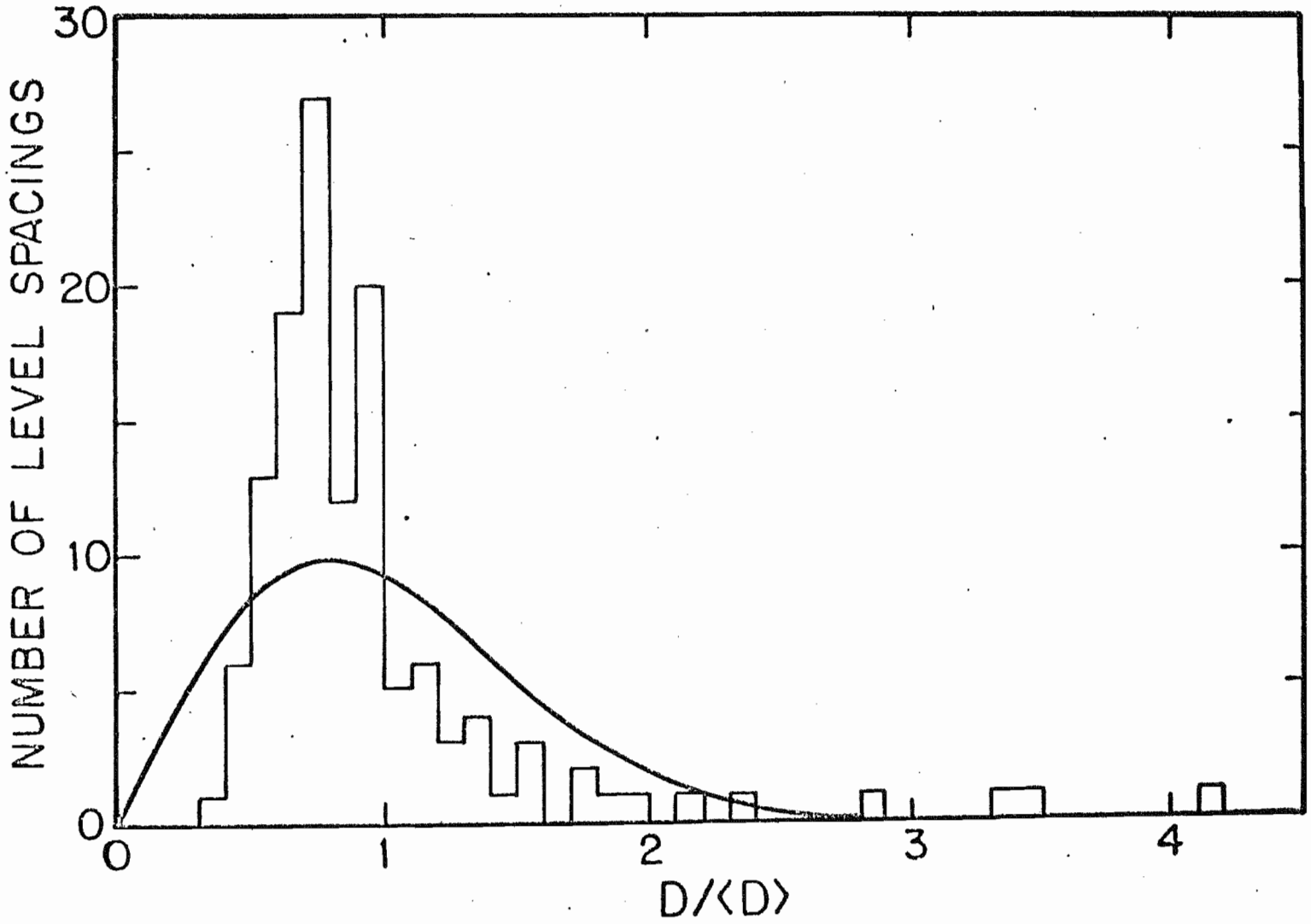
NUMBER OF LEVEL SPACINGS
30
20
10
0
0
1
2
3
4
D/⟨D⟩

the cross section in this region contains 132 s-wave resonances. A Wigner distribution normalized for 131 spacings is superimposed on the data. Two features are immediately apparent. First, more large spacings (for which $D/\langle D\rangle > 3$) occur than a Wigner distribution would indicate. In addition the data is much more sharply peaked in the region $0.5 < D/\langle D\rangle < 1.0$. One explanation might be that levels are being missed at random, either because the laboratory widths are below the threshhold of observability or because weak levels in close proximity to strong levels are being ignored. To test this hypothesis a randomly sequenced set of 500 resonance energies whose spacings followed a Wigner distribution was generated. 50 levels were removed at random and the spacing distribution recalculated, followed by the random removal of 50 more levels etc. The process was repeated many times and the distributions were averaged together at each stage. The resulting frequency functions are shown in figure 4.6. Random level removal would seem to explain a few large spacings. This is consistent with the observed energy dependence in the level density. Assuming a constant level density equal to the largest observed value indicates that about 12% of the levels have been missed. On the other hand, the width of the peak in the spacing distribution seems unaffected by random removal of levels, though the centroid appears to move down relative to the Wigner peak.

Figure 4.6 Simulation of the effects of random level removal from a randomly sequenced set of levels whose spacings follow a Wigner frequency function.

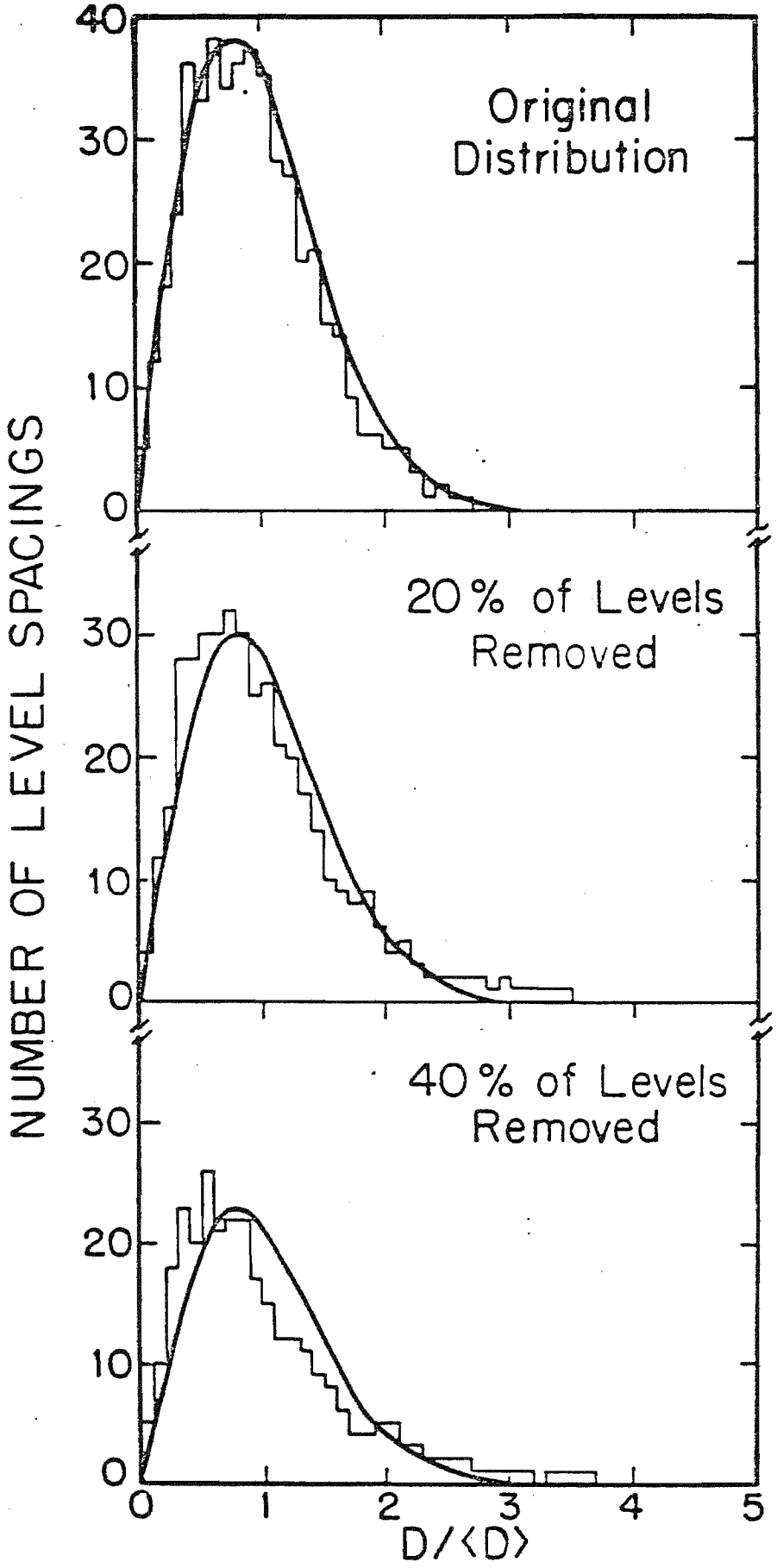
Original
Distribution
20% of Levels
Removed
40% of Levels
Removed
NUMBER OF LEVEL SPACINGS
D/⟨D⟩
0
10
20
30
40
0
1
2
3
4
5

This effect is probably related to the increase in <D> as levels are removed. It seems likely that the sharply peaked distribution of the resonance spacings reflects the tendency, when fitting cross section data in which the resonance lineshapes are not clearly defined, to insert resonances at approximately equal energy intervals and then adjust the resonance widths to improve the fit. This would result in many levels with approximately average spacing and very few small spacings, as observed.

The distribution of reduced widths is expected to assume a Porter-Thomas frequency function away from the analogue. In practice the presence of a highly fragmented analogue does not radically change the width distribution. Figure 4.7 shows the ^{90}Zr(p,p) width distribution for the data discussed above. The Porter-Thomas distribution is superimposed on the histogram. The dashed line indicates the minimum observable value of Y

$$Y_M = \frac{\Gamma_M}{2\rho\langle\gamma^2\rangle} \qquad (4.5.1)$$

where Γ_M = 15 eV. Integration of equation (2.4.2) from Y_M to infinity indicates that 25-30% of the levels are too small to be seen. However the experimental distribution shows no levels with $5 < Y < 10$. This effect may be due to the influence of the analogue state or some systematic error in the fitting procedure. In any case, this 'hole' in the distribution represents only about 2% of the levels and thus

Figure 4.7 The distribution of resonance reduced widths. Only levels between 5.87 and 5.93 MeV are included.

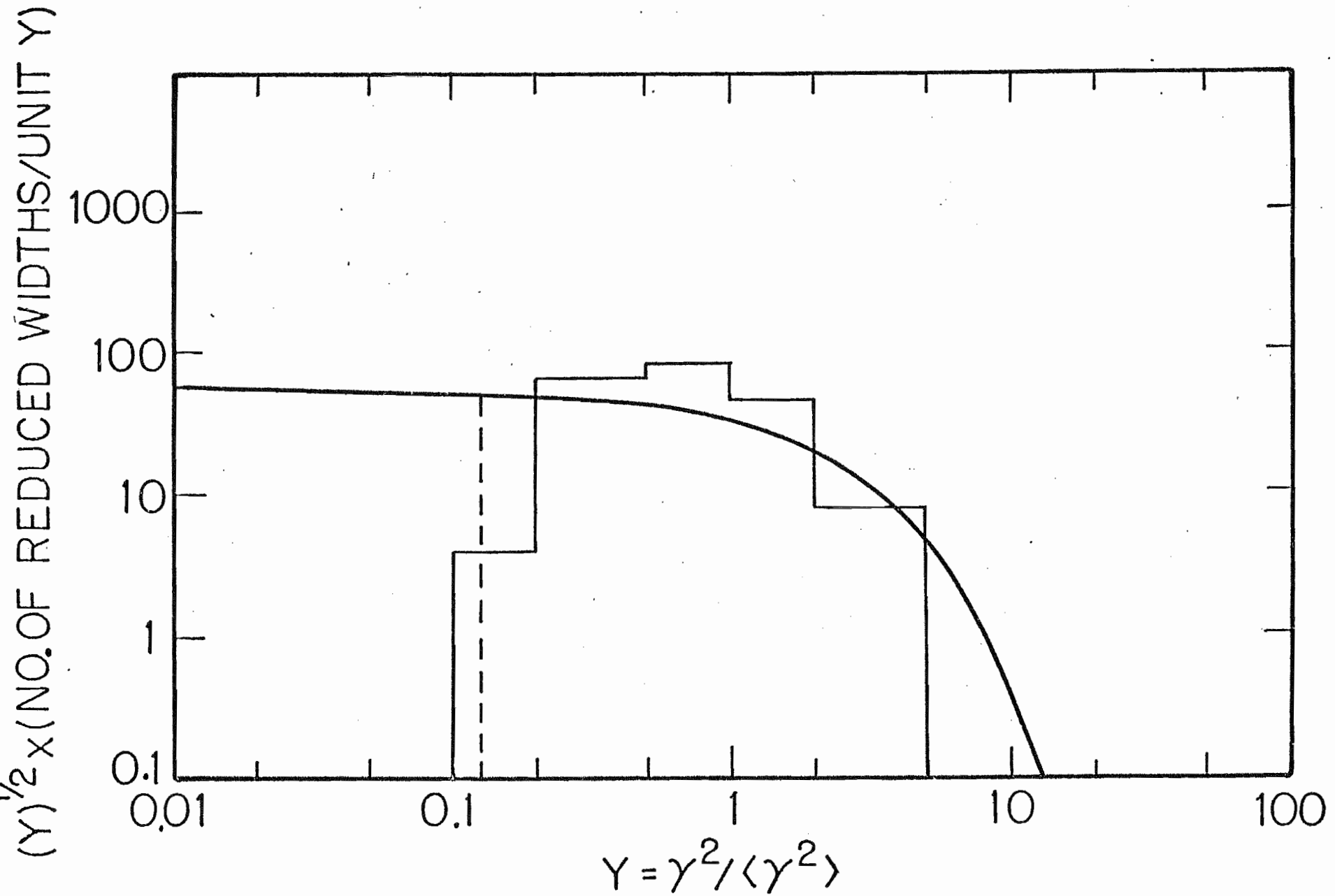
$(Y)^{1/2} \times$ (NO. OF REDUCED WIDTHS/UNIT Y)
1000
100
10
1
0.1
0.01
0.1
1
10
100
$Y = \gamma^2/\langle\gamma^2\rangle$

is not considered significant.

4.6 Single Particle Widths and Spectroscopic Factors

Single particle widths used to extract proton spectroscopic factors may be calculated in a number of ways. The computer code 'HANS', written by Harney (1969), calculates single particle widths in three different ways. These widths are designated ZDH (method of Zaidi, Darmodjo, and Harney (1967)), MM (method of Mekjian and MacDonald (1968)), and TAR (method of Thompson, Adams, and Robson (1968)). These methods are discussed in a paper by Harney and Weidenmuller (1969). ZDH and MM are shell model calculations while TAR employs an R-matrix approach. The input to the code includes target information (A and Z), the analogue state parameters (l, J, and E_A), parent state parameters (principal quantum number N and the parent state neutron separation energy), and optical model parameters as follows; all radii = 1.25 $A^{1/3}$ fermis, each diffuseness = 0.67 fermis, V_{so} = 8 MeV, and W = 0. The code starts with $V_p = V_n$ and searches for a neutron potential which gives the proper neutron separation energy. A more accurate proton potential is then obtained by adding a symmetry potential of the form

$$V_{SYM} = -\left[\frac{2T_0+1}{2}\right]\frac{125}{A} \qquad (4.6.1)$$

to the neutron well depth obtained in the search. The calculation is then repeated to calculate the single particle widths.

A proton single particle width may be obtained for comparison with the above methods by calculating the phase shifts for a proton incident on a real Wood-Saxon potential with a Thomas type spin-orbit term. The radius and diffuseness are given by $1.25\ A^{1/3}$ fermis and 0.65 fermis, respectively. The spin orbit potential is fixed at 8 MeV. With the excitation energy fixed at the analogue energy, the well depth is varied until the scattering phase shift equals $\pi/2$. The well depth is then fixed and the width is taken to be the interval in excitation energy in which the phase shift changes from $\pi/4$ to $3\pi/4$.

The residual interaction between the excess neutron and the core in ^{91}Zr are expected to be quite small due to the closed shell character of ^{90}Zr. Thus the spectroscopic factors of the single particle states should be large. Table 4.1 summarizes the results of the present work along with calculations, using the methods described above, of spectroscopic factors for 3 other analogue states in ^{91}Nb whose proton widths appear in the literature. Neutron spectroscopic factors from various $^{90}Zr(d,p)$ experiments (CC: Cohen and Chubinsky (1963), BH: Bingham and Halbert (1970), and G: Graue et al. (1972)) are included. Analogue proton widths and spectroscopic factors derived from the

Table 4.1

J^{π}	E_p (MeV)	Γ_p (keV)	$\Gamma_{sp}/(2T_o+1)$ ORIG	MM	ZDH	NT	TAR	S_p ORIG	MM	ZDH	NT	TAR	S_{dp} CC	BH	G
$5/2^{+1}$	4.71	4.0±.5	4.25	4.70	4.65	4.57	3.78	0.94	0.85	0.86	0.87	1.06	0.89	1.04	0.95
$1/2^{+}$	5.91	23.8±5		81.5	81.0	80.7	61.2		0.29	0.29	0.29	0.39	0.72	0.93	0.70
$3/2^{+2}$	6.86	15.0	39.3	50.0	49.7	53.4	41.0	0.38	0.30	0.30	0.28	0.37	0.45	0.63	0.48
$7/2^{+2}$	7.06	2.5	3.2	1.88	1.86	1.81	1.73	0.78	1.33	1.34	1.38	1.44	0.52	0.48	0.49

[1]H.L. Scott, C.P. Swann, and F. Rauch, Nucl. Phys. A134 (1969) 667.

[2]K.P. Lieb, J.J. Kent, and C. F. Moore, Phys. Rev. 175 (1968) 1482.

proton-in-a-real-well method are designated NT (no theory).

The neutron spectroscopic factors are indeed quite large ($S_{dp} > 0.5$ in most cases). In general the trend towards $S_{dp} > S_p$ is followed, except in the case of the 7/2+ analogue. However the observed proton width in this case is quite small and might easily be in error. Good agreement is obtained among the methods of MM, ZDH, and NT. The TAR method typically gives a smaller width and thus a larger spectroscopic factor.

In their original paper, Thompson et al. obtain a single particle width $\Gamma_{sp} = 40$ keV for the 1/2+ analogue. However, they use a slightly different set of optical model parameters with a non-zero imaginary component of the proton well. The value given by the NT method for the 1/2+ state also deserves some qualification. In this case the phase shift increases with excitation energy to slightly above 130° but never reaches $3\pi/4$. In this mass region, the phase shift is highly asymmetric about $\pi/2$. The calculation was done for the 1/2+ analogue in ^{93}Tc and the ratio of the half widths ($\Gamma_{1/2}$ from $\pi/4$ to $\pi/2$ and $\Gamma_{1/2}$ from $\pi/2$ to $3\pi/4$) was found to be 1.6. This ratio was used to compute the single particle width (NT) for ^{91}Nb.

The proton spectroscopic factor extracted for the 1/2+ state lies in the range 0.3-0.4, which is rather small compared to the anti-analogue spectroscopic factor (0.92) obtained by Vourvopolis et al. (1969), and the neutron

spectroscopic factors arising from (d,p) measurements. However, the disagreement with the (d,p) work also exists for the ^{93}Tc analcgue studied by Outlaw. Furthermore, there is considerable variation in the quoted values of S_{dp}. The smaller ones (CC and G) give spectroscopic factor ratios (S_p/S_{dp}) between 0.41 and 0.54 consistent with the general trend discussed in section 2.6.

Chapter 5

CONCLUSION

The differential cross section for the $^{90}Zr(p,p)$ reaction has been measured at four laboratory angles in the energy range 5.684 to 5.992 MeV. The data has been fit to an R-matrix cross section which includes 302 $1/2^+$ resonances. These comprise the fine structure of the lowest $1/2^+$ analogue state in ^{91}Nb. Proton energy resolution of 425 to 450 eV was maintained for most of the measurement.

Excellent beam energy resolution has been achieved through use of a triple loop energy regulating system developed specifically for this experiment. This system reduces time dependent proton energy fluctuations to less than 100 eV without employing a target correction voltage. In addition an improved analyzing magnet control system has been developed which allows extremely precise, automated control of the absolute proton energy.

Despite the fact that both of these systems have met

their respective design goals, the fine structure of the 5.91 MeV analogue in ^{91}Nb has not been totally resolved. The extremely high level density results in extensive level interference which prevents the extraction of unambiguous resonance parameters in some sections of the data. Nevertheless, the fine structure distribution has been fit using the Lane strength function. This procedure yielded good values for the analogue energy, analogue proton width, and analogue spreading width. The asymmetry parameters and background strength function are somewhat less well determined. The proton spectroscopic factor for the analogue disagrees sharply with the parent state values extracted from (d,p) experiments. This discrepancy is consistent with the bulk of the analogue state data accumulated at TUNL and in particular with the measurement of the 1/2$^+$ analogue in ^{93}Tc.

The TUNL tandem Van de Graaff, equipped with the three loop energy stabilizer, will continue to be a useful tool in high resolution nuclear spectroscopy. At present a series of angular correlation measurements in the proton inelastic scattering from ^{54}Fe is in progress. However, future experiments in high level density nuclei such as ^{91}Nb will require better energy resolution than that obtained in the present work. To obtain a total instrumental resolution of 250 to 350 eV, it will be necessary to reduce the energy straggling in the terminal stripper. This may be possible

through the use of ultra-thin (<1 g/cm^2) stripping foils or a different stripping gas. If this level of performance can be realized, a number of very interesting experiments dealing with the fine structure of analogue states can be carried out in the mass region $70 < A < 90$.

Appendix I

This appendix contains the resonance parameters extracted from the multi-level R-matrix fitting procedure described in section 4.1. For each resonance, a laboratory proton energy, spin-parity, laboratory proton width and reduced proton width are listed in table I.1. The error in the relative energy spacing of adjacent resonances is on the order of 150 eV. The errors associated with the laboratory widths reflect the relative 'goodness of fit' obtained by varying the resonance parameters during the fitting procedure. Resonances enclosed in parentheses satisfy the conditions

$$D_M \leq \sqrt{\Gamma_p^2 + \Delta^2}$$

where Δ is the resolution width and D_M is the smaller nearest neighbor spacing associated with that resonance.

Table I.1

E (MeV)	J^{π}	Γ_p (eV)	γ_p^2 (eV)
5.68420	1/2+	10 +/- 5	11
5.68650	1/2+	20 +/- 5	23
5.69352	1/2+	45 +/- 11	51
5.69560	1/2+	40 +/- 10	45
5.70070	1/2+	20 +/- 5	23
5.70788	1/2+	38 +/- 9	43
5.70912	1/2+	50 +/- 12	56
5.71118	1/2+	20 +/- 5	22
5.71816	1/2+	30 +/- 7	33
5.71950	1/2+	14 +/- 5	16
5.72522	1/2+	16 +/- 5	18
5.72580	1/2+	49 +/- 12	54
5.72640	1/2+	77 +/- 15	85
5.72692	1/2+	48 +/- 12	53
5.72766	1/2+	30 +/- 7	33
5.72904	1/2+	24 +/- 6	27
5.73118	1/2+	80 +/- 16	88
5.73472	1/2+	35 +/- 9	39
5.73524	1/2+	30 +/- 7	33
5.73798	1/2+	25 +/- 6	27
5.73854	1/2+	75 +/- 15	82
5.73946	1/2+	35 +/- 9	38
5.74016	1/2+	30 +/- 7	33
5.74482	1/2+	36 +/- 9	39
5.74762	(1/2-)	35 +/- 9	55

E (MeV)	J^{π}	Γ_p (eV)	γ_p^2 (eV)
5.74883	(1/2-)	32 +/- 8	50
(5.74998	1/2+	55 +/- 11	60)
(5.75040	1/2+	84 +/- 17	91)
5.75140	(1/2-)	15 +/- 5	24
5.75240	(1/2-)	15 +/- 5	24
5.75354	1/2+	21 +/- 5	23
5.75653	1/2+	25 +/- 6	27
(5.75902	1/2+	30 +/- 7	32)
(5.75940	1/2+	19 +/- 5	20)
5.76034	1/2+	78 +/- 16	84
(5.76473	1/2+	45 +/- 11	48)
(5.76506	1/2+	35 +/- 9	38)
5.76690	(1/2-)	25 +/- 6	39
5.76736	(1/2-)	25 +/- 6	39
5.76832	1/2+	40 +/- 10	43
(5.76989	1/2+	36 +/- 9	39)
(5.77018	1/2+	26 +/- 6	28)
5.77072	1/2+	19 +/- 5	20
(5.77343	1/2+	25 +/- 6	27)
(5.77358	(1/2-)	45 +/- 11	69)
(5.77392	1/2+	42 +/- 10	45)
(5.77420	1/2+	23 +/- 6	25)
(5.77453	1/2+	13 +/- 5	14)
(5.77760	1/2+	30 +/- 7	32)
(5.77802	1/2+	80 +/- 16	85)

E (MeV)	J^{π}	Γ_p (eV)	γ_p^2 (eV)
(5.77986	(1/2-)	45 +/- 11	69)
(5.78010	1/2+	36 +/- 9	38)
5.78180	1/2+	22 +/- 5	23
5.78528	1/2+	29 +/- 7	31
5.78682	1/2+	51 +/- 10	54
5.78756	1/2+	52 +/- 10	55
5.79028	1/2+	21 +/- 5	22
5.79084	1/2+	19 +/- 5	20
5.79268	1/2+	20 +/- 5	21
(5.79316	1/2+	13 +/- 5	14)
(5.79350	1/2+	19 +/- 5	20)
(5.79566	1/2+	60 +/- 12	63)
(5.79590	1/2+	50 +/- 12	52)
(5.79680	1/2+	24 +/- 6	25)
(5.79686	1/2+	35 +/- 9	37)
5.79822	1/2+	30 +/- 7	31
5.79942	1/2+	32 +/- 8	33
5.80070	(1/2-)	30 +/- 7	45
5.80202	1/2+	40 +/- 10	42
5.80294	1/2+	20 +/- 5	21
5.80350	1/2+	25 +/- 6	26
5.80528	1/2+	33 +/- 8	34
5.80636	(1/2-)	20 +/- 5	30
5.80846	1/2+	19 +/- 5	20
5.80938	1/2+	29 +/- 7	30

E (MeV)	J^{π}	Γ_p (eV)	γ_p^a (eV)
5.81086	1/2+	20 +/- 5	21
5.81131	1/2+	40 +/- 10	41
(5.81246	1/2+	25 +/- 6	26)
(5.81278	1/2+	39 +/- 10	40)
(5.81312	1/2+	20 +/- 5	21)
5.81430	1/2+	30 +/- 7	31
5.81692	1/2+	38 +/- 9	39
5.81750	1/2+	20 +/- 5	21
(5.81799	1/2+	19 +/- 5	20)
(5.81840	1/2+	25 +/- 6	26)
(5.81983	1/2+	20 +/- 5	21)
(5.82018	1/2+	48 +/- 12	49)
5.82100	1/2+	24 +/- 6	25
5.82217	1/2+	64 +/- 13	66
5.82260	1/2+	24 +/- 6	25
5.82773	1/2+	80 +/- 16	82
(5.82832	1/2+	42 +/- 10	43)
(5.82871	1/2+	29 +/- 7	30)
5.83262	1/2+	44 +/- 11	45
5.83410	1/2+	30 +/- 7	31
5.83464	1/2+	60 +/- 12	61
5.83568	1/2+	55 +/- 11	56
5.83654	1/2+	95 +/- 19	96
5.83704	1/2+	106 +/- 16	108
(5.83959	1/2+	29 +/- 7	29)

E (MeV)	J^{π}	Γ_p (eV)	γ^2_p (eV)
(5.83996	1/2+	65 +/- 13	66)
5.84039	1/2+	25 +/- 6	25
5.84087	1/2+	36 +/- 9	36
5.84165	1/2+	50 +/- 12	51
5.84300	1/2+	60 +/- 12	61
5.84350	1/2+	40 +/- 10	40
5.84423	1/2+	21 +/- 5	21
(5.84505	1/2+	39 +/- 10	39)
(5.84538	1/2+	77 +/- 15	78)
(5.84574	1/2+	42 +/- 10	42)
(5.84940	1/2+	150 +/- 22	151)
(5.84953	1/2+	43 +/- 11	43)
(5.85019	1/2+	90 +/- 18	90)
(5.85048	1/2+	52 +/- 10	52)
5.85138	1/2+	44 +/- 11	44
(5.85370	1/2+	140 +/- 21	140)
(5.85392	(1/2-)	35 +/- 9	50)
5.85440	1/2+	42 +/- 10	42
5.85570	1/2+	32 +/- 8	32
5.85615	1/2+	29 +/- 7	29
5.85664	1/2+	65 +/- 13	65
5.85712	1/2+	31 +/- 8	31
(5.85910	1/2+	32 +/- 8	32)
(5.85942	1/2+	60 +/- 12	60)
(5.85984	1/2+	40 +/- 10	40)

E (MeV)	J^{π}	Γ_p (eV)	γ_p^2 (eV)
5.86121	1/2+	15 +/- 5	15
(5.86227	1/2+	42 +/- 10	42)
(5.86260	1/2+	98 +/- 20	98)
(5.86503	1/2+	25 +/- 6	25)
(5.86538	1/2+	83 +/- 17	82)
(5.86562	1/2+	60 +/- 12	60)
(5.86974	1/2+	73 +/- 15	72)
5.87017	1/2+	48 +/- 12	48
(5.87078	1/2+	82 +/- 16	81)
(5.87110	1/2+	63 +/- 13	62)
(5.87143	1/2+	40 +/- 10	40)
(5.87174	1/2+	100 +/- 20	99)
5.87363	1/2+	25 +/- 6	25
(5.87427	1/2+	45 +/- 11	44)
(5.87468	1/2+	39 +/- 10	38)
(5.87551	1/2+	72 +/- 14	71)
(5.87590	1/2+	54 +/- 11	53)
5.87638	1/2+	120 +/- 18	118
5.87710	1/2+	40 +/- 10	39
(5.87760	1/2+	94 +/- 19	93)
(5.87802	1/2+	120 +/- 18	118)
(5.87847	1/2+	80 +/- 16	79)
5.87877	1/2+	175 +/- 26	172
(5.87900	1/2+	50 +/- 12	49)
5.87971	1/2+	70 +/- 14	69

E_p (MeV)	J^π	Γ_p (eV)	γ_p^2 (eV)
5.88016	1/2+	60 +/- 12	59
(5.88069	1/2+	60 +/- 12	59)
(5.88105	1/2+	43 +/- 11	42)
(5.88380	1/2+	120 +/- 18	118)
(5.88408	1/2+	150 +/- 22	147)
5.88479	1/2+	30 +/- 7	29
(5.88535	1/2+	53 +/- 11	52)
(5.88576	1/2+	44 +/- 11	43)
(5.88617	1/2+	45 +/- 11	44)
(5.88658	1/2+	130 +/- 19	127)
(5.88692	1/2+	115 +/- 17	112)
(5.88730	1/2+	60 +/- 12	59)
(5.88764	1/2+	40 +/- 10	39)
(5.88798	1/2+	51 +/- 10	50)
(5.88831	1/2+	80 +/- 16	78)
5.88861	1/2+	237 +/- 36	231
(5.88898	1/2+	70 +/- 14	68)
(5.88986	1/2+	30 +/- 7	29)
(5.89023	1/2+	44 +/- 11	43)
(5.89072	1/2+	135 +/- 20	132)
(5.89104	1/2+	75 +/- 15	73)
(5.89132	1/2+	135 +/- 20	131)
5.89164	1/2+	232 +/- 35	226
(5.89183	1/2+	120 +/- 18	117)
5.89213	1/2+	175 +/- 26	170

E_p (MeV)	J^π	Γ_p (eV)	γ_p^a (eV)
(5.89368	1/2+	40 +/- 10	39)
(5.89405	1/2+	30 +/- 7	29)
(5.89556	1/2+	80 +/- 16	78)
(5.89591	1/2+	135 +/- 20	131)
(5.89630	1/2+	100 +/- 20	97)
5.89661	1/2+	300 +/- 45	291
5.89694	1/2+	400 +/- 60	388
5.89726	1/2+	250 +/- 37	242
(5.89751	1/2+	120 +/- 18	116)
(5.89784	1/2+	120 +/- 18	116)
(5.89812	1/2+	115 +/- 17	111)
(5.89840	1/2+	70 +/- 14	68)
(5.89860	1/2+	70 +/- 14	68)
5.89990	1/2+	90 +/- 18	87
(5.90086	1/2+	120 +/- 18	116)
(5.90126	1/2+	115 +/- 17	111)
(5.90183	1/2+	65 +/- 13	63)
(5.90204	1/2+	29 +/- 7	28)
5.90236	1/2+	186 +/- 28	180
5.90274	1/2+	300 +/- 45	290
5.90302	1/2+	260 +/- 39	251
(5.90333	1/2+	140 +/- 21	135)
(5.90395	1/2+	63 +/- 13	61)
(5.90425	1/2+	62 +/- 12	60)
(5.90474	1/2+	150 +/- 22	145)

E_ρ (MeV)	J^π	Γ_ρ (eV)	γ^2_{ρ} (eV)
5.90510	1/2+	164 +/- 25	158
(5.90560	1/2+	140 +/- 21	135)
(5.90595	1/2+	90 +/- 18	87)
(5.90620	1/2+	127 +/- 19	122)
5.90654	1/2+	280 +/- 42	270
5.90696	1/2+	400 +/- 60	385
5.90740	1/2+	161 +/- 24	155
5.90784	1/2+	220 +/- 33	212
(5.90828	1/2+	130 +/- 19	125)
(5.90887	1/2+	131 +/- 20	126)
5.90930	1/2+	360 +/- 54	346
5.90959	1/2+	280 +/- 42	269
5.91010	1/2+	100 +/- 20	96
5.91055	1/2+	70 +/- 14	67
(5.91135	1/2+	105 +/- 16	101)
(5.91165	1/2+	85 +/- 17	82)
(5.91212	1/2+	89 +/- 18	85)
(5.91254	1/2+	45 +/- 11	43)
(5.91310	1/2+	30 +/- 7	29)
(5.91336	1/2+	65 +/- 13	62)
(5.91368	1/2+	110 +/- 16	105)
(5.91410	1/2+	80 +/- 16	77)
(5.91472	1/2+	40 +/- 10	38)
(5.91511	1/2+	102 +/- 15	98)
(5.91540	1/2+	120 +/- 18	115)

E_p (MeV)	J^π	Γ_p (eV)	γ_p^2 (eV)
5.91570	1/2+	210 +/- 31	201
5.91599	1/2+	280 +/- 42	268
5.91620	1/2+	350 +/- 52	335
5.91656	1/2+	210 +/- 31	201
(5.91692	1/2+	120 +/- 18	115)
5.91729	1/2+	163 +/- 24	156
5.91756	1/2+	170 +/- 25	162
(5.91776	1/2+	87 +/- 17	83)
(5.91799	1/2+	40 +/- 10	38)
(5.91824	1/2+	62 +/- 12	59)
5.91847	1/2+	170 +/- 25	162
5.91878	1/2+	575 +/- 86	549
5.91928	1/2+	350 +/- 52	334
5.91970	1/2+	170 +/- 25	162
(5.92020	1/2+	80 +/- 16	76)
(5.92056	1/2+	60 +/- 12	57)
5.92102	1/2+	220 +/- 33	210
5.92137	1/2+	310 +/- 46	295
5.92160	1/2+	164 +/- 25	156
5.92183	1/2+	202 +/- 30	192
5.92207	1/2+	265 +/- 40	252
5.92224	1/2+	161 +/- 24	153
5.92256	1/2+	162 +/- 24	154
5.92292	1/2+	200 +/- 30	190
(5.92318	1/2+	84 +/- 17	80)

E_p (MeV)	J^π	Γ_p (eV)	γ_p^2 (eV)
(5.92352	1/2+	135 +/- 20	128)
(5.92392	1/2+	107 +/- 16	102)
(5.92420	1/2+	125 +/- 19	119)
5.92440	1/2+	180 +/- 27	171
5.92476	1/2+	200 +/- 30	190
(5.92520	1/2+	148 +/- 22	141)
(5.92558	1/2+	65 +/- 13	62)
(5.92592	1/2+	75 +/- 15	71)
(5.92696	1/2+	77 +/- 15	73)
5.92720	1/2+	159 +/- 24	151
5.92765	1/2+	120 +/- 18	114
5.92810	1/2+	47 +/- 12	45
5.92890	1/2+	30 +/- 7	28
5.92934	1/2+	35 +/- 9	33
5.93136	1/2+	63 +/- 13	60
5.93186	1/2+	32 +/- 8	30
5.93356	1/2+	36 +/- 9	34
(5.93443	1/2+	125 +/- 19	118)
5.93485	1/2+	160 +/- 24	151
(5.93594	1/2+	50 +/- 12	47)
(5.93622	1/2+	85 +/- 17	80)
(5.93656	1/2+	47 +/- 12	44)
(5.93684	1/2+	70 +/- 14	66)
(5.93720	1/2+	57 +/- 11	54)
5.93832	1/2+	40 +/- 10	38

E_p (MeV)	J^π	Γ_p (eV)	γ_p^2 (eV)
(5.93880	1/2+	55 +/- 11	52)
(5.93914	1/2+	75 +/- 15	71)
(5.93944	1/2+	55 +/- 11	52)
(5.93978	1/2+	30 +/- 7	28)
(5.94000	1/2+	30 +/- 7	28)
(5.94025	1/2+	80 +/- 16	75)
(5.94044	1/2+	75 +/- 15	70)
(5.94080	1/2+	50 +/- 12	47)
(5.94114	1/2+	102 +/- 15	96)
(5.94148	1/2+	51 +/- 10	48)
(5.94180	1/2+	90 +/- 18	84)
(5.94200	1/2+	67 +/- 13	63)
(5.94226	1/2+	90 +/- 18	84)
(5.94260	1/2+	150 +/- 22	141)
(5.94298	1/2+	45 +/- 11	42)
(5.94384	1/2+	50 +/- 12	47)
(5.94424	1/2+	45 +/- 11	42)
(5.94472	1/2+	29 +/- 7	27)
(5.94502	1/2+	56 +/- 11	52)
(5.94558	1/2+	50 +/- 12	47)
(5.94584	1/2+	50 +/- 12	47)
(5.94669	1/2+	55 +/- 11	51)
(5.94700	1/2+	30 +/- 7	28)
5.94878	1/2+	30 +/- 7	28
5.94958	1/2+	40 +/- 10	37

E_p (MeV)	J^π	Γ_p (eV)	γ_p^2 (eV)
5.95016	1/2+	48 +/- 12	45
5.95070	1/2+	70 +/- 14	65
5.95214	1/2+	20 +/- 5	19
5.95415	1/2+	40 +/- 10	37
5.95480	1/2+	30 +/- 7	28
5.95550	(1/2-)	30 +/- 7	40
5.95700	1/2+	45 +/- 11	42
5.95860	1/2+	35 +/- 9	32
5.95916	(1/2-)	45 +/- 11	59
5.95970	1/2+	42 +/- 10	39
5.96140	1/2+	40 +/- 10	37
5.96224	(1/2-)	30 +/- 7	39
5.96330	1/2+	20 +/- 5	18
5.96470	1/2+	20 +/- 5	18
5.97118	1/2+	30 +/- 7	28
5.97204	(1/2-)	55 +/- 11	71
5.97390	1/2+	25 +/- 6	23
5.97550	(1/2-)	45 +/- 11	58
5.97726	(1/2-)	30 +/- 7	39
5.98034	(1/2-)	30 +/- 7	39

Appendix II

II.1 The Van de Graaff Terminal Installation

Several components of the triple loop stabilizer system are located within the high voltage terminal of the TUNL tandem accelerator. These are conveniently grouped into three sections; the high voltage amplifier, the power supplies, and the photomultiplier tube and its preamplifier. The high voltage amplifier is housed with the power supplies in an aluminum cabinet which is suspended within the low energy terminal compression fixture. The analogous position in the high energy fixture is occupied by the pulley for the charging belt. The stripper is connected to the high voltage amplifier by an insulated high voltage cable (RG8). One end attaches to the brass tubing which supplies gas to the stripper. The other end connects to the 'doorknob' type output electrode which protrudes from the top of the high voltage amplifier cabinet. Two additional cables enter this module from the bottom. One supplies the 400 Hz, 115 V power from the belt driven alternator. The other transports power to and signals from the phototube preamplifier. The phototube-preamp assembly is fixed to the left side of the terminal and faces the low energy viewing port. Figure II.1 illustrates the terminal installation with top and left side views. The 115 V power for this equipment is controlled by

Figure II.1 Top and left side views of the terminal installation. The dotted lines indicate the high voltage amplifier.

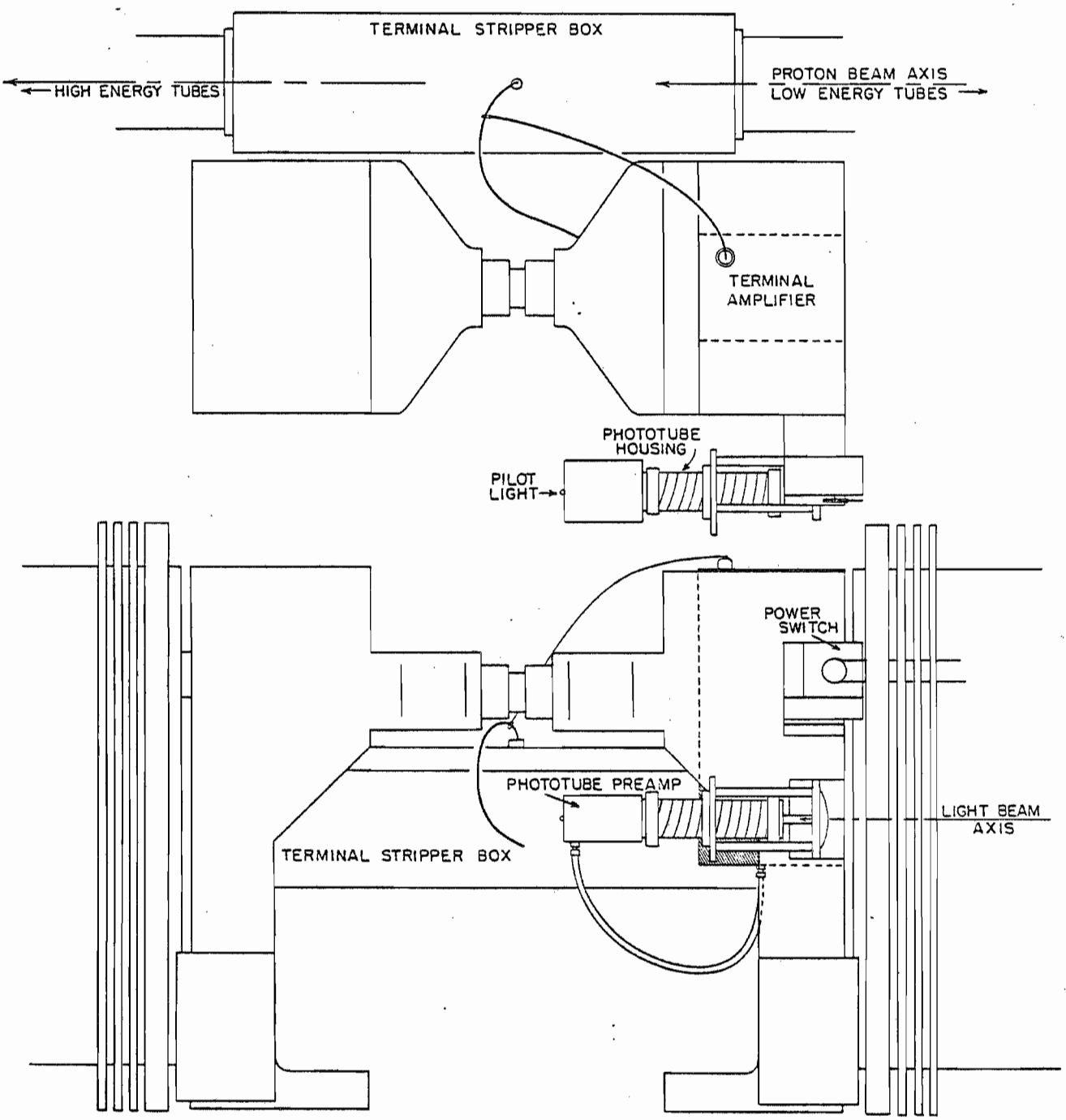
TERMINAL STRIPPER BOX
HIGH ENERGY TUBES
PROTON BEAM AXIS
LOW ENERGY TUBES
TERMINAL AMPLIFIER
PHOTOTUBE HOUSING
PILOT LIGHT
POWER SWITCH
PHOTOTUBE PREAMP
LIGHT BEAM AXIS
TERMINAL STRIPPER BOX

a string operated switch. A pilot light tied to the preamplifier filament supply serves as a power on indicator. This light may be seen from the high energy viewing port.

The circuit diagram for the high voltage amplifier is shown in figure II.2. The cathode of the upper tube rides at 4 kV. In this 'piggy back' configuration, the tube serves as a dynamic load resistor which improves the amplifier linearity for large output swings. The voltage gain of the amplifier is given by

$$\frac{V_o}{V_i} = \frac{g_m R_2}{1 + g_m R_1} \qquad (II.1.1)$$

The transconductance, g_m, of the Y634 triode is 50 μmhos which gives a voltage gain of about 50. There are several physical features which allow the amplifier to withstand the harsh terminal environment. The vacuum tubes are ceramic planar triodes designed for use in spacecraft communications equipment. The original tubes have shown no sign of deterioration after four years of use. Protection against transients from tank or tube sparks is partially provided by the double layered aluminum cabinet and single point ground layout of the terminal amplifier. The output and power input are protected by 15 kV spark gaps. In addition there is a high frequency choke coil in series with the load to inhibit transients. A 50 MΩ resistor is placed in parallel with the load to bleed off beam current intercepted by the

Figure II.2 Circuit diagram for the phototube preamp and high voltage amplifier.

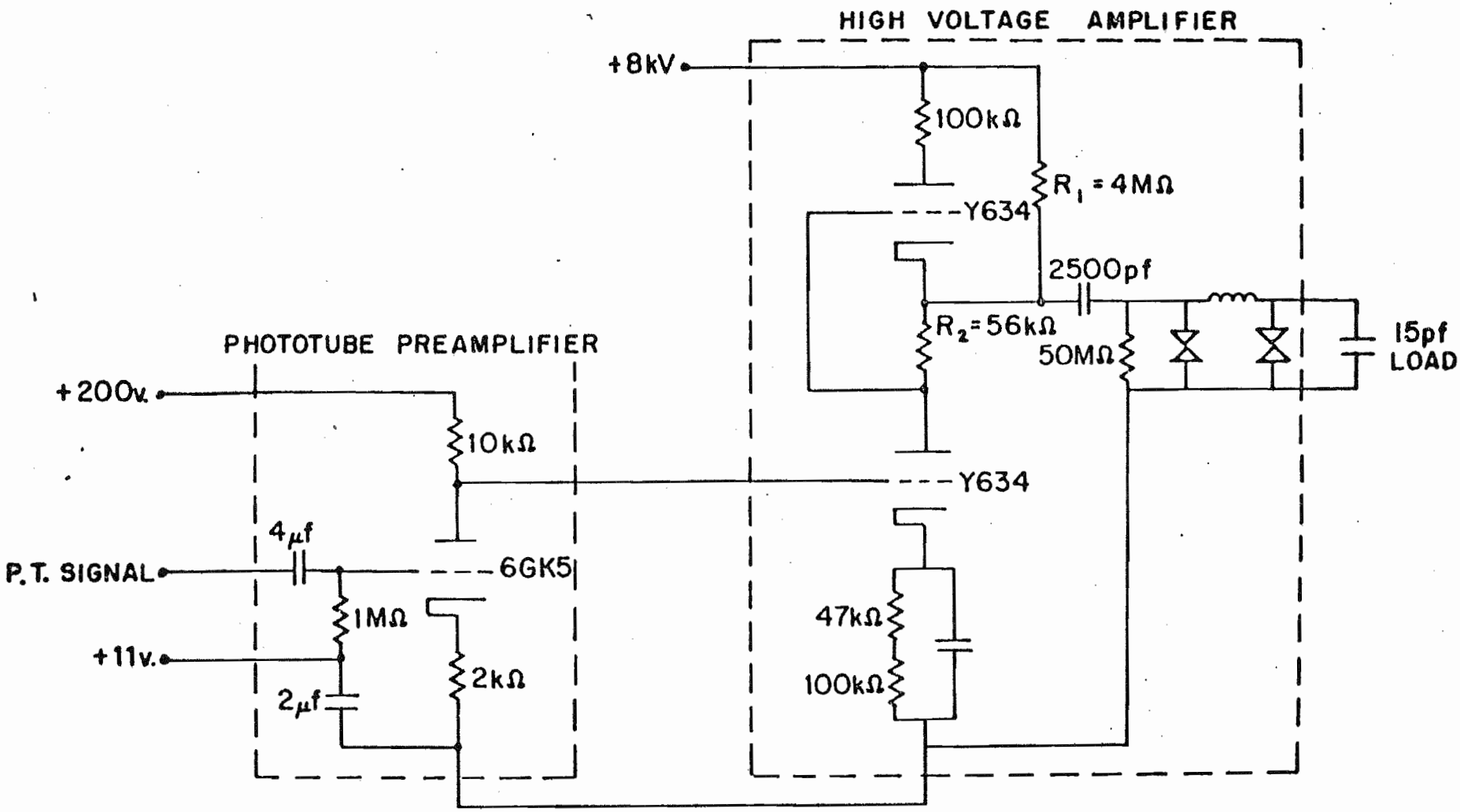
HIGH VOLTAGE AMPLIFIER
+8kV
100kΩ
R1 = 4MΩ
Y634
2500pf
R2 = 56kΩ
50MΩ
15pf
LOAD
PHOTOTUBE PREAMPLIFIER
+200v.
10kΩ
Y634
4μf
P.T. SIGNAL
6GK5
1MΩ
+11v.
2μf
2kΩ
47kΩ
100kΩ

stripper canal.

The phototube (RCA 6199) resides within a piece of 3" beam pipe mounted behind the collecting lens. The PM tube preamplifier, whose circuit diagram is also shown in figure II.2, is enclosed in an aluminum box fixed to one end of the phototube housing. The position of the phototube relative to the lens may be adjusted to focus the light on the photo cathode.

The power supplies are shown schematically in figure II.3. Rectification is provided by appropriately chosen silicon controlled rectifiers (SCR). The 11 V and 200 V supplies are shunt regulated by Zener diodes. The 800 V and 8 kV supplies are capacitively filtered. An isolation transformer supplies the filament current for the 'piggy back' tube which rides at 4 kV.

The unity gain frequency response H_T of the signal path from phototube to stripper is well approximated by

$$H_T = \left(\frac{sT_1}{1+sT_1}\right)\left(\frac{sT_2}{1+sT_2}\right)\left(\frac{1}{1+sT_3}\right) \qquad (II.1.2)$$

Here T_1 (4 sec) is the time constant associated with the preamplifier input coupling capacitor. The 2500 pf output coupling capacitor gives rise to T_2 (.125 sec) while the load capacitance is responsible for T_3 (55 μsec).

Figure II.3 Circuit diagram for the terminal power supply.

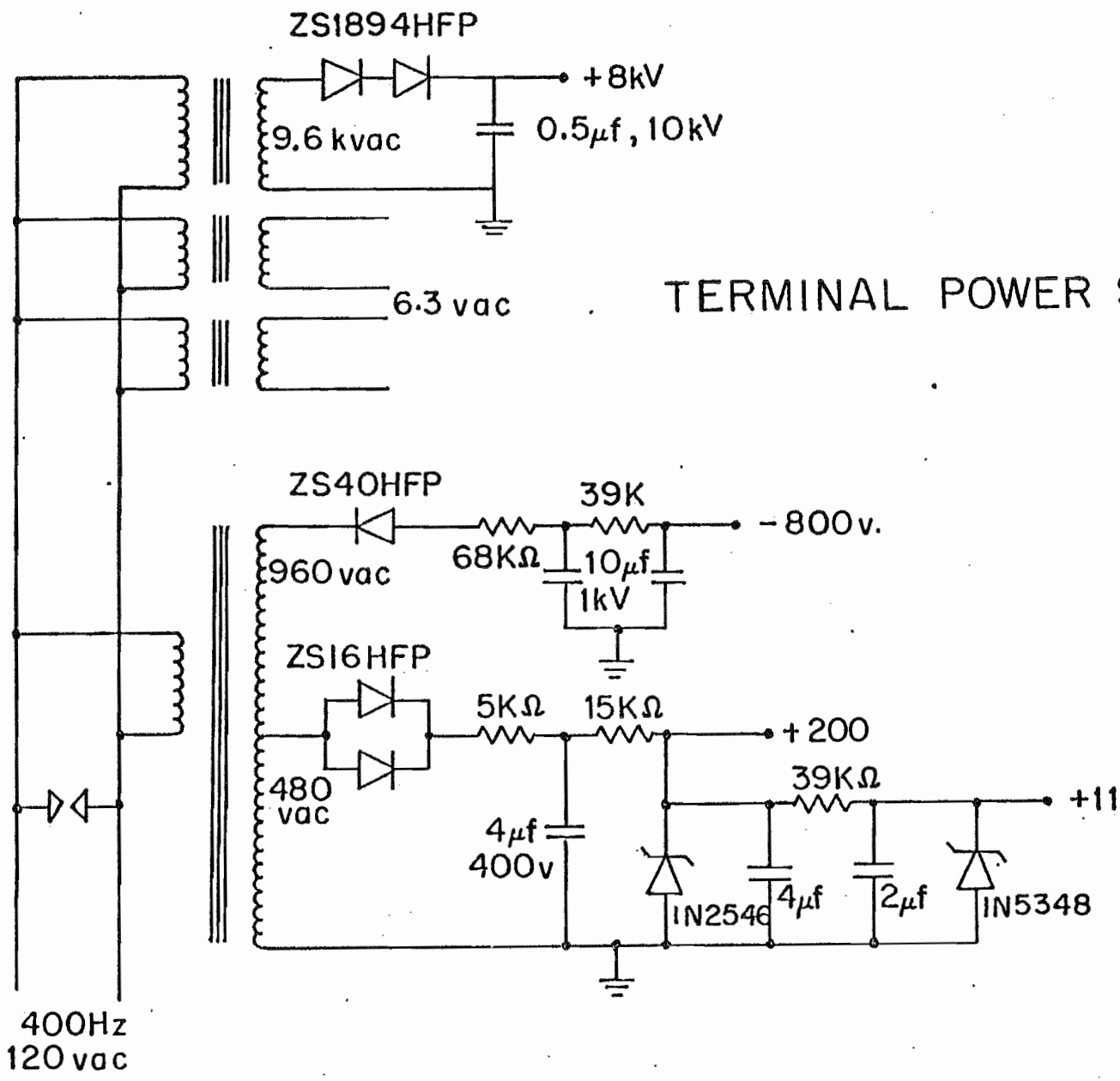

TERMINAL POWER SUPPLY

II.2 The LED Driver

The light output of a light emitting diode is proportional to the current which passes through it. However the current is not proportional to the voltage across the diode. In order to obtain linear light intensity modulation, a circuit whose current output is proportional to the input voltage is required. Such a circuit is shown in simplified form in figure II.4. The current through R is given by

$$I_s = \frac{V_i Z}{R_s R} \qquad (II.2.1)$$

If R is much greater than the diode impedance Z , then $I_s = I_o$ and the linearity condition is satisfied. The actual circuit is shown in figure II.5. An adjustable phase lead has been provided but in practice the coupling capacitor is shorted out for most running conditions. The feedback impedance Z is adjusted to give a 6 dB/octave rolloff from 32 Hz to 3.2 kHz. The frequency response is flat elsewhere in the band of interest unless the adjustable high pass filter is in use. The expression

$$H_o(s) = \left[1 + 100 \frac{s T_4}{1 + s T_4} \right]^{-1} \qquad (II.2.2)$$

with $T_4 = 50\,\mu$sec accurately models the diode driver unity gain transfer function. The terminal amplifier load

Figure II.4 Schematic representation of the voltage to current converter.

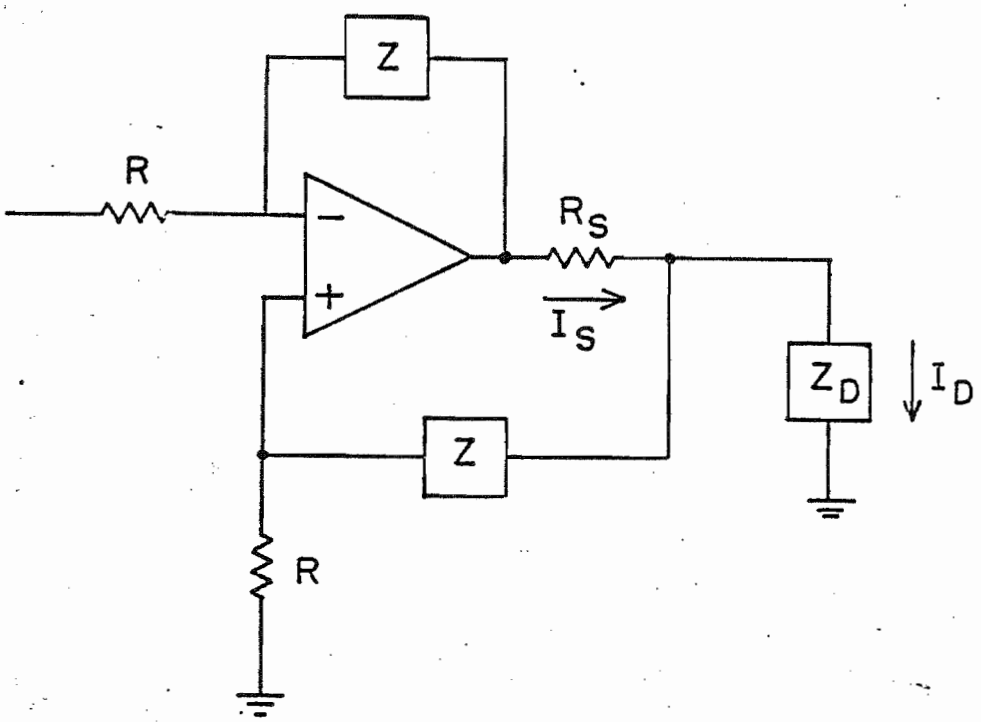
Z
R
−
+
R_S
I_S
Z_D
I_D
Z
R

Figure II.5 The LED driver circuit diagram.

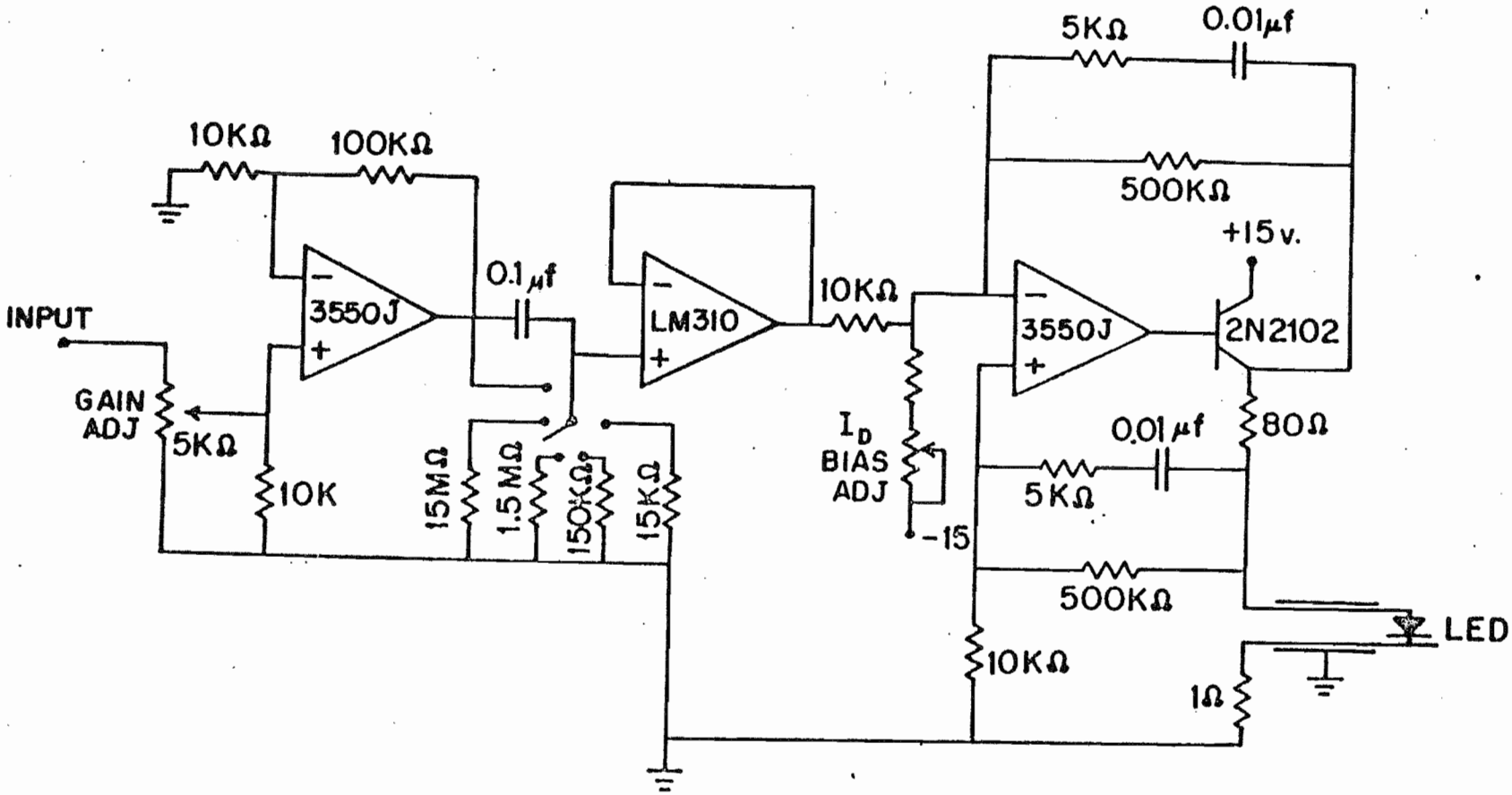
10KΩ
100KΩ
INPUT
GAIN ADJ
5KΩ
10K
3550J
0.1 μf
15MΩ
1.5MΩ
150KΩ
15KΩ
LM310
10KΩ
I_D BIAS ADJ
-15
5KΩ
0.01μf
500KΩ
+15v.
3550J
2N2102
0.01 μf
80Ω
5KΩ
500KΩ
LED
10KΩ
1Ω

capacitance forces a 6 dB/octave rolloff at 2.9 kHz. The fast channel response H_c is the product of H_T and H_D. The breakpoints have been chosen to peak the response at 5 Hz with a smooth rolloff to 10 kHz or more. The measured response is shown in figure II.6.

II.3 The Slit Current Preamplifiers

The slit current preamplifier circuit is shown in figure II.7. The first stage is a low noise current to voltage transducer. The second stage provides the logarithmic gain characteristic. A pair of amplifiers is matched by obtaining the non-linear feedback from the gate-drain junctions of a pair of matched field effect transistors. The third stage drives the long cable to the control room. The dc gain is illustrated in figure II.8 and the measured unity gain frequency response H_P is shown in figure II.9. The bandwidth of the preamplifiers is almost 30 kHz.

A pair of preamplifiers is housed in a single aluminum chassis. The components are arranged on three circuit boards by parallel stages. The boards are shielded from each other within the aluminum cabinet. A twinaxial cable routes the output signals to the difference amplifier in the control room. Very short coaxial cables connect the slits to the amplifier inputs.

The difference amplifier and the other components in the

Figure II.6 The measured frequency response of the stripper modulation channel.

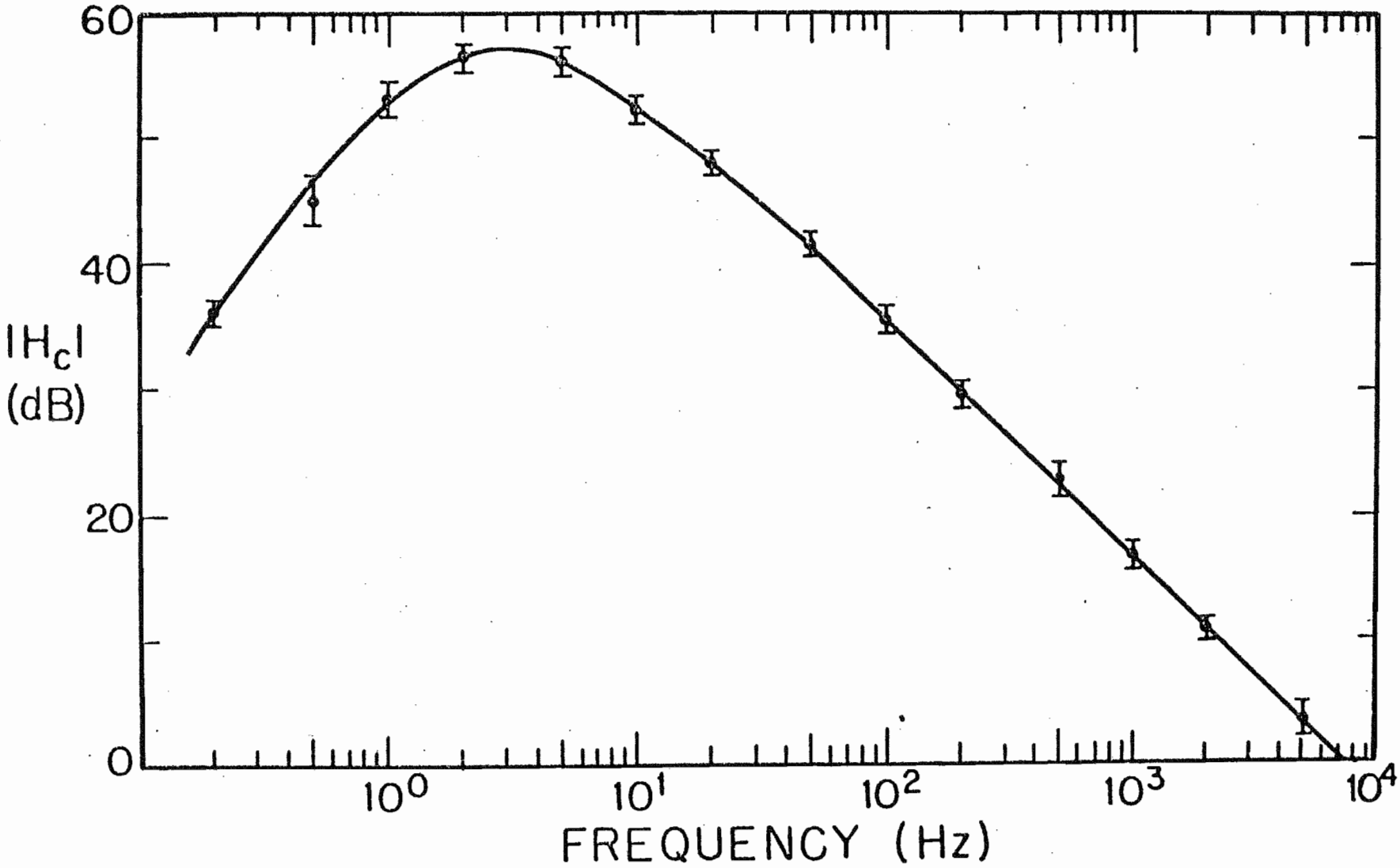
60
40
20
0
$|H_c|$
(dB)
10^0
10^1
10^2
10^3
10^4
FREQUENCY (Hz)

Figure II.7 The slit current preamplifier circuit diagram.

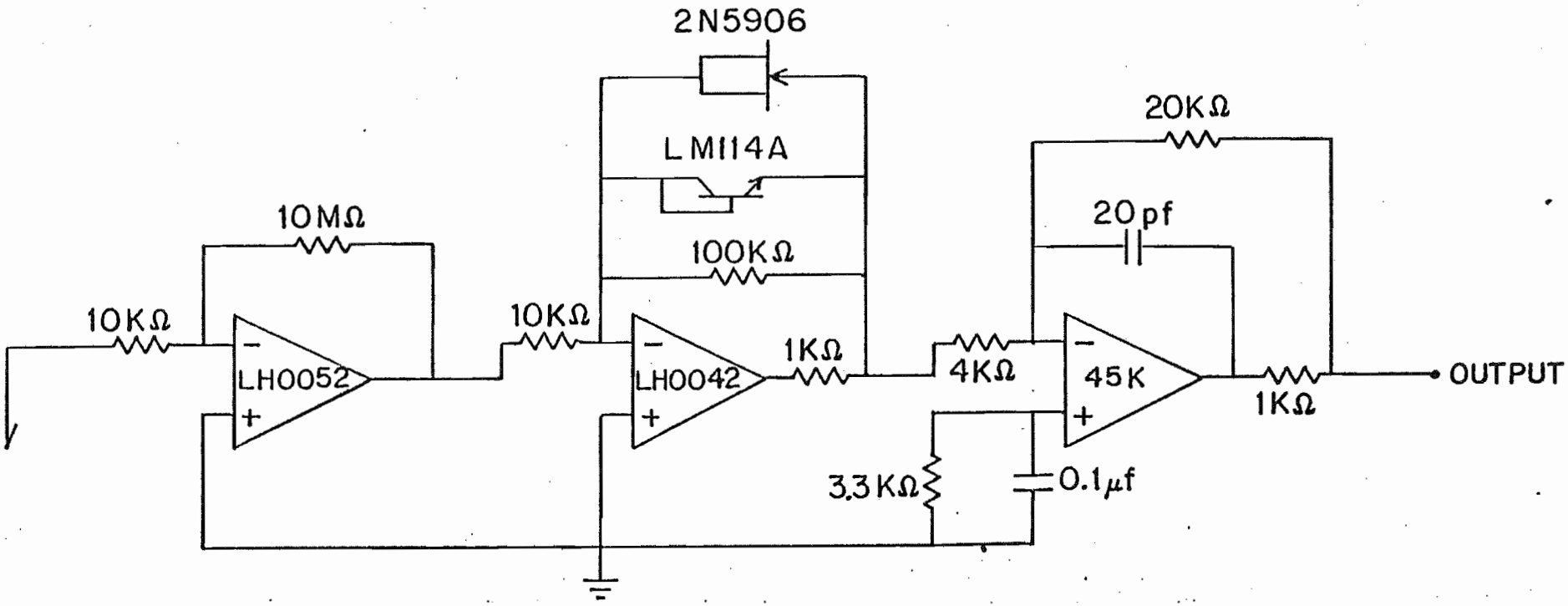
2N5906
LM114A
20KΩ
20pf
10MΩ
100KΩ
10KΩ
10KΩ
1KΩ
4KΩ
LH0052
LH0042
45K
1KΩ
OUTPUT
3.3KΩ
0.1μf

Figure II.8 The measured dc gain characteristic of the slit current preamplifier.

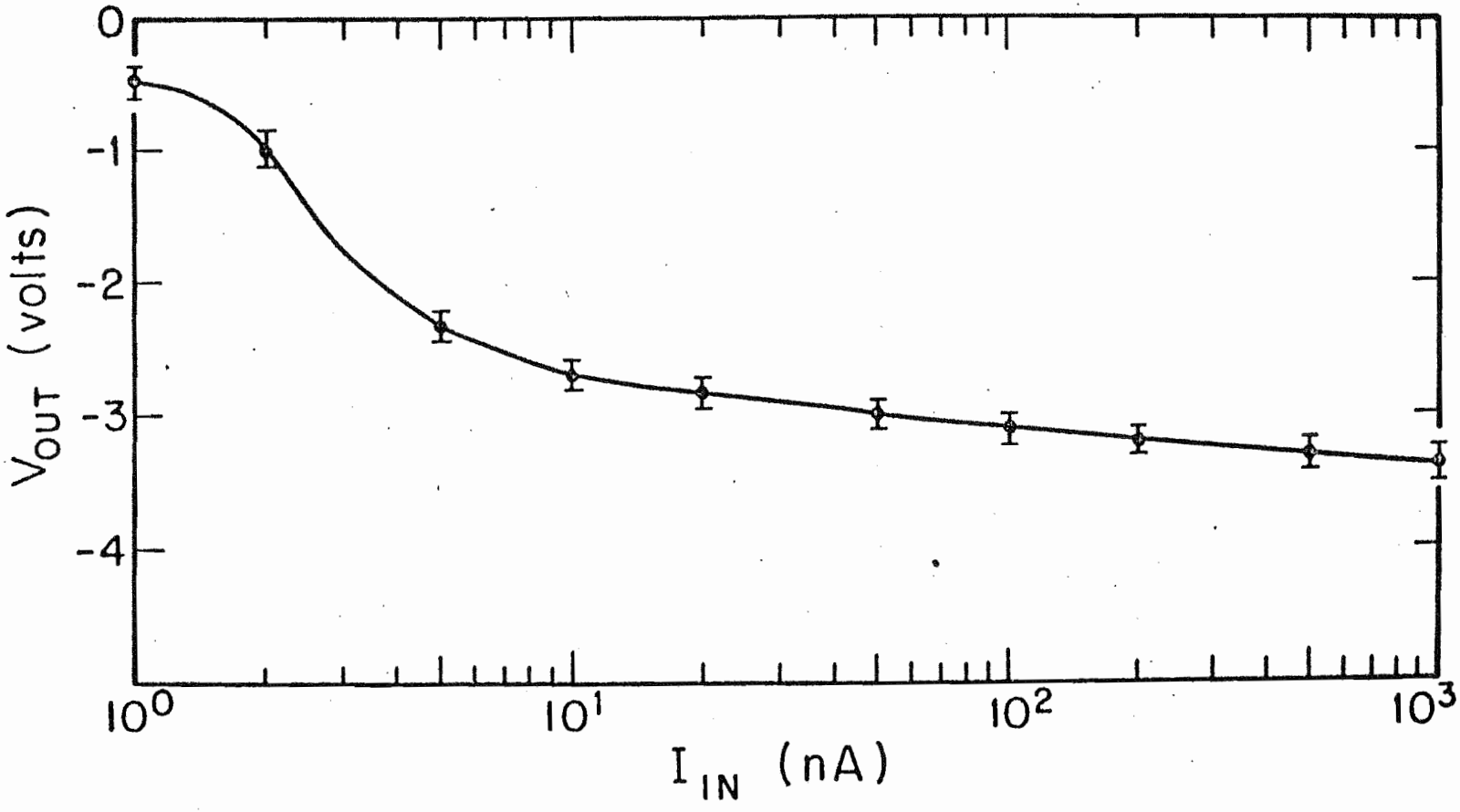
0
-1
-2
-3
-4
V_{OUT} (volts)
10^0
10^1
10^2
10^3
I_{IN} (nA)

Figure II.9 The measured frequency response of the slit current preamplifier.

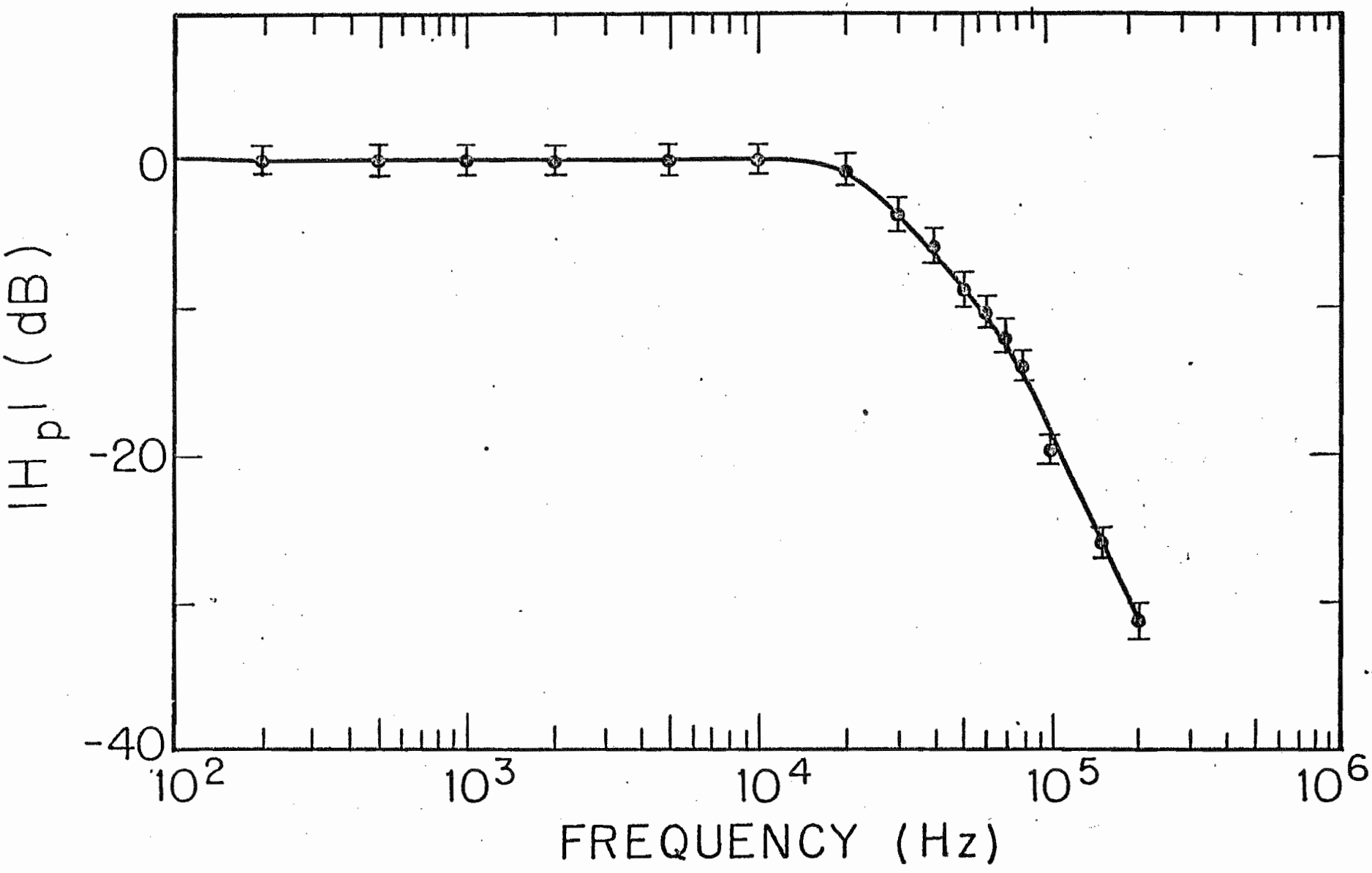
0
-20
-40
$|H_p|$ (dB)
10^2
10^3
10^4
10^5
10^6
FREQUENCY (Hz)

corona control locp comprise a slightly modified Gere type control system manufactured by High Voltage Engineering Corporation.

BIBLIOGRAPHY

M. Abramowitz and I. A. Stegun eds., Handbook of Mathematical Functions, U. S. Govt., Washington, D. C. (1970).

J. D. Anderson and C. Wong, Phys. Rev. Lett. 7 (1961) 250.

H. A. Bethe, Phys. Rev. 47 (1935) 747.

H. A. Bethe and G. Placzek, Phys. Rev. 51 (1937) 450.

E. G. Bilpuch, A. M. Lane, G. E. Mitchell and J. D. Moses, Phys. Lett. 28C (1976) 147.

C. R. Bingham and M. L. Halbert, Phys. Rev. C2 (1970) 2297.

R. Bloch, R. E. Pixley, W. Reichart and F. Zamboni, Nucl. Instr. and Meth. 59 (1968) 325.

N. Bohr, Nature 137 (1936) 344.

J. C. Browne, unpublished Ph.D. thesis, Duke University (1969).

J. E. Cairns, unpublished M.S. thesis, McMaster University (1973).

J. E. Cairns, M. W. Green and J. A. Kuehner, Nucl. Instr. and Meth. 114 (1974) 489.

B. L. Cohen and O. V. Chubinsky, Phys. Rev. 131 (1963) 2184.

T. G. Dzubay, E. G. Bilpuch, F. O. Purser, J. D. Moses, H. W. Newson and G. E. Mitchell, Nucl. Instr. and Meth. 101 (1972) 407.

D. S. Flynn, unpublished Ph.D. thesis, Duke University (1976).

J. D. Fox, C. F. Moore and D. Robson, Phys. Rev. Lett. 12 (1964) 198.

E. A. Gere, H. P. Lie and G. L. Miller, IEEE Trans. on Nucl. Sci. NS-14, no. 3 (1967) 161.

A. Gilbert and A. G. W. Cameron, Can. J. Phys. 43 (1965) 1446.

A. Graue, L. H. Herland, K. J. Lervik, J. T. Nesse and E. R. Cosman, Nucl. Phys. A187 (1972) 141.

H. L. Harney and H. A. Weidenmuller, Nucl. Phys. A139 (1969) 241.

H. L. Harney, unpublished computer code, (1969).

E. M. Henley, Isospin in Nuclear Physics, ed. D. H. Wilkinson (North Holland, Amsterdam, 1969) 15.

P. L. Kapur and R. E. Peierls, Proc. Roy. Soc. A166 (1938) 277.

G. A. Keyworth, G. C. Kyker, Jr., E. G. Bilpuch and H. W. Newson, Phys. Lett. 20 (1966) 281.

G. A. Keyworth, G. C. Kyker, Jr., E. G. Bilpuch and H. W. Newson, Nucl. Phys. 89 (1966) 590.

A. M. Lane and R. G. Thomas, Rev. Mod. Phys. 30 (1958) 257.

A. M. Lane, Nucl. Phys. 35 (1962) 676.

A. M. Lane, Isospin in Nuclear Physics, ed. D. H. Wilkinson (North Holland, Amsterdam, 1969) 509.

A. M. Lane, J. E. Lynn and J. D. Moses, Nucl. Phys. A232 (1974) 189.

A. Mekjian and W. M. MacDonald, Nucl. Phys. A121 (1968) 385.

P. A. Mello, Ann. Phys. 45 (1967) 240.

P. B. Moon and R. Tillman, Proc. Roy. Soc. 153 (1936) 421.

D. A. Outlaw, unpublished Ph.D. thesis, North Carolina State University (1974).

P. B. Parks, H. W. Newson and R. M. Williamson, Rev. Sci. Instr. 29 (1958) 834.

C. E. Porter and R. G. Thomas, Phys. Rev. 104 (1956) 384.

M. A. Preston, Physics of the Nucleus, (Addison-Wesley, 1962).

D. Robson, Phys. Rev. 137 (1965) B535.

G. W. Roth and W. G. Weitkamp, Nucl. Instr. and Meth. 101 (1972) 407.

P. Richard, C. F. Moore, D. Robson and J. D. Fox, Phys. Rev. Lett. 13 (1964) 343.

P. Richard, C. F. Moore and J. D. Fox, Nucl. Phys. A174 (1971) 273.

D. L. Sellin, unpublished Ph.D. thesis, Duke University (1968).

W. J. Thompson, J. L. Adams and D. Robson, Phys. Rev. 173 (1968) 975.

G. Vourvopolis, R. Shoup, J. D. Fox and J. P. Ball, Proc. Conf. Nucl. Isospin, 2nd, Asilomar, Pacific Grove, CA, J. D. Anderson, S. D. Bloom, J. Cerney and W. W. True eds. (Academic Press, New York, 1969) 205.

E. P. Wigner, Phys. Rev. 70 (1946) 15.

E. P. Wigner, Phys. Rev. 70 (1946) 606.

E. P. Wigner and L. Eisenbud, Phys. Rev. 72 (1947) 29.

E. P. Wigner, Ann. Math. 62 (1955) 548.

W. M. Wilson, unpublished Ph.D. thesis, Duke University (1973).

S. A. Zaidi and S. Darmodjo, Phys. Rev. Lett. 19 (1967) 1446.

BIOGRAPHY

Mark Eric Bleck

Personal: Born 9 May, 1951, Buffalo, New York
Married 21 August 1976, to the former Donna R. Denny

Education: B.S. in Physics, California Institute of Technology, 1973

Positions: Teaching Assistant, Duke University, 1973-1974
Research Assistant, Duke University, 1974-present

Membership: American Physical Society
Sigma Xi

Abstracts: 'Channel Spin Mixing Ratios in High Resolution Proton Inelastic Scattering on ^{44}Ca,' T. R. Dittrich, C. R. Gould, G. E. Mitchell, E. G. Bilpuch, M. E. Bleck and K. Stelzer, B. A. P. S. 21 (1976) 662.

'A Three Loop Regulator for the TUNL Tandem Van de Graaff Accelerator,' M. E. Bleck, W. K. Wells, D. A. Outlaw, F. O. Purser and E. G. Bilpuch, B. A. P. S. 22 (1977) 578.

'A High Resolution Study of the Lowest 1/2$^+$ Analogue State in ^{91}Nb,' M. E. Bleck, W. K. Wells, D. A. Outlaw, C. R. Westerfeldt, E. G. Bilpuch and G. E. Mitchell, B. A. P. S. 23 (1978) 554.